THE DEVELOPMENT OF NOVEL, HIGH-FIDELITY MODELING TOOLS FOR THERMAL MANAGEMENT OF PLANAR AND TUBULAR SOLID OXIDE FUEL CELL SYSTEMS

by

Kyle J. Kattke

A thesis submitted to the Faculty and the Board of Trustees of the Colorado School of Mines in partial fulfillment of the requirements for the Masters of Science (Engineering).

Golden, Colorado

Date _____

Signed:_____
Kyle J. Kattke

Signed:_____
Dr. Robert Braun
Thesis Advisor

Golden, Colorado

Date _____

Signed:_____
Dr. Terry Parker
Professor and Head
Department of Engineering

ABSTRACT

Solid oxide fuel cells (SOFCs) are emerging as a promising energy conversion technology alternative for small-scale power generation applications. High efficiency and reasonable power density give SOFCs an advantage over conventional battery and engine generator technologies. As with any technology, the full benefits of SOFCs are only realized with effective system designs. In mobile applications, system design includes tightly packaging balance of plant (BoP) hardware along with the SOFC in order to achieve high volumetric power densities. As system components are placed in close proximity to one another, thermal integration arises as a second design consideration. Not only are components connected through process gas streams and the associated conduits, thermofluidic coupling occurs between components via both fluid dynamic and convection and radiation heat transfer mechanisms. The goal of this thesis is to create system-simulation tools that capture these component interactions. Thermal interactions between components play a particularly significant role in high-temperature SOFC systems, and by adequately representing these physics, the coupling between stack performance and process gas temperatures throughout the system can be extracted and used to evaluate system architectures and operating parameters.

Two distinct thermally coupled system models are presented where each model represents small-scale SOFC systems of varying system architecture and geometric configuration. The first system model is applicable for planar, anode-supported SOFCs in which each system component is distinct and physically separated from one another. The second system modeling approach is applicable for novel, highly-integrated tubular SOFC systems in which system components share common boundaries. In the planar geometric configuration, a reduced-order thermal resistance network model is developed and couples component processes in the system primarily through heat transfer mechanisms. In the tubular configuration, a high-fidelity model incorporating computation fluid dynamics (CFD) is developed for a 66-tube mobile power system and

is employed to capture the thermofluidic interactions throughout the entire highly-integrated system.

Simulation results from both models reveal the significant effect heat transfer from the stack to its surroundings has on stack performance and process gas flows throughout the system. In the planar system, convection and radiation transport in the stack gas manifolds and at the stack insulation surface provides additional heat transfer pathways from the stack. A 65% reduction in oxidant delivered to the stack is predicted in the planar stack compared to models which represent the SOFC stack as adiabatic. When gas manifold heat transfer is considered in a counter-flow, planar SOFC stack, the location of the maximum temperature gradient within the cell is observed to shift towards the oxidant inlet. Furthermore, the magnitude of the maximum temperature gradient is predicted to be 24% higher than that found in adiabatic stack model representations. The gas manifold heat transfer is also found to represent a significant fraction (often greater than 30%) of the total cathode gas temperature rise. Simulation results of planar SOFC systems point to circulating recuperator exhaust within the system enclosure as an effective means for providing a cooling medium or thermal sink that is in addition to the cathode gas flow and thereby reduces excess air requirements and the associated parasitic power.

In contrast to the planar SOFC system, radiation is found to be the dominate heat transfer mechanism accounting for 66-92% of total heat rejection from the external surface of tubular cells. The dominance of radiation heat transfer in highly-integrated tubular SOFC systems stems largely from the variation in radiation view factor from the tube surface to the wall enclosing the tube bundle. It is found that the variation of radiation view factor produces nominal tube temperature variations within the SOFC tube bundle that result in a cell-power variation ranging from 7.6-10.8 W per tube. Additionally, simulation results show a strong relationship between stack performance and the temperature field within the recuperator which suggests utilizing a counter-flow recuperator. Finally, effective control variables are revealed with insight from the thermally coupled models. Interestingly, it is observed that lowering the fuel flowrate is

not an effective means to increase fuel utilization in highly-integrated tubular systems because of the resulting lower cathode air preheat temperature in the recuperator causing stack power and system efficiency to decrease. Analysis of simulation results points to increasing current as the preferred control parameter to increase fuel utilization and system efficiency.

TABLE OF CONTENTS

LIST OF FIGURES

LIST OF TABLES

ACKNOWLEDGMENTS

I am very thankful for my parents who have always taught the value of hard work and taking pride in my work. I am also grateful to my advisor Dr. Rob Braun with whom I had countless discussions that provided the guidance for my research. I also would like to thank fellow graduate student Andrew Colclasure for implementing several changes to his existing fuel cell model that allowed me to use his model in my research. I would also like to express my gratitude to Dr. Graham Goldin who provided the initial UDF foundation and was very helpful with any FLUENT issues. Additionally, thanks is due to Dr. Braun, Dr. Bob Kee, Dr. Neal Sullivan, and Dr. Jason Porter for serving on my thesis committee. Finally, I would like to express my appreciation to the U.S. Office of Naval Research and the U.S. Department of Energy, Office of Energy Efficiency and Renewable Energy for their financial support of my work.

CHAPTER 1

INTRODUCTION

As the world's demand for energy rapidly increases, fuel cells are emerging as a viable alternative source of efficient and clean energy. High efficiency is possible because fuel cells are able to directly convert the chemical energy of a fuel into electrical energy. This is in contrast to combustion where chemical energy is first converted to thermal energy that can be used to drive a power cycle. Potential useful work of the fuel is destroyed due to irreversibilities in the combustion process. In the case of Rankine power cycles, the Carnot efficiency limits the magnitude of useful work extracted from thermal energy supplied in the form of a hydrocarbon fuel. Fuel cells can also have fewer greenhouse gas emissions than traditional combustion power sources. In fact, fuel cells only produce water as a byproduct when utilizing pure hydrogen as a fuel source. Fuel cells are easily scaled leading to power applications ranging from single watt portable power to mega-watt grid electrical power generation.

1.1 Solid Oxide Fuel Cells

There are several types of fuel cells, but this thesis is focused on solid oxide fuel cells (SOFCs). SOFCs are made up of ceramic based materials which distinguishes SOFCs from other fuel cell types. Another unique characteristic to SOFCs is their high operating temperatures, 700-1000°C. Figure 1.1 illustrates how an SOFC is able to directly convert the chemical energy of a fuel into electrical energy. A fuel, in this case hydrogen, enters the anode side and air enters the cathode side of the cell. Oxygen diffuses through the porous cathode electrode and is electrochemically reduced at the cathode-electrolyte interface known as the cathode triple phase boundary (TPB). Following reaction

Eq. (1.1), oxygen is reduced creating oxygen ions which are transported across the dense electrolyte to the anode-electrolyte surface known as the anode TPB. Hydrogen diffuses through the porous anode electrode to the anode TPB, is oxidized by the oxygen ion producing water and two free electrons. Hydrogen oxidation occurs via the reaction given in Eq. (1.2). Free electrons liberated at the anode are at a higher electrical potential than at the cathode; thus, a driving potential exists to drive a current. Free electrons are collected at the surface of the anode, sent through an external load, and finally collected back on the cathode surface. Unlike batteries, SOFCs will continue to create electrical power as fuel and oxidant are continuously supplied.

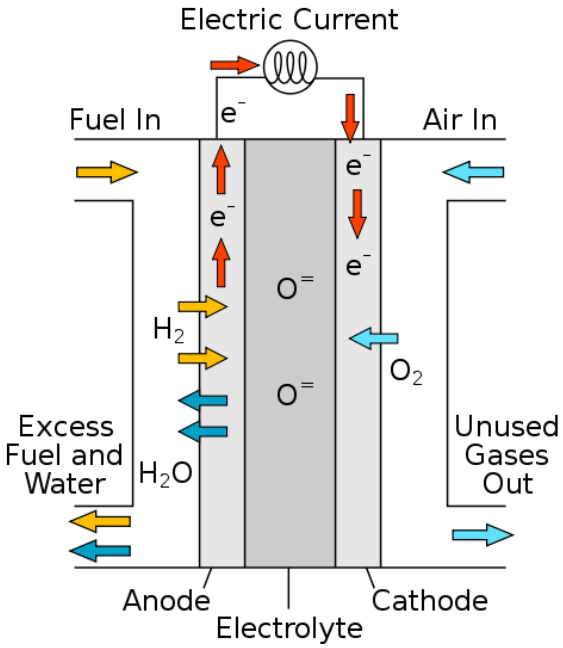

Figure 1.1 Diagram illustrating how an SOFC operates

$$\frac{1}{2}O_2 + 2e^- \leftrightarrow O^{-2} \tag{1.1}$$

$$H_2 + O^{-2} \leftrightarrow H_2O + 2e^- \tag{1.2}$$

The overall fuel cell reaction is the combination of both electrochemical half reactions resulting in the overall reaction in Eq. (1.3). The overall reaction in Eq. (1.3) also represents the reaction for conventional combustion of H_2. The advantage of a fuel cell is that by physically separating the combustion reaction with the membrane electrode

assembly (MEA), the energy released by rearranging electrons from reactants to products can be directly harnessed to produce electrical work. In a combustion reaction, the energy released with electron rearrangement is converted to thermal energy.

$$H_2 + \frac{1}{2}O_2 \leftrightarrow H_2O \tag{1.3}$$

While Figure 1.1 illustrates an SOFC of planar geometry, SOFCs can also be of tubular geometry as shown in Figure 1.2. Other geometries are possible, but planar and tubular cells dominate the SOFC field. The advantages/disadvantages to both designs will be discussed in Section 1.1.4 on fuel cell stacks.

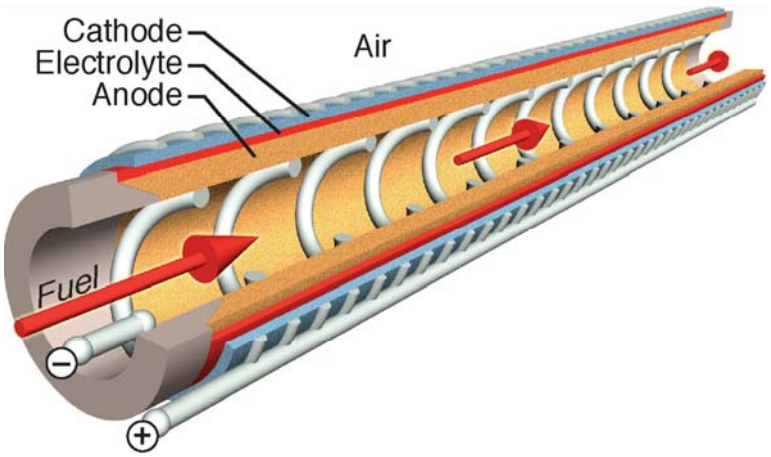

Figure 1.2 Schematic of a tubular SOFC. Current collectors shown as white metallic coils at surface of anode and cathode electrodes [1].

1.1.1 Cell Performance

While fuel cells are able to convert the chemical energy of a fuel directly into electrical energy, thermodynamics places a limit on the maximum electrical work extracted from any chemical reaction. Specifically, the maximum work potential of any chemical reaction is given by the change in Gibbs free energy of the reaction. The Gibbs free energy is a combination of other thermodynamic properties as shown in Eq (1.4). The change in Gibbs free energy of a reaction can be converted into an electrical potential with Eq. (1.5) where F is Faraday's constant, n is the number of electrons liberated, and $\Delta\bar{g}_{rxn}$ is on a molar basis. Equation (1.5) represents the maximum

theoretical voltage a fuel cell can produce. The maximum efficiency of a fuel cell is then given by the ratio of Gibbs free energy to the thermal energy of a reaction, Eq. (1.6). The maximum efficiency decreases with increasing fuel cell temperature. In the operating range of SOFCs, 700-1000°C, the maximum theoretical efficiency is 0.67 and 0.60, respectively. The operating range of 700-1000°C also places limits on the maximum theoretical voltage at 1.0 and 0.92V, respectively. The above values assume a H_2 fuel source, but high theoretical efficiencies and similar voltages are achieved with other hydrocarbon fuel sources such as CH_4.

$$G = H - TS \tag{1.4}$$

$$V = -\frac{\Delta \bar{g}_{rxn}}{nF} \tag{1.5}$$

$$\eta_{\max} = \frac{\Delta g_{rxn}}{\Delta h_{rxn,HHV}} \tag{1.6}$$

Equations (1.5) and (1.6) both represent the theoretical maximums with pure fuel and oxidant entering the fuel cell. The dilution of fuel with water vapor being produced at the anode along with utilizing standard air in the cathode will both reduce the maximum operating voltage of a fuel cell. The maximum voltage a fuel cell can produce at a given temperature, pressure, and gas compositions is given by the Nernst voltage, Eq. (1.7).

$$E_N = -\frac{\Delta \bar{g}_{rxn}}{nF} - \frac{RT}{nF} \ln \frac{\Pi a_{products}^{v_i}}{\Pi a_{reac\tan ts}^{v_i}} \tag{1.7}$$

where a is the activity of the species and v is the corresponding stoichiometric coefficient. The activity of a species can be approximated by its partial pressure. The Nernst voltage represents the theoretical maximum voltage at the operating conditions of the fuel cell.

The Nernst voltage is only realized with zero net current flowing through the cell. As current is drawn from the cell to power the external load, irreversible losses occur within the cell and the operating voltage drops below the Nernst voltage. Three mechanisms

cause voltage losses (also referred to as overpotentials and polarizations) within the cell. The first irreversibility stems from sluggish reaction kinetics at the electrode TPBs. Activation overpotentials are required to promote the electrochemical half-reactions at the TPBs. Secondly, ohmic losses occur due to resistance to charge transfer within the electrolyte and electrodes. Lastly, concentration losses occur if the half-reactions begin to be limited not by kinetics but by diffusion limitations through the porous electrodes. The total voltage loss in the cell is the summation of the three irreversibilities, see Figure 1.3. The amount of current produced in a cell is directly proportional to the surface areas of the electrodes; therefore, current output is normalized by area resulting in current density, j.

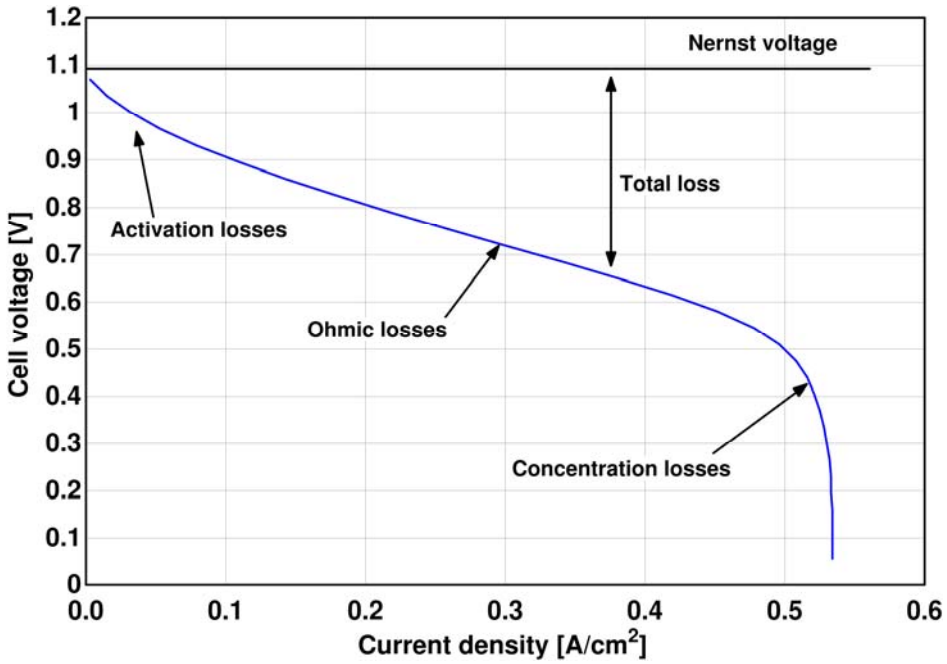

Figure 1.3 Typical fuel cell voltage current relationship for a tubular cell

A fuel cell is most efficient at low current densities where overpotentials are minimized; however, fuel cells are typically operated at moderate current densities to generate appreciable power without excessive cell area. Figure 1.4 shows a plot of power density overlaid onto a V-j curve. In fuel cells, there is always a trade-off between the physical size of the cell and its efficiency. To produce the same power, a smaller cell operates at higher current densities and lower efficiency than a larger cell operating at lower current densities and higher cell efficiency. Fuel cells typically operate at mid-

level current densities in the linear region of the V-j curve. Depending on the target application, the operating point may shift towards higher efficiency or higher power density.

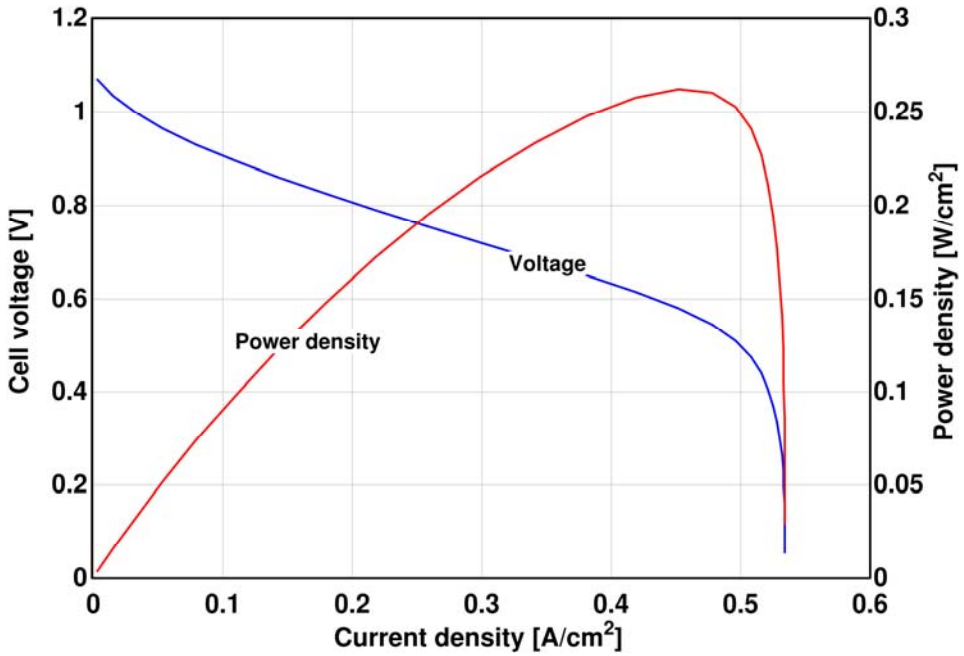

Figure 1.4 Typical cell power density relation to current density for a tubular cell

In order to drive a load, some magnitude of overpotential must be overcome. The chemical energy required to overcome the total overpotential is irreversible converted to heat within the cell. Even operating at the Nernst voltage, some irreversible heat generation occurs as the maximum efficiency, Eq. (1.6), is less than 100%. This being said, an SOFC is an exothermic device. Thermal energy created within the cell must be transported from the cell in order to maintain a constant cell temperature. The methods in which thermal energy is transported out of the cell are discussed in Section 1.1.4 which describes how fuel cell stacks are created.

1.1.2 Materials

One of the distinguishing characteristic of SOFCs is the MEA is constructed from ceramic materials. SOFC electrolytes are typically composed of pure yttria stabilized zirconia (YSZ). YSZ is a good ion conductor and a poor electron conductor which is

essential for any electrolyte. The electrolyte is dense to prevent gas leakage between the fuel and oxidant. SOFC anodes are typically made of a cermet comprised of YSZ and nickel. Nickel acts as a catalyst along with providing good electron conductance pathways The YSZ provides structural support and helps to match thermal expansion between the anode and electrolyte. Lastly, cathode electrodes are typically constructed from a cermet combining YSZ and lanthanum strontium magnetite (LSM). Both the anode and cathode are porous to allow transport of fuel and oxidant, respectively, to the TPB.

1.1.3 Advantage over Competing Fuel Cell Types

The majority of advantages SOFCs possess over competing fuel cell types originates from their high operating temperatures. In low temperature fuel cells, expensive catalysts such as platinum are dispersed at the TPBs in order to decrease activation losses caused by slow reaction kinetics. The high operating temperatures of SOFCs provides for sufficiently fast reaction rates without the need for a platinum catalyst coating; thus, activation losses are lower in SOFCs than low temperature fuel cells. The second main advantage is the ability to internally reform hydrocarbons within the SOFC. At the SOFC operating temperatures, nickel in the anode acts as a catalyst to reform fuels such as methane and carbon monoxide. Lastly, the high quality waste heat allows SOFC integration into combined heating and power (CHP) applications. CHP systems can achieve thermal efficiencies of 60-80% [2] based on the higher heating value (HHV).

1.1.4 Stacks

The voltage of a single cell is not enough to drive any significant load; therefore, fuel cells are connected in electrical series to build up the output voltage. Combining cells in electrical series results in a fuel cell stack also called a bundle with tubular cells. Since there is always irreversible heat generation within a cell, the stack must be able to transport internally generated thermal energy in order to maintain a constant stack temperature. The differences between planar and tubular cell geometries become

apparent when considering their respective stack architectures. The construction of planar and tubular stacks along with their thermal management strategies are described in the following.

1.1.4.1 Planar

A representative schematic of a planar stack is shown in Figure 1.5. A defining component in planar SOFC stacks is the interconnect. The interconnect has dual purposes. First it provides gas channels above the anode and the cathode where fuel and oxidant flows, respectively. Secondly, the interconnect ribs contact the electrode surfaces collecting electrons from the anode surface and distributing electrons on the cathode surface. Repeating units of MEAs and interconnects creates a planar stack. A challenge in planar stacks is sealing. To avoid anode and cathode gas mixing, the entire stack must be held together under pressure with compression plates. Without the freedom to expand, high thermal stresses can develop in planar stacks. The benefit of planar stacks is their high power densities.

The dominate heat transfer mechanism internal to planar SOFC stacks is convection. Thus, the ability to control stack temperature is tied to controlling either the fuel or oxidant flow through the stack. Varying fuel flow is not desirable for temperature control because flowing excess fuel substantially lowers system efficiency. Oxidant flow is what is typically varied in planar stacks to control stack temperature. The majority of irreversible heat generated in the stack is convectively transported out of the stack via excess oxidant flow. A drawback to convective stack cooling with excess oxidant flow is the increased blower power requirement. Internal steam reforming of hydrocarbon fuels on the Ni anode can also adsorb thermal energy to reduce convective cooling requirements.

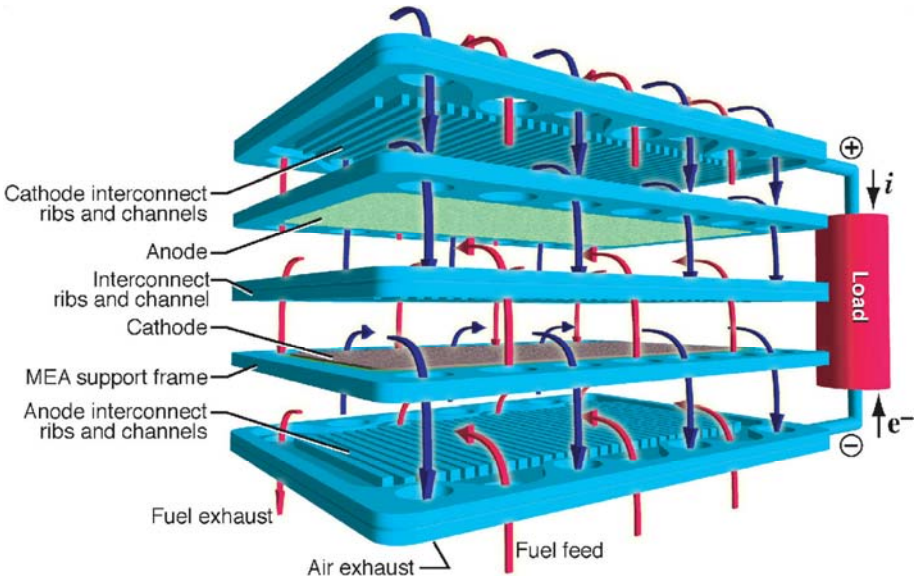

Figure 1.5 Representation of a planar SOFC stack [1]

1.1.4.2 Tubular

A representative schematic of a tubular stack is shown in Figure 1.7. Unlike the planar stack, all cells in a tubular stack share a common gas volume external to the tubular cells (cathode gases in this figure). In this tubular stack, cells are supported at the inlet tube-sheet located at the fuel entrance. Air leaves the cathode region through cutouts surrounding each tube in the outlet tube-sheet. Tubular cells are only physically constrained at the inlet tube-sheet. Because of their free end, tubes are allowed to thermally expand with lower levels of thermally induced stresses than compared to planar stacks. Gas sealing in tubular stacks is accomplished with a single seal between the tube and the inlet tube-sheet; therefore, gas sealing is easier to accomplish in tubular stacks. A downside side tubular stacks is their long conduction paths. Electrons are collected with a current collector lying on the anode surface (see Figure 1.2), travel up the length of the cell, travel down the length of the next cell, and distribute along the cathode surface via the cathode current collector. These long electron pathways lead to larger ohmic losses than in planar stacks. Ensuring good contact between the current collectors and the anodes is also a manufacturing challenge.

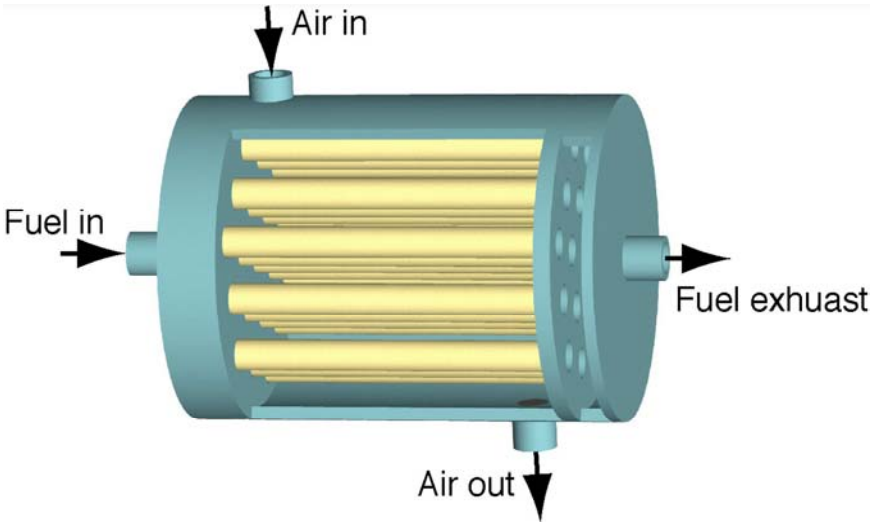

Figure 1.6 Representation of a tubular SOFC stack [1]

There has been little research on small-scale tubular stacks (<100 cells) as shown in Figure 1.7; therefore, current temperature control schemes are relatively unknown. The majority of tubular stack research has focused on large arrays of tubular cells where convective cooling via excess oxidant flow is employed to control stack temperatures. It will be shown in this thesis that radiation plays a large role in transporting thermal energy out of smaller-scale tubular stacks. Unlike planar stacks where the stack edge areas are small in comparison to the overall stack area, tubular stacks can have a large cell area near the stack periphery. Large temperature differences can develop between bundle periphery cells and the stack enclosure wall which promotes increased radiation heat transfer at the elevated SOFC operating temperature. Convectively cooling small-scale tubular stacks may not be necessary if radiation heat loss can be strategically exploited thus eliminating the need for increased blower power.

1.1.5 Challenges

With the many benefits to SOFCs due to their high operating temperature comes several challenges in their operation. Every component within the SOFC will expand as it is brought up to the operating temperature. Thermally induced stresses will develop if the cells are not free to expand. As some level of sealing is required, the cell will never be completely free to expand; thus, thermally induced stresses need to be maintained

below the mechanical limits of the material. Thermal stresses also develop within the cell as the MEA is composed of different materials. Careful matching of thermal expansion coefficients between the three layers in the MEA is necessary to avoid delaminating and cracking of the MEA. As mentioned in the materials section, the electrolyte material, YSZ, is dispersed within both the anode and cathode electrodes in an attempt to match thermal expansion coefficients within the MEA. Mechanical stability is also a problem over time as the SOFC must go through numerous thermal cycles. Start-up and shut-down procedures must be such that temperature gradients within the cell are minimized. While there are challenges to SOFCs, their numerous benefits including high efficiency, relatively low cost materials, and high quality waste heat continue to attract research.

1.2 SOFC Systems

An SOFC stack does not operate alone; it requires the integration of several components to create a functional SOFC system. Components that accompany the SOFC stack are called the balance-of-plant (BoP). The BoP is designed to deliver a supply of fuel and oxidant to the stack, reformer complex hydrocarbon fuels, preheat fuel and oxidant streams prior to entering the stack, and condition the DC stack power to suit the desired application. A schematic of an SOFC system is shown in Figure 1.7. In this system, liquid fuel is first pumped through a vaporizer prior to entering a fuel reformer. Reformate then enters the anode gas channels of the stack. Oxidant, in this case air, is brought into the system through two blowers. One stream is used in the fuel reformer while the other stream preheats within a recuperative heat exchanger prior to entering the cathode gas channels of the stack. Fuel that is not electrochemically consumed within the stack is oxidized within a tailgas burner or tailgas combuster (TGC). The fraction of fuel electrochemically consumed within the stack is defined by the fuel utilization, U_F [2].

$$U_F = \frac{\left(\dot{n}_{H_2}\right)_{stack\ consumed}}{\left(4\dot{n}_{CH_4} + \dot{n}_{H_2} + \dot{n}_{CO}\right)_{anode\ inlet}} \tag{1.8}$$

where $\dot{n}$ is the molar flow rate of the gas species.

The thermal energy produced within the TGC is used to preheat the air stream in the recuperative heat exchanger prior to leaving the system. Electrical power produced is used to power ancillary loads such as the blowers and pump with remaining power going to the desired application. To mitigate heat loss, the majority of system components are located within an insulated enclosure referred to as the hotbox or hot enclosure.

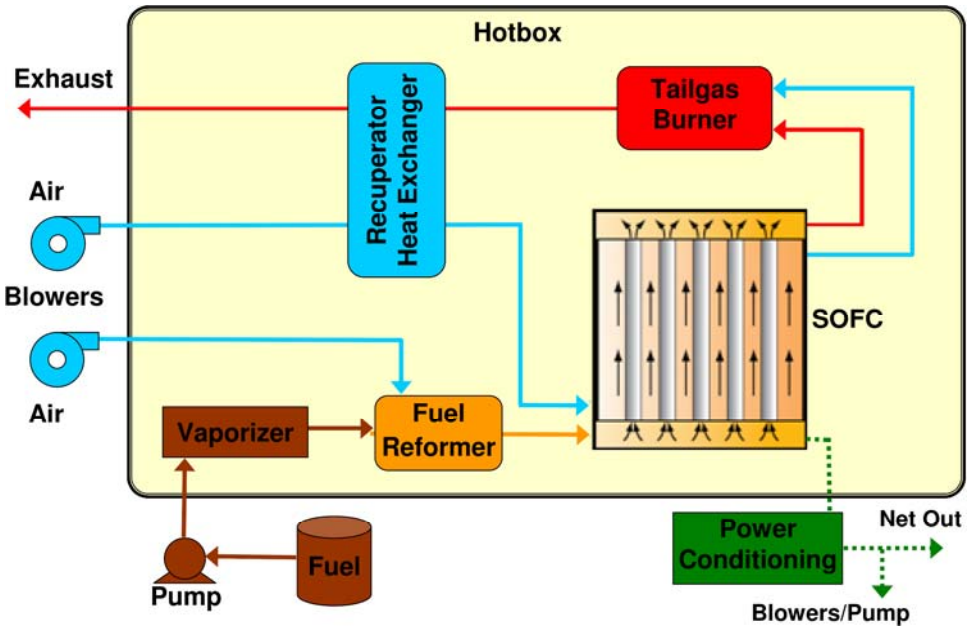

Figure 1.7 Process schematic representing a SOFC system

Effective thermal integration of system components is critical in SOFC systems in order to achieve high system efficiencies, 40-45% HHV. Each system component can be classified as a sink, a source, or as thermally neutral in terms of thermal management. An efficient SOFC system requires an effective coupling between system-level sink and sources. As an example, the TGC exhaust gas is used to preheat oxidant to the desired cathode inlet temperature. By effectively integrating the TGC with the recuperative heat exchanger, less excess fuel needs to be oxidized in the TGC thereby lowering the fuel input to the system, i.e. increasing system efficiency. The thermal characteristics of each system component will be described in the following sections.

1.2.1 Fuel Reforming

In order to operate an SOFC on readily available fuels such as logistic and diesel fuels, a fuel reformer is required upstream of the stack anode. While current SOFC anodes can reform simple hydrocarbons such as methane, current SOFCs are unable to reform complex hydrocarbons because of degradation issues over time due to carbon build up. To describe the thermal characteristics of a fuel reformer, the three main reformer types need to be introduced because each have different thermal characteristics.

1.2.1.1 CPOx Reforming

In catalytic partial oxidation (CPOx) reforming, fuel is combined with oxygen to partial oxidize the fuel into carbon dioxide and hydrogen. Complete combustion is avoided by providing an oxygen flowrate less than required for complete combustion. CPOx reforming is the easiest method to implement in SOFC systems. With oxygen already required in the system for the stack, there is not a large expense to provide a stream on oxygen to the CPOx reformer as well. Typically air is used rather than pure oxygen where the presence of nitrogen only dilutes the product H_2 and CO concentrations. The overall CPOx reaction follows reaction Eq. (1.9) which is applicable to any hydrocarbon. CPOx is a strongly exothermic process; thus, CPOx reforming provides a system-level source of thermal energy.

$$C_x H_y + \frac{1}{2} x O_2 \leftrightarrow xCO + \frac{1}{2} y H_2 \qquad \Delta H_{rxn} < 0 \tag{1.9}$$

1.2.1.2 Steam Reforming

Another typical reformer used in SOFCs is a steam reformer (SR). Steam reforming has the highest H_2 yield of the three reformer options. The difficulty with steam reforming lies in system integration. Steam reforming requires mixing water vapor with fuel in the reformer. Two methods prevail in adding steam to the SR. First, water can be supplied to the system, vaporized, and added to the fuel stream. This method requires the additional weight, cost, and volume associated with storing and supplying an additional

input stream to the system. The second method is to recycle a portion of the anode exhaust to the SR. Water vapor created within the stack is then provided to the SR. Added system cost and weight are low with this option, but it can be difficult to implement a control strategy. Fluctuations in anode exhaust gas need to be monitored to maintain a constant ratio of H_2O to fuel in the reformer. The overall steam reformer reaction follows reaction Eq. (1.10) which is applicable to any hydrocarbon. Steam reforming is a strongly endothermic process; thus, steam reforming provides a system-level sink of thermal energy.

$$C_xH_y + xH_2O_{(g)} \leftrightarrow xCO + \left(\frac{1}{2}y + x\right)H_2 \qquad \Delta H_{rxn} > 0 \tag{1.10}$$

1.2.1.3 Autothermal Reforming

The last reformer option is an autothermal reformer (AR). Autothermal reforming combines CPOx reforming and stream reforming by introducing both oxygen and water vapor to the fuel stream. The benefit of AR comes from a thermal management viewpoint as the steam-to-carbon ratio can be selected such that the overall reaction is thermally neutral. The downside to AR is that it has the lowest H_2 yield of the three reformers. AR is also the most complicated reformer to integrate into the system as in requires building in two additional inlet streams, oxygen and steam.

1.2.1.4 Selection and System Integration

Selection of a fuel reformer for a particular SOFC system is driven primarily by reformer size, system complexity, and thermal characteristics of the system. In larger SOFC systems designed for distributed power generation, the efficiency of a SR is very desirable. Small-scale systems designed for portable power and unmanned vehicles place a premium on size and weight; therefore, CPOx reformers are ideally suited. SOFC systems designed for auxiliary power units (APU) utilize a reformer than has an optimal balance between size, complexity, and controllability.

The other factor in choosing a reformer type is the thermal characteristics of the system. If the SOFC system is running inefficiently, transporting a large fraction of thermal energy to the environment, coupling a SR to absorb a portion of this otherwise unused energy will raise the system efficiency. Now, if excess fuel is being burned in the TGC to provide thermal energy to the system, integration of a CPOx reformer can supply heat to the system reducing the fuel input requirement. Autothermal reformers are thermally suited for systems that are neither creating too much or little thermal energy.

1.2.2 Tailgas Burner and System Integration

To take advantage of any electrochemically unutilized fuel leaving the stack, fuel in the anode exhaust is oxidized by cathode exhaust gases converting chemical energy in the fuel to thermal energy. TGC thermal energy is utilized within the system to preheat gas streams as well as supply energy to endothermic components. The most typical arrangement, as shown in Figure 1.7, is to flow TGC exhaust through a recuperative heat exchanger to preheat air bound for the cathode gas channels. The effectiveness of thermal integration between the TGC and recuperator varies with they system design. Typically, the thermal coupling occurs via flow conduit that connects exhaust gas from the TGC to the recuperator. A stronger thermal connection can be achieved by combining the TGC and recuperator into a single component where common walls are shared between the unit processes. By increasing the thermal coupling between TGC exhaust and process gas streams, less fuel needs to be burned in the TGC leading to an increase in system efficiency.

1.2.3 Recuperator and System Integration

To avoid excessive temperature gradients within the SOFC stack, oxidant needs to be preheated to a temperature near the SOFC operating temperature prior to entering the cathode. The main source of preheating occurs in a recuperative heat exchanger. Commonly, tailgas burner exhaust gas is the main source of thermal energy. Other

architectures can exploit the heat loss from other exothermic components such as the SOFC stack to preheat oxidant as well.

1.2.4 SOFC Stack and System Integration

Two methods of stack thermal integration are typically employed. First, the stack can be wrapped in high temperature micro-porous silica insulation. The benefit of stack insulation is the temperature field within the stack remains more uniform. The disadvantage is maintaining the stack temperature requires a greater amount of excess oxidant supplied to the cathode. This requires a larger ancillary power draw to operate the blower. The second thermal integration option is to couple the outer periphery wall of the stack to a system-level sink. For example, by flowing oxidant over the outer wall of the stack prior to entering the cathode, a recuperative heat exchanger can be coupled to the outer wall of the stack. This approach eliminates a discrete recuperator, increasing the power density of the system. Blower power is also reduced as convective cooling through excess oxidant flow is not the only mechanism to maintain the stack temperature.

1.3 Small-scale SOFC Systems

Small-scale SOFCs can be classified as any system producing anywhere from 100 W to 10 kW of power. Small-scale SOFCs have application in portable power, unmanned vehicles, and auxiliary power units (APUs). SOFCs are attractive in portable and unmanned applications as there power densities are greater than batteries for long duration missions. The high efficiency of SOFCs is attractive in APU applications where conventionally small-scale diesel generators or diesel engines at part load are used. The success of SOFCs in all of these applications requires a compact, high power density system. A representative schematic of a small-scale system is shown in Figure 1.8. High power densities are only achieved by creating system architectures with high packing factors[1].

[1] Packing factor is defined as the sum of individual volumes occupied by the system components to the total volume of the packaged system.

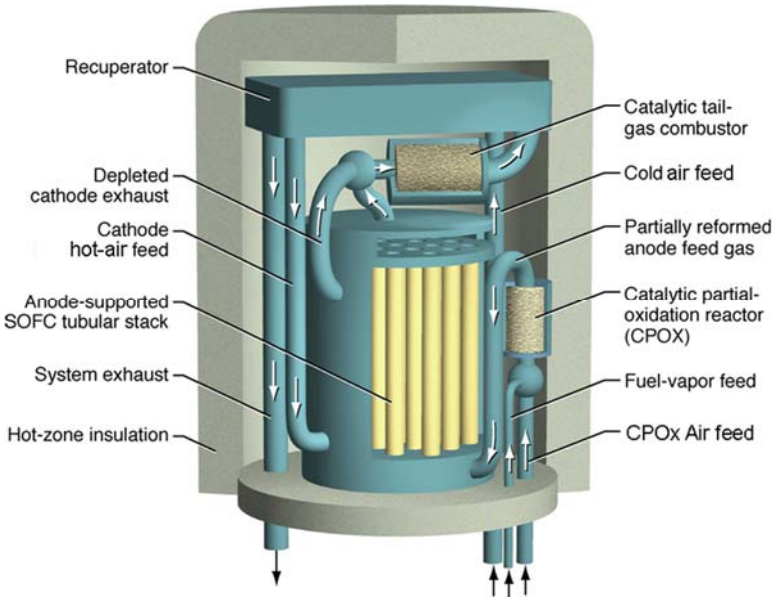

Figure 1.8 Diagram of a small-scale SOFC system. Stack is of tubular geometry.

Beyond a high packing factor, the SOFC system needs to be operating at a high system efficiency to achieve a high power density. The high operating temperatures of SOFCs combined with the required process gas heating requires an effectively thermally integrated system to achieve system efficiencies of 40-45%. The effect of thermal integration on system performance is most dramatic in small-scale SOFC systems. As systems become smaller in size, the ratio of surface area to volume increases. Thus, the rate of heat transfer to the thermal mass of a component increases resulting in an increased sensitivity of component performance to heat loss.

In small-scale SOFC systems, the physical space separating components is reduced leading to thermal interactions beyond that of a connection through process gas streams. Convective and radiation thermal energy exchange between system components acts to thermal couple all system components. An operating change in one component will have an effect on another due to a process gas connection as well as the thermal coupling between components. For example, the change in SOFC performance alters process statepoints throughout the system by virtue of the thermal interactions within the hotbox enclosure.

An SOFC system architecture needs to exploit the sinks and sources of thermal energy within the system by thermally coupling these processes. Thermal coupling can be enhanced by locating component sinks (recuperative heat exchanger) in close proximity to component sources (tailgas burner). A more direct means of thermal coupling is to combine system unit processes into a common component, thus sinks and sources of thermal energy are in close thermal contact, separated by walls alone.

1.4 Objectives and Approach

The primary objectives of this thesis are the development of thermally coupled SOFC system modeling tools and to demonstrate the capabilities of the models. Two distinct system models are developed both attempting to capture the thermal interactions between BoP and the SOFC stack. The first system model describes the thermal interactions within a small-scale planar SOFC system where each unit operation occurs in a discrete BoP component. The second system model describes the thermal interactions within a highly-integrated small-scale tubular SOFC system where common walls are shared between BoP and the stack. The approach to modeling each geometric configuration varies, but the overall goal is to create a modeling tool to aid in the thermal management of SOFC systems and to compare and contrast the advantages/disadvantages of SOFC geometries. Modeling results point to thermal management strategies to improve system metrics. These metrics range from reducing oxidant usage in unmanned vehicle applications to increasing overall system efficiency. The highly-integrated tubular system model incorporates a high-fidelity SOFC stack model which also provides a powerful tool in stack design.

The first SOFC system model thermally couples system components where each unit operation occurs within a discrete component, as in Figure 1.8. Heat loss from BoP and the SOFC stack is predicted with a quasi one-dimensional thermal resistance model. The thermal resistance model is coupled to a thermodynamic model of the system which predicts the system performance and required flowrates of fuel and oxidant. System components are thermally coupled via convection and radiation exchange within an

insulated enclosure surrounding the system. Convection heat transfer from all components occurs to a common gas temperature within the insulated enclosure, and radiation exchange from each component occurs to a common enclosure inner wall temperature. A single lumped temperature is assumed at each BoP component. A more rigorous treatment is given to the SOFC stack where radiation and convective heat transfer within gas manifolds is captured. Heat loss from the stack to the manifolds as well as conduction through stack insulation is then coupled to the overall system thermal resistance network.

The discrete SOFC thermally integrated model is executed on a system intended for an unmanned underwater vehicle (UUV). Model predictions illustrate the reduction in convective stack cooling via excess oxidant flow as the stack is able to shed thermal energy through conduction with a thermally integrated model. Oxidant flow predictions are very critical in UUV application where tanks are sized based on this requirement. Model predictions also highlight the distribution of oxidant heating with the stack as a large fraction occurs in the stack manifolds not just inside the cathode gas channels. Capturing heat transfer within stack manifolds and coupling this to the stack results in an increase in stack temperature gradients in comparison to a convectional adiabatic stack model. Lastly, the model allows different system operating strategies to be investigated where further reduction to oxidant consumption can be achieved.

The second thermally integrated system model is intended for highly-integrated tubular SOFC systems with power outputs up to 10 kW. This highly-integrated system model couples a high-fidelity SOFC stack model to BoP models. The SOFC stack model consists of a 1-D tubular cell model coupled to a 3-D computational fluid dynamics (CFD) model of the stack cathode. Variations in temperature and composition within the cathode are captured and their effect on cell performance within the stack is quantified. BoP components along with process flow conduits are coupled to the high-fidelity stack model to create a thermally integrated system model. First, the CFD domain is extended to include a recuperator, fuel/air preheat tube, and system insulation. CPOx and TGC

models complete the system each based on quasi one-dimensional thermal resistance models.

Simulation results of the highly-integrated system are useful in both system-level analysis and detailed stack analysis. System-level results highlight effective and non-effective coupling of thermal sinks to sources as a result of system architecture. The high-fidelity stack models provides a very powerful tool in stack design. It is seen that non-uniform cell performance occurs within the stack. The cause of cell performance variations is highlighted and model predictions can suggest methods of system operation and architecture to mitigate non-uniformities in cell performance. In this highly-integrated system, a strong thermal coupling exists between the stack performance and process statepoints throughout the system; therefore, a thermally coupled system model is a necessity to predict optimal system operating parameters. Improvements to operating parameters are suggested as a result of both a sensitivity analysis and parametric study.

CHAPTER 2

PREVIOUS MODELING EFFORTS

The successful design of an SOFC system is a two step process. The first step is to characterize a fuel cell stack that meets the power requirements of the desired application. Secondly, a system needs to be integrated around the stack and the subsequent system characterized in terms of its performance. Stack models provide information on the number of required cells and nominal operating temperatures of both the stack and inlet flows. System models provide required process gas temperatures and flowrates which can be used in sizing system components. Models representing both stacks and systems can be found in the literature, but they do have their shortcomings. A review of the current modeling efforts in planar and tubular stacks and systems is given below.

2.1 Stack Models

The building block of a stack model is the single cell model. A typical cell model represents an interior cell positioned in the middle of the stack. An interior cell is surrounded by other cells at approximately the same temperature leading to small temperature gradients between cells. An appropriate adiabatic boundary condition is imposed to represent an interior cell both in planar cells [3,4,5,6,7] and tubular cells [8,9]. An issue arises when the performance of the single cell is aggregated to all cells in order to represent a stack model. Cells located near the stack periphery will inevitably loss heat to the external stack surroundings. Heat loss to the surrounding will lower periphery cell temperatures, lowering power and causing overall stack power to decrease. Stack models need to capture heat loss to the surroundings at outer periphery cells in order to

accurately predict stack power as well as aiding in thermal integration of the stack into the system.

2.1.1 Planar

The majority of planar stack models aggregate the performance of a single interior cell to all cells within the stack [10,11]. In planar stacks, cells located near the top and bottom of the stack will inevitably loss heat to the surrounding external to the stack. While only one or two cells may experience any significant heat loss, overall stack power can be significantly affected for smaller scale systems. A limited number of models have incorporated some level of heat loss from the stack to the surroundings.

Chyou [12] performed a detailed analysis of the heat loss from a single planar cell to the surroundings. This model calculates heat loss from a single cell with an interconnect and insulation on both sides of the cell. A planar cell model is coupled to a 3-D model of the interconnect and insulation. Heat loss to the surroundings does occur but its effect on cell performance is not quantified. This model is also limited because it is for a single cell where heat transfer effects on performance will be greater than a boundary cell in a stack. Interior cells provide thermal energy to boundary cells acting to mitigate the decrease in performance that a single cell model would predict.

Beale [13] incorporated reactant and product gas manifolds into a ten-cell planar stack model. All boundaries surrounding the stack/manifold assembly are assumed adiabatic, but this model predicts the heat transfer between the gas manifolds and the stack. The focus of the model was on the velocity and pressure distributions in the gas manifolds; therefore, the effect of heat transfer from the stack on performance was not investigated.

Petruzzi [14] modeled the thermal interactions of a planar stack located inside a rectangular insulated enclosure. Radiation and convective heat transfer was modeled in-between the stack and the enclosure where radiation was modeled with a linearized

radiation heat transfer coefficient. Heat exchange between the stack and enclosure was simplified by utilizing the average temperatures of both in determining the driving potential. Heat is then shed to the external surroundings of the insulated enclosure. Transient simulation results reveal the effect edge heat transfer has on the temperature profile of the cell. This type of stack model is useful in calculating total stack heat loss, but it needs to be coupled to a complete system thermal model in order to capture the effect stack heat loss has on process gas temperatures entering the stack and the temperature external to the enclosure.

2.1.2 Tubular

The number of tubular stack models is limited in comparison to planar stacks. The majority of tube models that do exist utilize the deign layout of the Siemens Westinghouse tube. A schematic of the Siemens tube design is shown in Figure 2.1, details on oxidant and fuel delivery are not shown. Oxidant preheats in the central tube before being exposed to the cathode surface. Fuel flows external to the tubular cell. Cells are connected via interconnects to create a stack and a single fuel volume is shared within the entire bundle.

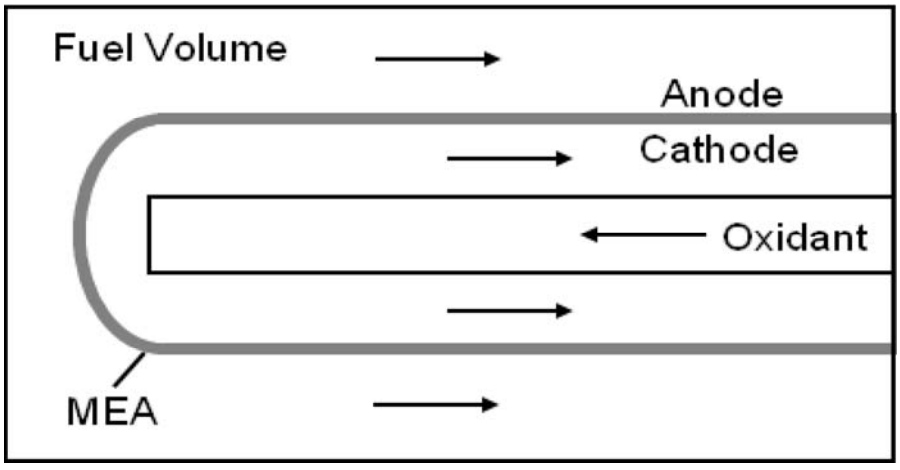

Figure 2.1 Schematic of a single Siemens Westinghouse tubular cell

While radiation is a contributing factor in heat exchange between the MEA and the oxidant feed tube [8], radiation exchange between cells is not modeled when an interior cell is used to represent the entire stack. Radiation external to the MEA is assumed negligible because a centrally located cell only sees more cells at roughly the same temperature. In tubular stacks, a larger number of cells are located at the stack periphery where tubes experience radiation exchange with the walls enclosing the fuel volume. A decrease in overall stack power due to edge effects will be more dramatic in tubular stacks than planar stacks because of the increased percentage of edge cells. Sanchez [9] reports that a 2-3% penalty to total stack power can occur when the effects of tubes near the periphery are taken into account. This penalty is based on large arrays of Siemens Westinghouse tubes, when smaller scale stacks are considered the penalty will increase because a larger fraction of cells are at the stack periphery.

Models intended for tubular SOFC stacks are limited. Kee [15] presented a heat transfer model for a small-scale stack geometry in which fuel flows interior to and oxidant flows exterior to the cells. In contrast to the Siemens design, no oxidant preheat tube is used and all cells share a common cathode gas volume. In this simplified model, a constant heat generation rate is applied to each cell which must dissipate all heat via convection and radiation from the outer surface of the cell. Parametric studies varying the convective heat transfer coefficient and the emissivity of the cells all resulted in radiation accounting for 75-82% of total heat transfer. This approach does highlight the significance of radiation in small-scale tubular stacks, but a constant heat generation rate is not appropriate to predict stack power. The heat transfer model needs to be coupled to the electrochemistry within the cell to accurately predict stack performance.

Another area in which the entire tubular stack has been studied is in micro-tubular stacks, < 100W. In these studies, each cell is simulated separately, but adiabatic conditions are applied to the wall enclosing the array of tubular cells [16,17]. The micro-tubular system geometries are very similar to that investigated by Kee. Fuel directly enters the inner diameter flow region of the cell and oxidant directly enters the flow region external to the cell. Because a large ΔT in the system is not seen with the

adiabatic boundary condition, radiation is also typically neglected in micro-tubular stack models [16]. The usefulness of micro-tubular stack results is limited because radiation will be shown to be dominant in tubular SOFC stacks.

2.2 System Models

The creation of an effectively thermally integrated SOFC system requires a system-level model that captures thermal interactions between components. Modeling efforts must go beyond simply connecting components through process gas flows. Heat transfer from components to their surroundings must be incorporated in order to predict component interactions within the system.

The most common SOFC system models impose adiabatic boundaries on all components [18, 19, 20, 21, 22]. Component to component thermal interactions are only captured in the interconnections of process gas flows. Adiabatic systems are relatively easy to create as they are based on thermodynamic models and due not require knowledge of the system dimensions. Adiabatic systems are useful in providing ballpark values such as the number of required cells and BoP loads to reach a given power output, but they are not able to guide developers in system design and layout.

There are thermodynamic based system model that calculate heat transfer from certain system components [23]. Any heat transfer is not rate based but a result of an energy balance around a component given a specified inlet and outlet state. These results give SOFC developers an idea of the required heat loss from a component in order to achieve a given state, but no insight is provided on how to achieve the required heat transfer.

The next step in predicting heat loss within the system is to apply rate based equations to predict component heat transfer. Chan [24] applied rate based heat transfer equations to the stack and burner where all stack heat transfer was directly to the surroundings. Heat loss from the burner was distributed to vaporize water and provide

thermal energy to the reformer with the remaining heat loss transferred to the surroundings. The distribution of burner heat loss was calculated with thermodynamic energy balances not based on heat transfer rate equations of a vaporizer or reformer. Lu [25] also used a thermal resistance to calculate heat loss from the stack to the surroundings. Burke [26] created an SOFC system model for an unmanned underwater vehicle where stack heat loss via convection and radiation occurs to the inner hull. The limitation to theses system models is that component heat loss is not coupled as heat transfer occurs to a surroundings at a fixed constant temperature.

All of the above mentioned SOFC system models are limited in system design because they lack thermal coupling between system components. Without thermal coupling, system architectures designed to coupled system-level sinks and sources can not be evaluated. Thermal interactions become stronger as system sizes are reduced; therefore, a thermally coupled system is a necessity to accurately predict the performance of small-scale SOFC systems. Two thermally coupled system models that overcome the shortcomings of previous modeling efforts are presented in the remainder of this thesis.

CHAPTER 3

PLANAR SOFC SYSTEM MODEL

In this chapter, a thermally coupled system model is developed and employed on a small-scale planar SOFC system. This system model is applicable to SOFC system designs utilizing discrete components. A discrete system is characterized by each BoP unit operation and the stack as being physically separate components. Because there is a spatial separation between all components, a lower-order thermal resistance based model is employed to thermally couple system components.

3.1 Objectives and Approach

The overall objective for this system model is to investigate the steady-state thermal interactions among components in planar SOFC systems and to facilitate thermal integration of these components for successful system design. The model allows for system configurations to be evaluated on a thermal management level. Selection of optimal system-level operating parameters is also aided through modeling results. System components include an electrochemical cell-stack, fuel reformer, recuperative heat exchanger, and catalytic burner all packaged within a hot enclosure. The cell-stack is the largest in size of any component in small-scale SOFC systems and its relatively high heat transfer area and high operating temperature cause strong thermal interactions with the smaller BoP hardware. Thus, one motivation in model development is to capture these effects in order to quantify the sensitivity of system processes to SOFC stack operating temperature and design configuration. Considering the dominant role of the cell-stack in thermal management, the modeling strategy focused on enabling feedback of heat transport from/to both the BOP hardware and the SOFC stack.

Details of the developed stack thermal model are presented first, followed by a description of how the stack thermal model is extended to the system thermal model to include the BoP components. The resulting thermal model of the system is connected to a system-level thermodynamic process design model to enable a better understanding of how component heat loss affects process gas temperatures and flow requirements throughout the system. The resulting model is exercised on a ~1 kW SOFC system intended for mobile power applications. System performance sensitivity is examined for various thermal management strategies that involve altering the convective and radiative heat transfer in the enclosure. The impact of these measures on internal temperature distributions within the cell-stack is also studied.

3.2 SOFC Stack Module Thermal Model

The objective of SOFC stack thermal modeling is to estimate the stack surface heat loss that inevitably occurs but is not captured by the typical assumption of adiabatic stack operation. The stack thermal model begins with a simplified view of the stack assembly (repeating cell units, compression plates, and manifolding) and the insulation that is wrapped around the stack assembly as shown in Figure 3.1. The combination of the stack assembly and insulation is referred to as the stack module. The stack under investigation is in a counter-flow arrangement, but the methodology given herein could easily be applied to co-flow configurations. Reactant and product gases enter the stack module through slots in the insulation and distribute inside manifolds before entering the anode/cathode flow channels. In practice, the internal manifolding of the stack separates anode and cathode streams in much the same way as a counter-flow plate-fin heat exchanger, but in this simplified viewpoint, the manifold is considered an open volume where separation of oxidant and fuel streams is ignored. This is a valid assumption in the thermal model as separation of the streams occurs with high thermal conductivity metals.

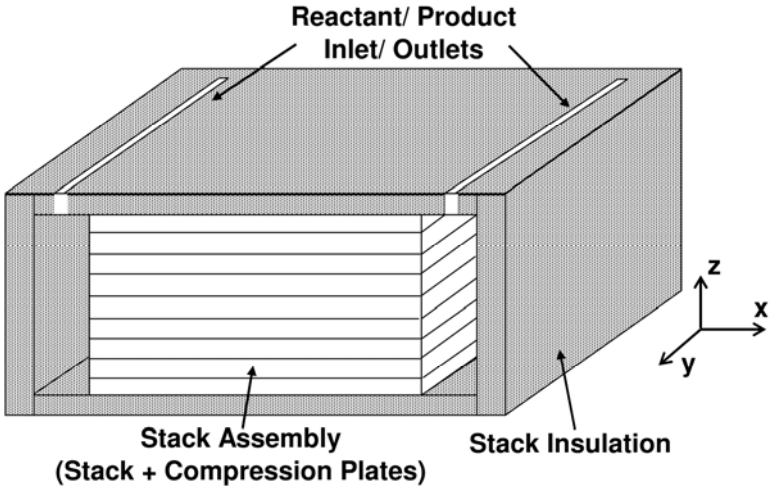

Figure 3.1 Cut view of the planar stack module

The stack module geometry in Figure 3.1 yields four sides of the stack assembly that are in intimate contact with insulation and two stack assembly sides which are adjacent to the gas manifolds. These six stack assembly sides represent the internal thermal boundary conditions for the stack module thermal model. The thermal boundary conditions are specified by stack boundary temperatures calculated with a previously developed [2,27] 1-D planar cell model that is incorporated within the thermodynamic system model. A schematic of the stack without manifolding and insulation is given in Figure 3.2 and includes the discretization of the 1-D model in the direction of reactant gas flow.

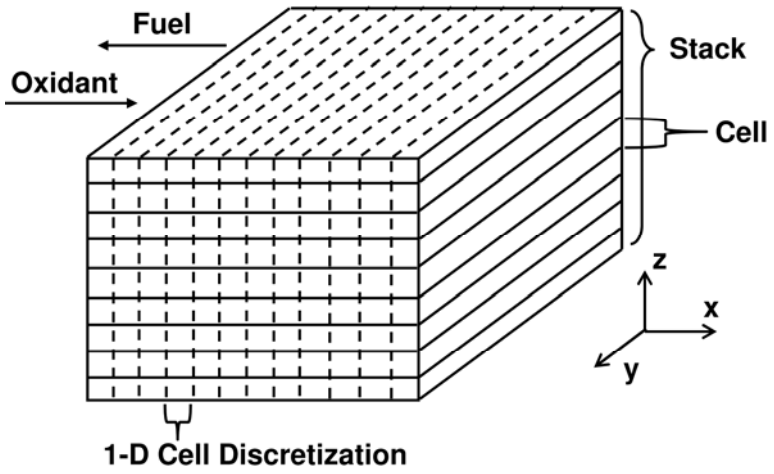

Figure 3.2 Counter-flow 1-D planar stack model

Solution to the 1-D cell model yields a streamwise temperature profile. In this stack modeling approach, the performance of a single cell is aggregated to represent the entire stack resulting in a streamwise stack temperature profile (i.e., along x in Figure 3.2) and no temperature gradients normal to stack gas flows (along y and z in Figure 3.2). Beale et al. [13], developed a reduced order distributed resistance analogy model to study a cross-flow stack with rectangular manifolding. While Beale considered an adiabatic stack assembly, it was found that the gases in the stack inlet and outlet manifolds did not register significant temperature gradients along the z axis (see Figure 3.2). Beale's results support the use of a 1-D stack model in the present study. With the existence of a streamwise temperature profile, it would be inaccurate to use a single average surface temperature to represent the six sides of the stack.

A lumped, area-averaged cell temperature is assumed at the four stack assembly surfaces that are in intimate contact with stack insulation, i.e., the four external stack surfaces that are not exposed to inlet/exit manifold gas flows. (Note this approach assumes the top and bottom compression plates are also at same temperature as the stack.) The validity of using an area-averaged cell temperature rather than the 1-D profile was tested. As these four stack sides are in contact with insulation, the total conductive heat flux from an area-averaged surface and a 1-D discretized surface was calculated. Utilizing an area-averaged temperature, total heat flux was observed to be within 0.2% of the discretized surface for a given ambient temperature.

The remaining two sides of the stack serve as the reactant gas inlet/outlets to the repeating cell elements and are adjacent to the gas manifolds. Temperature boundary conditions of the stack adjacent to the gas manifolds are provided by the temperature at the inlet/outlet of the 1-D planar cell model. Cross-plane temperature differences of less than 1°C in SOFCs [28], allow for the cell trilayer temperature to be lumped in the 1-D cell model. The interconnect temperature is also resolved; therefore, the 1-D model yields two temperature profiles, a trilayer and an interconnect profile. This results in two surface boundary temperatures at each stack side adjacent to the manifolds.

With the internal temperature boundary conditions to the stack module thermal model defined, the thermal resistance network accounting for heat transfer within the gas manifolds and stack insulation is discussed in the following sections. This thermal resistance network ties the boundary temperature of the six stack sides to the temperatures at the external surfaces of the stack insulation.

3.2.1 Gas Manifolds: Radiation Heat Transfer

High SOFC operating temperatures point to radiation as a substantial heat transfer mechanism; therefore, a radiation heat transfer mechanism is incorporated into the thermal resistance model of the gas manifolds. Radiation heat exchange in a manifold is assumed to occur between the five insulation surfaces and the adjacent stack side that make up the manifold enclosure (see Figure 3.3). All surfaces are assumed opaque, diffuse, and gray. Slots in the insulation for reactant/product gases entering the manifold are relatively small and are added to the top surface area of the manifold, creating a complete enclosure.

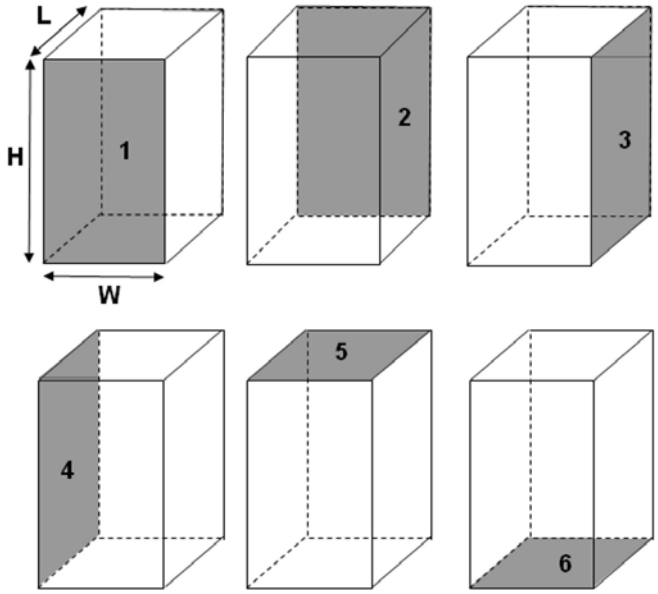

Figure 3.3 Illustration of a single gas manifold enclosure with surfaces labels

The end surfaces of the stack adjacent to the manifold (i.e., at x = 0 and x = L in Figure 3.2) are composite surfaces composed of cell trilayers (cathode-electrolyte-

anode/anode support), interconnects, gas flow channels, and compression plates as shown in Figure 3.4. Rather than discriminate between each trilayer surface inside the gas distribution manifold, all stack trilayers are lumped into a single surface. Similarly, each interconnect in the stack is lumped into a single interconnect surface and each cell gas channel is lumped into a single gas channel surface. Because of small areas and view factors relative to the manifold enclosure, gas flow channels are assumed to be irradiating surfaces. Compression plates are lumped into the interconnect surface because of comparable radiation properties due to similar metallic construction materials. This yields eight surfaces comprising each gas cavity enclosure (5 insulation surfaces and 1 stack surface that is decomposed into 3 separate surface areas). Enclosure view factors are calculated using relations for aligned parallel rectangles and perpendicular rectangles with a common edge [29] and are summarized in Table 3.1.

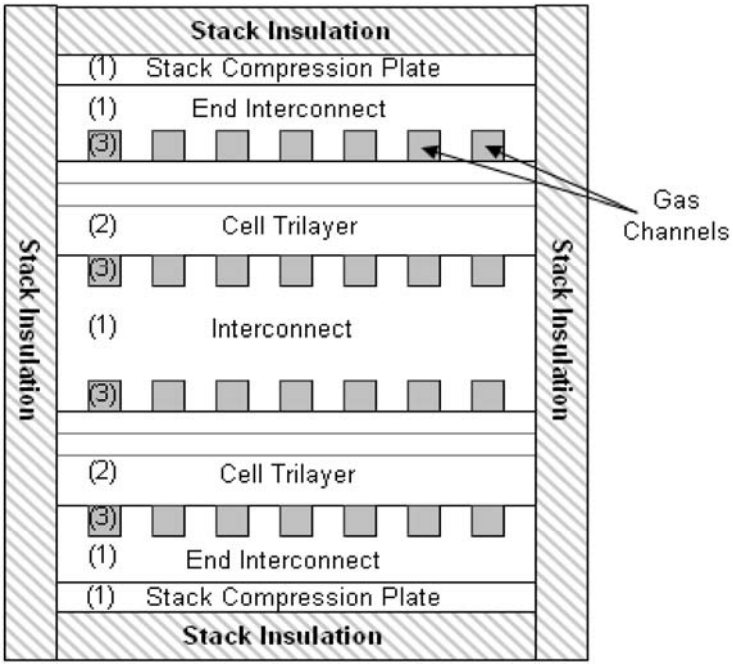

Figure 3.4 Illustration of the stack surface adjacent to the gas manifolds. The figure illustrates how the repeating cell structure is seen as a composite surface where all cell trilayers are grouped into surface 2. Stack interconnects are grouped into surface 1, and gas channels are grouped into surface 3.

Table 3.1 Manifold Enclosure View Factors, *Fij*

		i					
		1	2	3	4	5	6
j	1	0.000	0.031	0.039	0.039	0.052	0.052
	2	0.031	0.000	0.039	0.039	0.052	0.052
	3	0.462	0.462	0.000	0.891	0.446	0.446
	4	0.462	0.462	0.891	0.000	0.446	0.446
	5	0.022	0.022	0.016	0.016	0.000	0.005
	6	0.022	0.022	0.016	0.016	0.005	0.000

Surface 3 in Figure 3.3 serves as the composite cell surface in the left manifold and is comprised of irradiating gas channels, radiating trilayers, and radiating interconnects/compression plates. As discussed earlier, all stack trilayers are lumped into a single trilayer surface (surface 2 in Figure 3.4). The same lumping procedure follows for interconnects and gas channels (surfaces 1 and 3 respectively in Figure 3.4). Because trilayers, interconnects, and gas channels are tightly spaced and repeated throughout the stack, the view factors for the composite surface are computed as follows.

From stack composite surfaces to manifold insulation surfaces:

$$F_{tri,j} = F_{ic,j} = F_{chan,j} = F_{3,j} \tag{3.1}$$

From manifold insulation surfaces to stack composite surfaces:

$$F_{j,tri} = \frac{A_{tri}}{A_3} \cdot F_{j,3} \tag{3.2}$$

$$F_{j,ic} = \frac{A_{ic} + A_{comp\ plates}}{A_3} \cdot F_{j,3} \tag{3.3}$$

$$F_{j,chan} = \frac{A_{chan}}{A_3} \cdot F_{j,3} \tag{3.4}$$

where F_{ij} is the view factor from surface i to j and A_i is the surface area of surface i.

Focusing on a single manifold, radiosity balances on all eight manifold surfaces produce a set of equations in which surface radiosities are calculated.

For radiating surfaces, i:

$$\frac{\sigma T_i^4 - J_i}{\frac{1-\varepsilon_i}{\varepsilon_i A_i}} = \sum_{j=1}^{8} \frac{J_i - J_j}{\left(A_i F_{ij}\right)^{-1}} \tag{3.5}$$

For irradiating gas channel surface, i:

$$0 = \sum_{j=1}^{8} \frac{J_i - J_j}{\left(A_i F_{ij}\right)^{-1}} \tag{3.6}$$

where J_i is the radiosity at surface i and ε_i is the emissivity of surface i.

Net radiation heat transfer leaving each surface in the manifold is calculated as,

$$\dot{Q}_{rad,i} = \frac{\sigma T_i^4 - J_i}{\frac{1-\varepsilon_i}{\varepsilon_i A_i}} \tag{3.7}$$

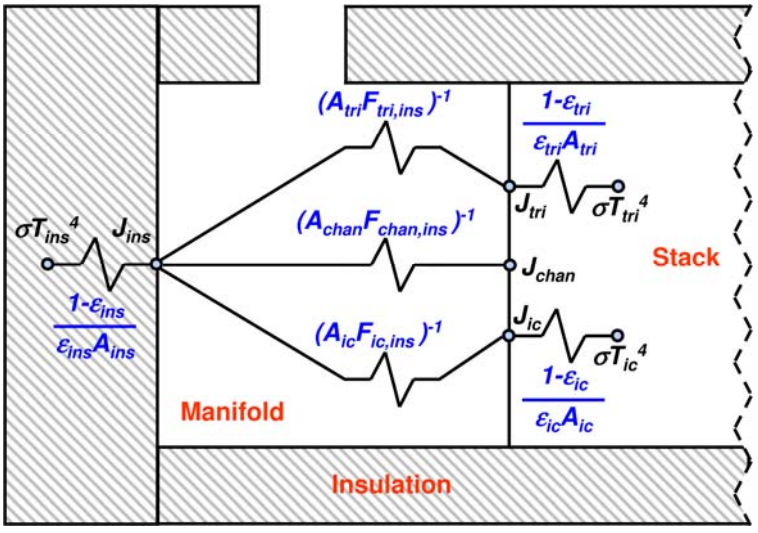

Figure 3.5 Radiation resistance model within gas manifolds. For figure clarity, only radiation exchange between the composite stack surface and adjacent insulation surface is shown.

The lumped thermal radiation resistance model for the left manifold in Figure 3.1 is shown in Figure 3.5. For simplicity, radiation exchange is only shown between the composite stack surface and the manifold surface parallel to the stack. An equivalent radiation resistance network models the interactions between all surfaces in each manifold enclosure. In total, there are eight surfaces per manifold: five manifold insulation surfaces, and 3 lumped surfaces representing the face of the cell-stack (trilayers, interconnects, and gas channel openings).

3.2.2 Gas Manifolds: Convection Heat Transfer

A convective heat transfer resistance model is coupled to the radiation resistance model within each gas manifold. Convection occurs from each lumped surface of the radiation model except for the gas channels lumped surface. Heat transfer due to convection leaving each surface *i* is calculated by,

$$\dot{Q}_{conv,i} = h_{man} A_i \left(T_i - T_{man,gas} \right) \tag{3.8}$$

where A_i is the surface area and T_i is the temperature of surface *i*, h_{man} is the heat transfer coefficient and $T_{man,gas}$ is the temperature of the stack manifold gas. Assuming a perfectly mixed condition inside the cavity, the amount of heat added to the resistance network is calculated as,

$$\dot{Q}_{man,gas} = \dot{m}_{man,gas} \cdot cp_{man,gas} \left(T_{gas,in} - T_{man,gas} \right) \tag{3.9}$$

where $\dot{Q}_{man,gas}$ is the thermal energy transported from manifold gas, $\dot{m}_{man,gas}$ is the flow rate in a stack manifold, $cp_{man,gas}$ is the heat capacity and $T_{man,gas}$ is the temperature of the manifold gas, $T_{gas,in}$ is the temperature of gases entering the manifold.

Oxidant flow is generally an order of magnitude greater than fuel flow in SOFCs; therefore, the mass flow rate and temperature of oxidant (not the fuel) is used in Eq. (3.9). At the oxidant inlet manifold of the stack module, $T_{gas,in}$ is the oxidant temperature entering the stack module and $T_{man.\ gas}$ is the temperature of oxidant entering the cathode

compartment of the cell. At the oxidant outlet manifold of the stack module, $T_{gas,in}$ is the oxidant temperature leaving the cathode and $T_{man.\ gas}$ is the oxidant temperature leaving the stack module.

A convection resistance network for the left manifold in Figure 3.1 is shown in Figure 3.6 using the surface numbering scheme of Figure 3.3. An equivalent network is written for the right manifold.

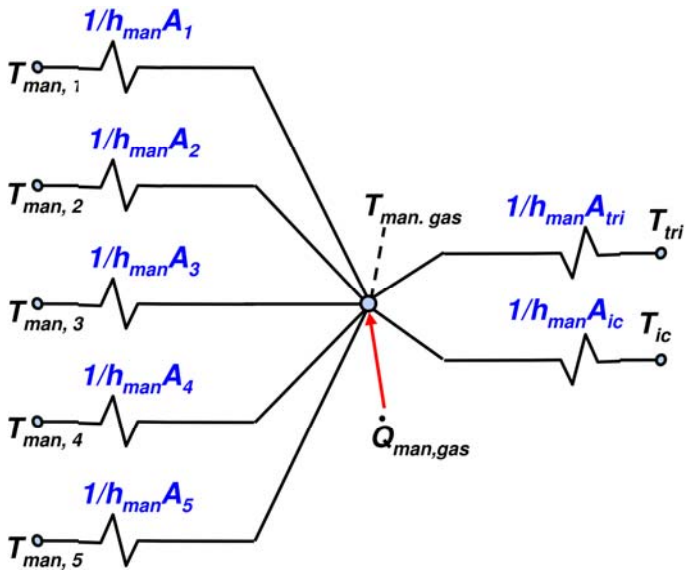

Figure 3.6 Gas manifold convection resistance network for a single manifold

Energy balances on each manifold surface combine the radiation and convection resistance models and results in the amount of thermal energy entering each surface,

$$\dot{Q}_{in,i} = -(\dot{Q}_{rad,i} + \dot{Q}_{conv,i}) \tag{3.10}$$

3.2.3 Stack Insulation Conduction

The manifold thermal resistance models result in 10-inner insulation surface temperatures (5 per gas manifold). As stated earlier, the four sides of the stack in intimate contact with insulation (see Figure 3.1) are lumped into a single surface at the area-averaged stack temperature. The inner surface of the insulation surrounding the stack and manifolds is described by 11 lumped surface temperatures. Connected the

inner surface to the external insulation surface is accomplished by calculating the conduction heat transfer from each surface. The conduction heat transfer equation below is written for each of the 11-inner insulation lumped surfaces,

$$\dot{Q}_{cond,i} = \frac{kA_i}{L_i}\left(T_{i,inner} - T_{i,outer}\right) \tag{3.11}$$

where k is the thermal conductivity, $T_{i,inner}$ and $T_{i,outer}$ are the inner and outer insulation surface temperatures of region i, respectively, and L_i is the insulation thickness of region i.. A_i is the average surface area of the inner and outer surfaces of region i.

It is conceivable to connect the 11-inner insulation lumped surfaces to 11-outer insulation lumped surfaces. This approach adds complexity in connected the SOFC thermal module to the remaining system. To reduce the number of external lumped surfaces on the stack insulation, conduction from manifold sides 1, 2, 5, & 6 in Figure 3.3 and conduction from the insulation surface in intimate contact with the stack occurs to a common outer insulation temperature. Thus nine inner insulation surfaces are connected through conduction to a common outer insulation lumped surface. The result is to reduce the number of outer insulation lumped surfaces to three (A, B, and C) as shown in Figure 3.7. The three surfaces depicted are two shaded end surfaces B and C along with the four un-shaded insulation sides that comprise the third surface, A. The conductive resistance network representing the stack insulation is shown in Figure 3.8. In the resistance network shown, right refers to the right manifold and left refers to the left manifold in Figure 3.1.

Allowing conduction to a common outer insulation surface A from the nine inner insulation surfaces has little effect on overall heat transfer. Assuming three outer insulation surfaces results in less than a 0.10% difference in total stack module heat loss compared to using eleven outer insulation surfaces. The three stack insulation skin temperatures are connected to the overall SOFC system thermal model as described in Section 3.3.

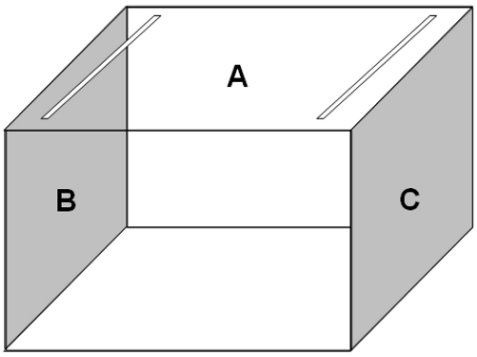

Figure 3.7 Illustration of the three lumped surfaces representing the external area of the insulated stack assembly

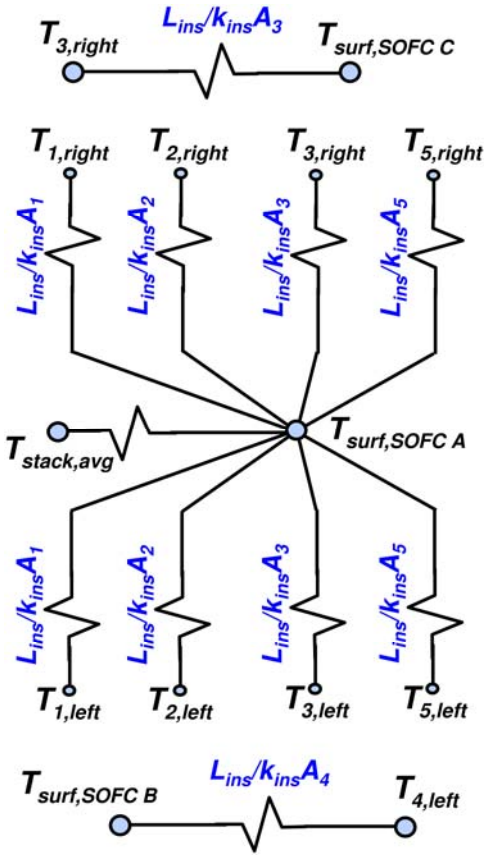

Figure 3.8 Stack insulation conduction model showing the connection between 11-inner insulation lumped surfaces to 3-outer insulation lumped surfaces

3.2.4 Coupling Heat Transfer to Electrochemical Stack Model

The heat transfer predicted with the stack module thermal model needs to be coupled to the 1-D electrochemical stack model. Within the gas manifolds, heat transfer is

predicted at both the inlet/outlet ends of the interconnects and trilayers. Thermal energy exchange with the gas manifolds is evenly distributed as a heat flux boundary condition to the interconnect and trilayer energy balances at the inlet/outlet of the 1D cell model. Conduction heat transfer also leaves the stack at the four stack sides in intimate contact with insulation. Conductive heat transfer is evenly distributed as a heat flux boundary condition to the cathode gas channel energy balance at all interior cell control volumes. Conduction heat transfer is removed from the cathode gas channel because in SOFCs convective cathode gas cooling is the dominate stack cooling method.

3.2.5 Summary of Stack Model Assumptions and Impacts

Assumptions made in development of the SOFC stack thermal model are summarized below.

1. Extrapolation of single-cell performance as predicted by 1-D model for entire stack and uniformly distributed reactant gases are assumed.
2. Radiation exchange in gas manifolds assumes opaque, diffuse, and grey surfaces, with non-emitting transparent gases.
3. Internal manifolding separating anode and cathode streams neglected due to its high thermal conductivity.
4. Cell repeating trilayers, interconnects, and gas channels are lumped to form three surfaces in each manifold.
5. Gas channels are considered irradiating surfaces due to relatively small view factors and areas with respect to remaining manifold surfaces.
6. Reactant gases are perfectly mixed in manifolds with the dominant reactant flow assumed to be that of cathode gas flow.
7. Fuel flow within the stack manifolds is considered to be adiabatic.
8. External insulation skin defined by three lumped surface temperatures.

Utilizing a 1-D stack model does not lend itself to identifying localized stack hot/cold zones, but this approach is sufficient in predicting nominal stack performance characteristics, temperature gradients, and heat rejection. Larger localized temperature

gradients are likely to arise than predicted by this model, but experimental knowledge would allow for appropriate scaling factors to be applied in predicting higher localized gradients. Neglecting detailed internal manifolding geometry allows radiation view factors to be calculated with relative ease, but is expected to result in an over-prediction of radiation heat transfer because internal manifolding is an additional resistance to radiation thermal energy exchange. Lumping of stack repeating surfaces in each manifold is appropriate for a 1-D stack model. Anode gas flow is excluded in manifold gas mixing because anode flow is an order of magnitude less than cathode flow; its exclusion has little impact on thermal capacity and temperature of cavity gases. Perfectly mixed manifold gas is supported by previous work where the largest temperature difference in similar rectangular manifolds was seen to be 26°C [13].

3.3 System Thermal Model

A thermal model of the SOFC system components within the hot enclosure (see Figure 3.10) was also developed for a power system representative of mobile and small stationary applications. The system thermal model predicts the heat loss or gain from system components and ties the magnitude of heat transfer to a thermodynamic model of the system. Heat transfer from system components does not occur independently as the thermal model thermally couples all components.

The system thermal model assumes a lumped, uniform surface temperature for all balance of plant components and enclosure surfaces and accounts for conduction, convection, and radiation heat transfer mechanisms. The SOFC stack is comprised of three lumped surface temperatures as described above and shown in Figure 3.7. System piping is assumed insulated and adiabatic except in the fuel piping, most notably between the reformer (catalytic partial oxidation, CPOx, unit) and SOFC.

Conduction heat transfer occurs in the system as each BoP component as well as the hot enclosure are wrapped in insulation. Convection heat transfer occurs between system components and the enclosure (or hot box) cavity gas. Lastly, radiation heat transfer

occurs between system components and the enclosure inner wall. *Importantly, component-to-component radiative interactions are assumed negligible compared with the interaction between a single component and the surrounding enclosure walls.* The validity of this assumption is largely dependent on system packaging. The more closely the components are packaged next to one another (i.e., high packing efficiencies[2]), the more consideration must be given to component-to-component interactions. The net heat transfer from BoP components is written in terms of a temperature difference divided by the overall resistance as follows,

$$\dot{Q}_{Total,i} = \frac{T_i - T_{skin,i}}{R_{ins,i}} \tag{3.12}$$

$$\dot{Q}_{Conv,i} = \frac{T_{skin,i} - T_{cav,gas}}{R_{conv,i}} \tag{3.13}$$

$$\dot{Q}_{Rad,i} = \frac{Tskin,_i - T_{HB,i}}{R_{rad,i}} \tag{3.14}$$

$$\dot{Q}_{Total,i} = \dot{Q}_{Conv,i} + \dot{Q}_{Rad,i} \tag{3.15}$$

where $\dot{Q}_{Total,i}$ is the rate of heat transfer from component *i*, T_i is the lumped inner wall surface temperature of component *i*, $T_{skin,i}$ is the insulation surface temperature of component *i*, $T_{cav,gas}$ is the hot box cavity gas temperature, and $T_{HB,i}$ is the inner hot box surface temperature. The net heat transfer rate from the SOFC stack is similarly calculated using the surface temperatures calculated in the stack thermal model, where Eqs. (3.13) thru (3.15) are written for the three stack insulation skin surfaces.

Figure 3.9 provides an illustration of the details of the thermal resistance network model between the catalytic burner and the surroundings. Heat is transmitted via conduction through insulation surrounding the burner. Surface heat flux from the outer surface of the component reflects the combined modes of radiation and convection heat transfer. Radiation heat flux between the burner outer skin surface and the enclosure

[2] "high" packing efficiencies are typically >65% where packing efficiency is defined as the sum of component volumes divided by the total enclosure volume.

assumes grey diffuse surfaces with an assumed view factor of 1.0 and a linearized radiation heat transfer coefficient.

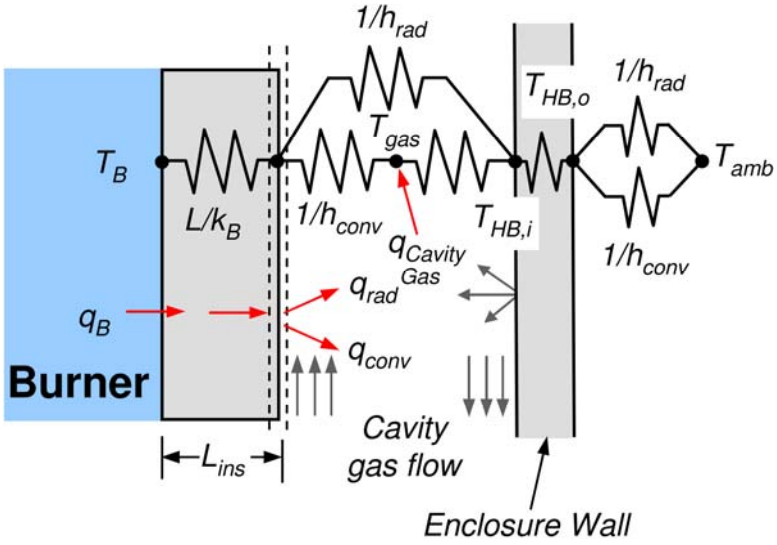

Figure 3.9 Illustration of heat transfer pathways from the burner to the ambient conditions surrounding the system enclosure

The equivalent heat transfer resistance for the burner is expressed as,

$$R_{tot,B} = \frac{L_B}{k_B A_{B,i}} + \frac{1}{h_{rad,B} A_{B,o} + \left(\frac{1}{h_{conv,B} A_{B,o}} + \frac{1}{h_{conv,HB} A_{HB,i}} \right)^{-1}} + \frac{L_{HB}}{k_{HB} A_{HB,i}} + \left(h_{conv,amb} A_{HB,o} + h_{rad,amb} A_{HB,o} \right)^{-1} \quad (3.16)$$

A thermal resistive network for the entire hot box can be developed from this basic framework by coupling each of the components to the inner hot box wall temperature, $T_{HB,i}$ and cavity gas temperature $T_{cav,gas}$. Figure 3.10 depicts the resistive network for the entire SOFC system thermal model. Components in the hot box include the SOFC stack, catalytic burner, CPOx reformer, and the recuperator. Balance of plant components within the hot box approximate their inner wall surface temperature by taking an average gas temperature. The small resistance, compared to insulation resistance, associated with the metallic outer wall of each BoP component (i.e. adjacent to the inner insulation surface) is neglected. The stack insulation surface temperatures are outputs from the

stack thermal model. *Components are indirectly coupled through convection* at the cavity gas temperature by applying an energy balance to the hot box cavity gas node,

$$\sum_i \dot{Q}_{Conv,BoP,i} + \sum_i \dot{Q}_{Conv,Stack,i} + \dot{Q}_{Conv,HB,i} + \dot{Q}_{Cav,Gas} = 0 \tag{3.17}$$

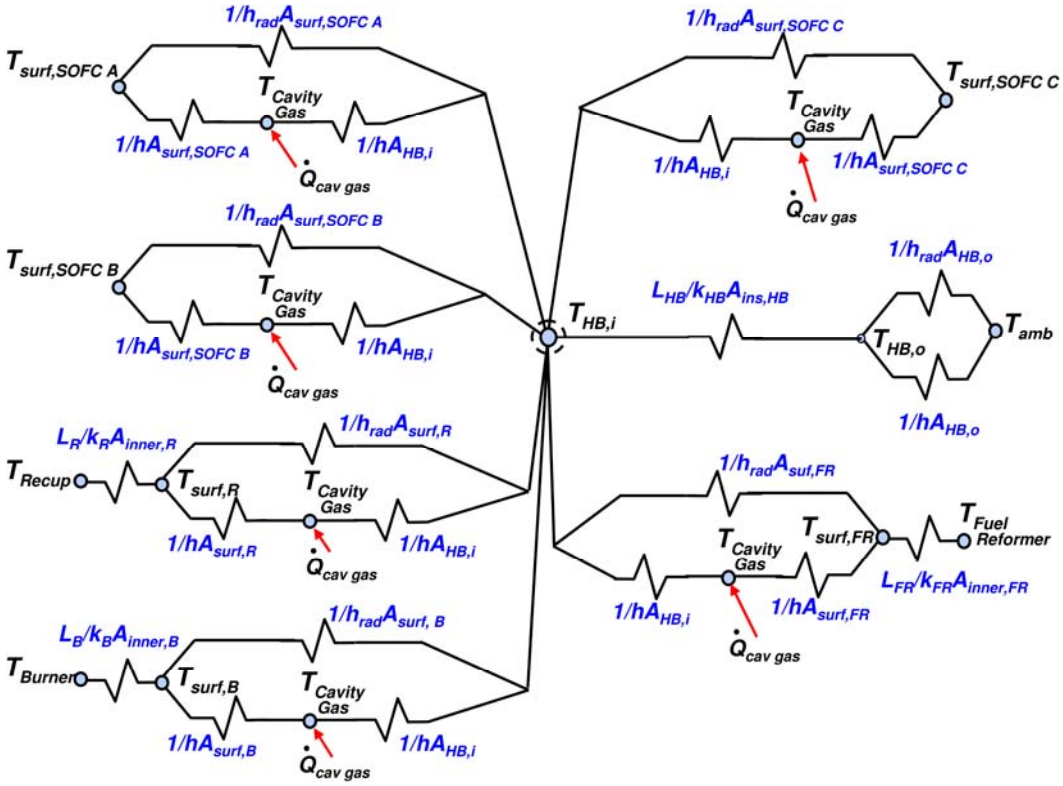

Figure 3.10 System thermal resistance model thermally coupling system components

System configurations arise where stack exhaust gases leaving the recuperator may be circulated inside the hot enclosure before being plumbed out of the enclosure. To allow for circulating cavity gas flow, a perfectly mixed condition inside the enclosure is considered where the amount of heat added to the resistance network is calculated as,

$$\dot{Q}_{cav\ gas} = \dot{m}_{cav.gas} \cdot cp_{cav.gas} \left(T_{gas\ in} - T_{cav.gas} \right) \tag{3.18}$$

where $\dot{m}_{cav.gas}$ and $T_{gas\ in}$ are the state of exhaust leaving the recuperator, $T_{cav.gas}$ is the temperature of cavity gases within the hot enclosure, and $cp_{cav.gas}$ is the average specific heat calculated at the inlet and cavity gas temperatures.

Components are also indirectly coupled though radiation by a common interaction with the inner surface of the enclosure wall. This coupling is achieved by applying an energy balance to the hot box inner wall node as follows,

$$-\dot{Q}_{\mathrm{Conv},HB,i} + \sum_i \dot{Q}_{Rad,BoP,i} + \sum_i \dot{Q}_{Rad,Stack,i} = \dot{Q}_{HB,out} \tag{3.19}$$

$$\dot{Q}_{Conv,HB,i} = \frac{T_{HB,i} - T_{cav,gas}}{R_{Conv,HB,i}} \tag{3.20}$$

$$\dot{Q}_{HB,out} = \frac{T_{HB,i} - T_{amb}}{R_{Ins,HB} + R_{amb}} \tag{3.21}$$

where $\dot{Q}_{HB,out}$ is the rate of heat transfer leaving the hot box to the surroundings. R_{amb} is the heat transfer resistance from the hot box outer skin to the surroundings; it can include any combination of radiation and convection.

3.3.1 Summary of System Model Assumptions and Impacts

Assumptions made in development of the system-level thermal model are summarized below.

1. BoP (not including stack) surface temperatures are lumped and predicted by the average inlet and outlet gas streams of each respective component.
2. Radiation exchange only occurs between each system component and the hot box itself, i.e. no component to component radiation exchange.
3. Each component ‘sees’ the hot box inner wall with a view factor of 1.0.
4. Surfaces are opaque, diffuse, and gray and utilize a linearized radiation heat transfer coefficient.
5. Cavity gas circulation is assumed to be perfectly mixed and the gases are assumed to be transparent in the infrared spectrum.
6. Heat loss associated with conduction from enclosure piping and instrumentation penetrations is neglected.

Using component view factors of 1.0, assumes a relatively large hot box area in comparison to component areas. In the case of larger system components, i.e., the stack and recuperator, where the hot box 'sees' the component, radiation exchange from larger components is expected to be over-predicted. The source of the cavity gas flow is envisioned to be the exhaust from the recuperator. Thus, heat transfer from components near the inlet of cavity gases into the enclosure will experience the greatest error, since that is where the largest departure from the perfectly mixed temperature occurs. Lumped surface temperatures and lack of component-to-component radiation exchange will tend to under-predict the coupling of neighboring system components. Greater fidelity in capturing component-to-component interactions requires either a more elaborate 1-D system model or use of CFD models.

3.4 Model Implementation

The system thermal model was integrated into a thermodynamic system process design model to capture interactions between component heat loss/gain and process gas temperatures and flow conditions. The predictive nature of the resulting integrated model provides feedback to system design parameters such as component sizing and required flow rates. The model is exercised on a 1.1 kW (gross) mobile SOFC system shown in Figure 3.11. The figure illustrates the general layout of the system where each unit operation is a discrete component. The SOFC stack is supported by a dielectric at its corners with a press fit between the stack and the enclosure inner wall. This example SOFC system concept is intended for unmanned underwater vehicle (UUV) applications, but the essential features of the integrated thermal system model are applicable to many other similar-sized applications. The external boundary condition on the hot box can take many forms depending on the UUV configuration. In this study, the enclosure is comprised of an internal metal liner wrapped in insulation and packaged within the vehicle hull. The surrounding environment of the enclosure can vary, but in this UUV application, ocean water represents the surroundings. Assuming conduction resistance through the metal liner and vehicle hull is negligible and the ocean water is opaque, the external boundary condition on the hot box is purely convective. Ambient conditions

surrounding the hotbox are representative of ocean water at a depth of 10 m (P_{amb} = 2.023 bar) and a temperature of 20°C.

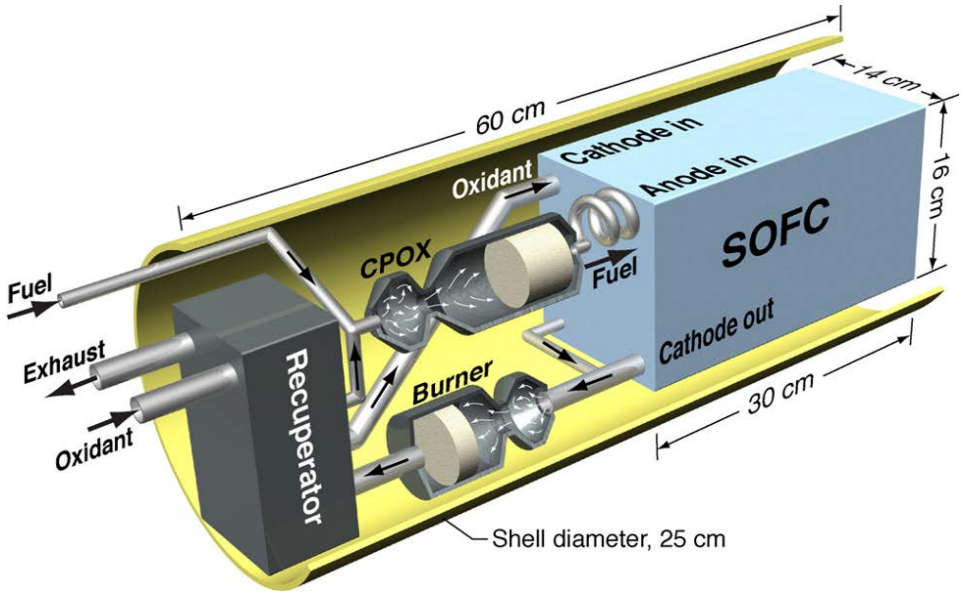

Figure 3.11 Representation of small-scale planar SOFC system with physically separate components

Unlike in the thermodynamic system model, representative geometry is required for the thermal model. The system geometries are listed in Table 3.2. Stack cells are 10x10cm in size and the stack manifolds are 1 cm in width.

Table 3.2 Planar SOFC System Geometry

	Stack Assembly	Stack Module	Recuperator	CPOx	Burner	Enclosure
Height [cm]	28.0	30.0	9.6	N/A	N/A	N/A
Width [cm]	12.0	14.0	7.1	N/A	N/A	N/A
Length [cm]	12.0	16.0	17.2	16.2	10.4	60.0
OD [cm]	N/A	N/A	N/A	4.8	4.1	25.0
Ins. Thick. [mm]	10.0	10.0	10.0	5.0	1.0	10.0
Ins. Material	fb/aerogel	fb/aerogel	aerogel	fb	fb	aerogel

Each component in the thermal model is wrapped in either high temperature Microtherm™ fiberboard or lower temperature Aerogel insulation with empirical fits [30] of the temperature dependence of thermal conductivity given below in Eqs. (3.22) and (3.23) where T is in °C. The SOFC insulation is comprised of a 1st layer of fiberboard and a 2nd layer of aerogel, both of equal thickness.

$$k_{fb} = 2.14E^{-2} + 1.2857E^{-5}T + 2.8571E^{-8}T^2 \tag{3.22}$$

$$k_{aerogel} = 9.7486E^{-3} + 5.7E^{-4}T - 2.1429E^{-8}T^2 \tag{3.23}$$

Baseline convective heat transfer coefficients for the system are listed in Table 3.3. In this system the external heat transfer coefficient for each BoP component, the SOFC stack, and the enclosure inner wall is assumed equal to h_{HB} [W/m^2-K]. A forced and natural convection baseline h_{HB} is used depending on whether gases are circulated inside the enclosure. The natural convection coefficient was calculated using a natural convection relationship for a long horizontal cylinder with the burner geometry. The forced convection heat transfer coefficient is a design/operating parameter because it can be increased above its lower bound by installing a high-temperature circulating fan in the enclosure or injecting recuperator exhaust gas into the enclosure. The lower bound of the convective heat transfer coefficient at the external wall of the enclosure, h_{amb}, is calculated using a free convection relationship for a long horizontal cylinder with the enclosure geometry. The heat transfer coefficient, h_{amb} is also an operating parameter as it increases above the free convection baseline as speed of the UUV through the water increases.

The heat transfer coefficient in the stack manifolds was calculated using a duct flow Nusselt number relationship using the average oxidant mass flow rate in a manifold and a flow area equal to 80% of the flow area in the manifold, which takes into account fuel flow through approximately 20% of the manifold. The average oxidant mass flow rate in a manifold equals 1/2 of the mass flow rate entering the manifold assuming oxidant is equally distributed to all gas channels in the stack.

Table 3.3 Baseline Heat Transfer Coefficients, [W/m^2-K]

$h_{manifold}$	h_{HB}		h_{amb}
	Natural Conv.	Forced Conv.	
29	2	5	16

There are two heat transfers in the SOFC system that are calculated with the thermodynamic system model. Thermodynamically required heat transfer is used to preheat fuel prior to entering the CPOx reformer and remove energy from the CPOx reformate (see Figure 3.12). The relatively low energy input to preheat fuel is taken directly from the heat rejected from the CPOx reformate. The amount of CPOx reformate heat remaining after removing energy for fuel preheat is added to the enclosure resistance model. Physically, the CPOx reformate rejects thermal energy through convection and radiation to the enclosure during pipe flow from the CPOx to the stack anode inlet. Since piping geometry is unknown, the thermodynamically required CPOx reformate heat loss is added to the resistance model. By applying the reformate average gas temperature out of the CPOx and into the stack to a cylindrical pipe geometry, it was determined that 55% of CPOx reformate heat loss is associated with radiation heat transfer and 45% is associated with convection heat transfer. The radiative CPOx reformate gas heat loss is added to the resistance model by adding the following to the $T_{HB,i}$ node.

$$\dot{Q}_{Rad,CPOx\,ref} = 0.55\left(\dot{Q}_{CPOX\,ref\,total}\right) \tag{3.24}$$

The convective CPOx exhaust heat loss is added to the resistance model by adding the following to the $T_{cav\,gas}$ node.

$$\dot{Q}_{Conv,CPOX\,ref} = 0.45\left(\dot{Q}_{CPOX\,ref\,total}\right) \tag{3.25}$$

Surface emissivity values are shown in Table 3.4. Both insulation materials are assumed to have equal emissivity values. Stack manifolds have an emissivity representing a sand-blasted Inconel alloy which lines the manifolds; the small thermal resistance of the metal liner is ignored in the thermal model. Stack and system operating parameters for this study are also listed in Table 3.4.

Table 3.4 System Emissivity Values and Operating Parameters

Emissivity Values		SOFC Stack Parameters				System Parameters	
interconnect	0.80	N_{cells}	45	$T_{Fuel,in}$ [°C]	650	T_{amb} [°C]	20
trilayer	0.80	P [kPa]	228	T_{cell} [°C]	800	P_{amb} [kPa]	202
manifold	0.93	V_{cell} [V]	0.959	U_F	0.85	Oxidant	pure O_2
insulation	0.90	j_{avg} [A/cm^2]	0.258	P_{Gross} [kW]	1.11	Fuel	$C_{12}H_{26}$
		$\Delta T_{cathode}$ [°C]	115			CPOx: O/C	1.0

3.5 RESULTS

Three systems cases (A-C) are explored. The first (Case A) is a thermal system model where recuperator exhaust gases are circulated within the hot box enclosure resulting in forced convection in the enclosure. The second (Case B) is a thermal system model where recuperator exhaust gases are directly plumbed out of the enclosure resulting in natural convection within the enclosure. Finally, thermally coupled system model results are compared against a quasi-adiabatic system model that does not incorporate the system or stack thermal models (Case C).

3.5.1 Case A: Thermally Integrated System Model With Forced Convection

A system statepoint diagram detailing results from an SOFC system operating from liquid dodecane ($C_{12}H_{26}$) and oxygen at the baseline conditions outlined in Table 3.3 and Table 3.4 is shown in Figure 3.12. Of particular interest is the temperature increase between oxidant entering the stack module and that entering the cathode compartment of the stack itself, 58°C. At the operating temperature of the stack, T_{avg} = 800°C, a relatively cold oxidant stream at 652°C is required to enter the oxidant inlet manifold of the stack. The solid stack remains relatively hot at the oxidant inlet, 756°C, which presents a large driving force for heat transfer to manifold cavity gases entering the stack

module. A large driving force does not exist at the oxidant outlet of the stack because the temperature difference between the stack and oxidant flow decreases in the direction of oxidant flow. Oxidant leaving the stack rejects heat to the manifold walls, but the magnitude of the heat rejection is small in comparison to the energy gained by oxidant gases in the stack inlet manifold.

In this system, enclosure cavity gases gain 301 W of thermal energy from the system components within. The amount of heat transfer to cavity gases is among the largest thermal energy transfers occurring in the system. *The high magnitude of heat transfer from system components to the cavity gas implies recuperator exhaust gas circulation has a major effect on system-level operating conditions*.

Of the 235 W of thermal energy leaving the stack insulation, 177 W or 75% is transferred via radiation to the enclosure inner wall. This reveals radiation as a substantial heat transfer mechanism in the hot box; therefore, inclusion of radiation in the system thermal model is essential. Finally, to justify the thermodynamically calculated CPOx exhaust heat loss, it is assumed this flow occurs in a 1.25 cm diameter pipe. A tube length of 10 cm is required to shed the 148 W of required heat which is feasible with coiled piping connecting the CPOx to the anode manifold inlet fitting on the stack.

3.5.2 Case B: Thermally Integrated System Model With Natural Convection

A variation on the physical SOFC system is explored where the recuperator exhaust gas is not forced into the hot enclosure, but is instead convected out of the system through conduit as shown in the statepoint diagram of Figure 3.13. All other parameter (except h_{HB}) from the forced convection case are held constant. Without the relatively cold recuperator exhaust gas entering the hot box cavity and absorbing energy, the hot box inner wall temperature is 144°C higher than with circulating recuperator exhaust gas. A higher hot box wall temperature points to lower system component heat losses which is evident in the stack because a higher oxidant flow rate is required to cool the stack. Stack oxidant flow at 1.986 g/s is 1.65 times higher than the predicted oxidant requirement with circulating recuperator exhaust gas in the enclosure (Case A).

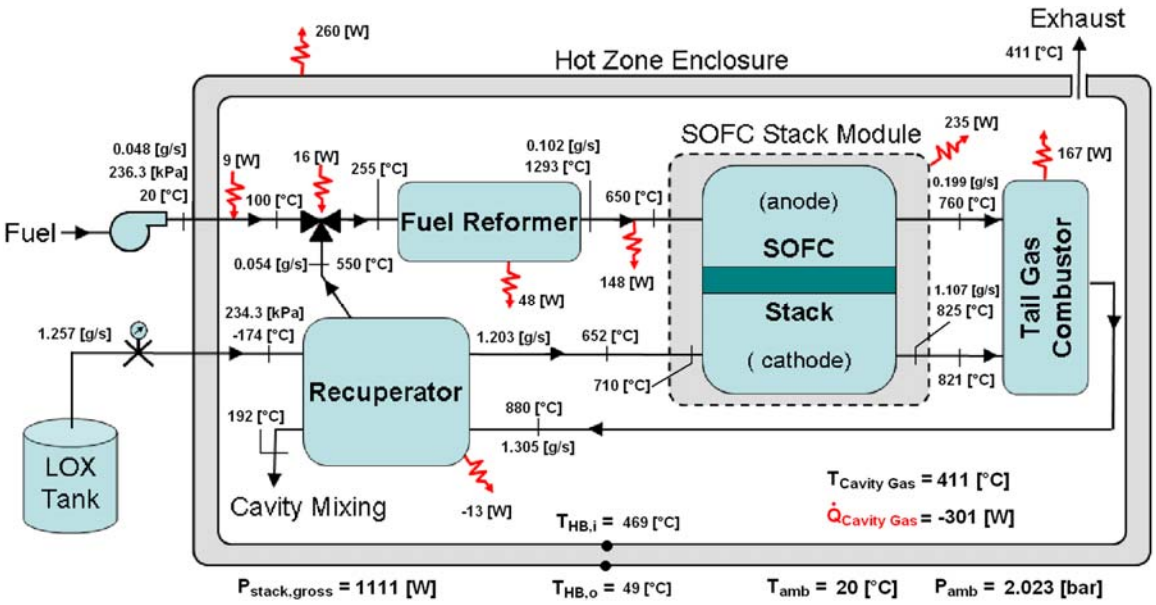

Figure 3.12 Case A: Thermally Integrated SOFC system with recuperator exhaust gas circulation

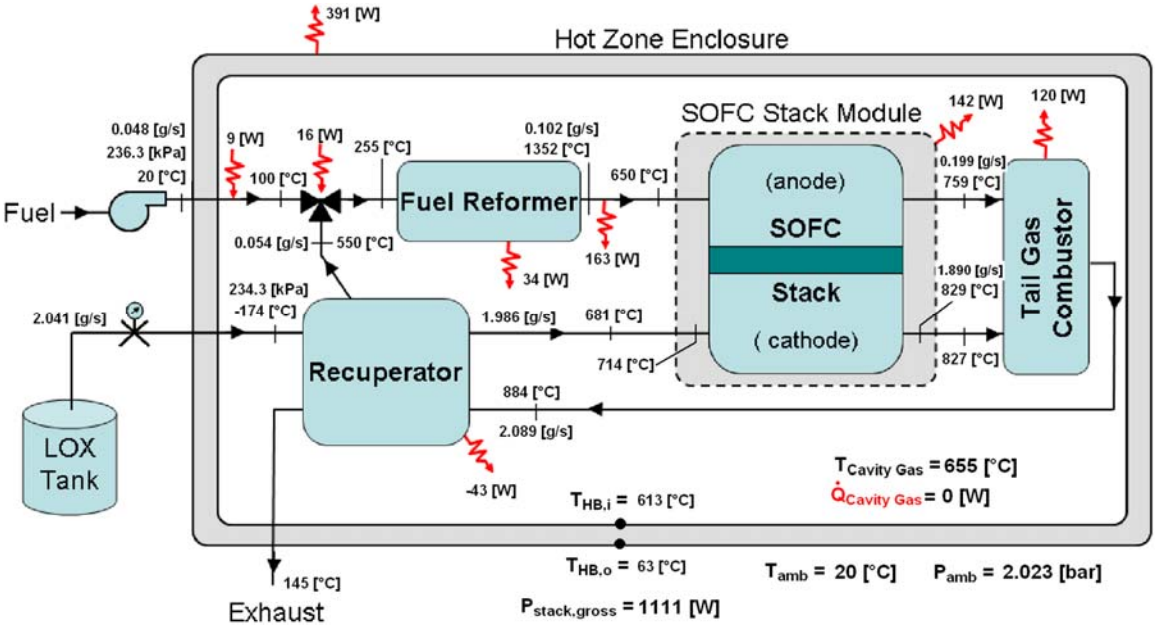

Figure 3.13 Case B: Thermally Integrated SOFC system without recuperator exhaust gas circulation

3.5.3 Case C: Thermodynamic System Model with Quasi-Adiabatic Conditions

To compare the coupling of the thermal model to the thermodynamic system model, an adiabatic thermodynamic system model was run at the same operating conditions used for Figure 3.13. The adiabatic thermodynamic model assumes zero heat transfer from the stack, recuperator, CPOx reformer, and burner. Stack cooling only occurs through convective gas cooling from anode and cathode streams. The two thermodynamically required heat transfers that cool CPOx reformate and preheat fuel are still allowed, with the remaining CPOx reformate heat loss added to recuperator exhaust gases. A statepoint diagram for the adiabatic system model is shown in Figure 3.14. The adiabatic model predicts a required oxidant flow rate of 3.653 g/s which is 1.84 times greater than predicted in Case B and 3.04 times greater than Case A. Oxidant usage becomes extremely important in mobile applications where oxidant must be stored onboard. The sensitivity of oxidant flow rate to system heat transfer predictions provides strong evidence for the need to employ thermally integrated system models.

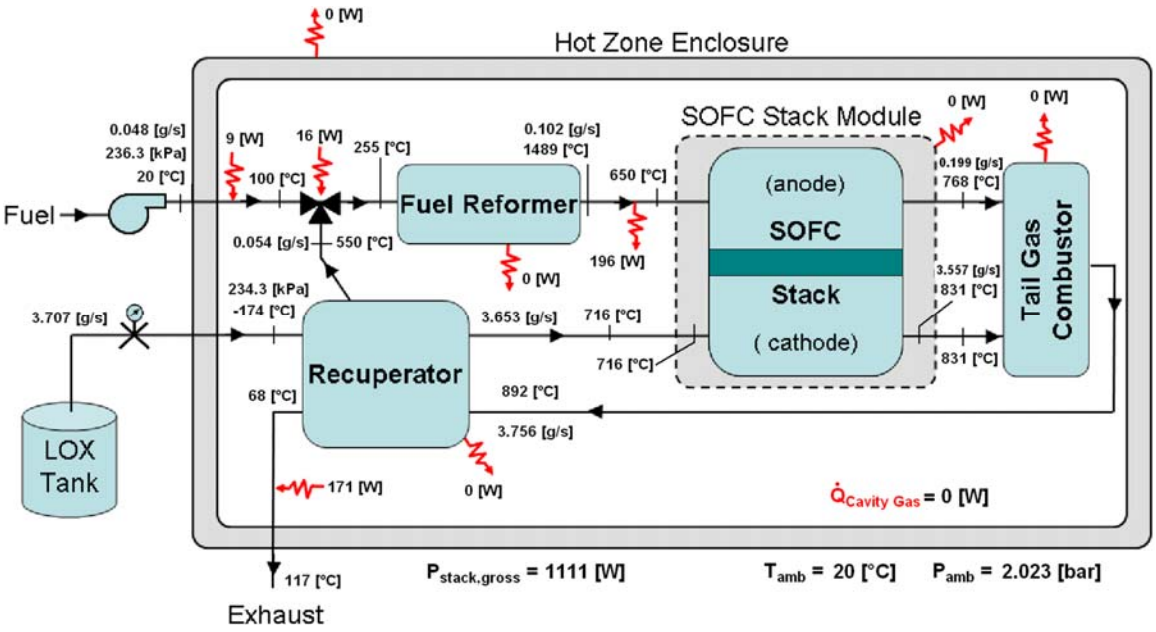

Figure 3.14 Case C: Thermodynamic SOFC system with quasi-adiabatic conditions

3.5.4 Manifold Gas Heating

The temperature rise of oxidant across the stack module varies for all three cases. Temperature increases of 169°C, 146°C, and 115°C in Cases A, B, and C respectively, illustrate the sensitivity of oxidant temperature rise across the stack module to system configuration and thermal model implementation. A significant fraction of oxidant heating occurs in the inlet manifold where 34% and 23% of the overall heating across the stack module occurs in the inlet manifolds of cases A and B, respectively. Oxidant heating within the stack module is also sensitive to the heat transfer coefficient used within the manifolds. A 10% reduction in $h_{manifold}$ in Case A lowers oxidant temperature rise by 5°C across the inlet manifold and across the stack module. As $h_{manifold}$ is dependent on manifold geometry, various stack designs will have different levels of gas heating within the manifolds.

3.5.5 Effect on Cell Temperature Profile

Understanding the impact of thermal management on the temperature distributions within the cell-stack is another important consideration when evaluating system-level thermal interactions associated with SOFC technology. The effect of system configuration (cases A and B) and modeling approach (case C) on the solid trilayer temperature profile within the stack is shown in Figure 3.15. The greatest effect of thermal integration on cell temperature is seen at the oxidant outlet to the stack where the cell temperature is lowered by about 8°C. Moving from the oxidant outlet, cell temperatures are relatively insensitive to the thermal integration method with temperatures remaining within 4°C of one another at cell positions of about 1.5 to 10 cm.

A greater effect on stack design and operation is shown in Figure 3.16 which depicts the effect of coupled heat transfer on the solid trilayer temperature gradient. Stack temperature gradients generate thermally induced stresses. The magnitude and location of the largest gradient in the cell is important in avoiding deleterious operating conditions and designing stacks for maximum operating life.

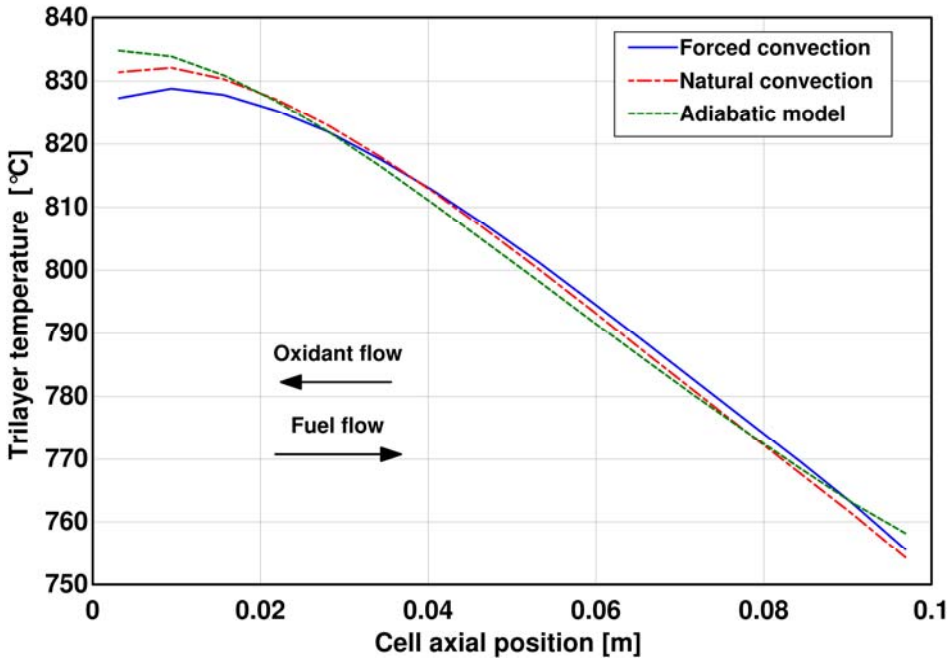

Figure 3.15 Comparison of the solid cell temperature profiles resulting from the three simulation cases.

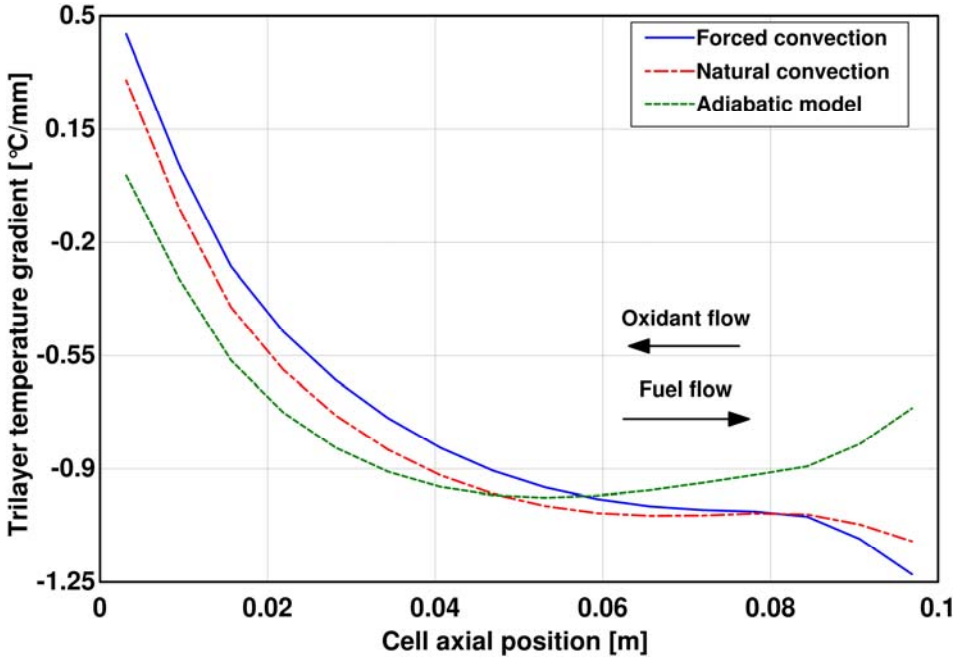

Figure 3.16 Comparison of the solid cell temperature gradient profiles resulting from the three simulation cases.

The overall temperature gradient profile and maximum is altered when the thermal model is integrated. The adiabatic stack has a concave up distribution with a maximum

gradient occurring in the interior of the cell. The thermally integrated stack model shows an inflection point in the temperature gradient profiles with the maximum gradient occurring at the oxidant inlet to the stack rather than within the interior. The maximum cell temperature gradient is predicted to be 24% higher with a thermally integrated stack (Case A) compared to an adiabatic stack model (Case C).

3.5.6 Parametric Study on Case A: Thermally Integrated SOFC Model with Forced Convection

Now focus is shifted to the circulating recuperator exhaust gas system integrated with the thermal system model. The sensitivity of the SOFC system to the design/operating parameters, h_{HB} and h_{amb} is explored in the following. First, the sensitivity to the convective heat transfer coefficient in the enclosure cavity, h_{HB}, is explored as h_{HB} can be varied by installing an induced draft fan in the system outlet duct. The total thermal resistance to the system surrounding of each BoP component as defined in Eq. (3.16) along with the total resistance of the stack surfaces is plotted against h_{HB} in Figure 3.17.

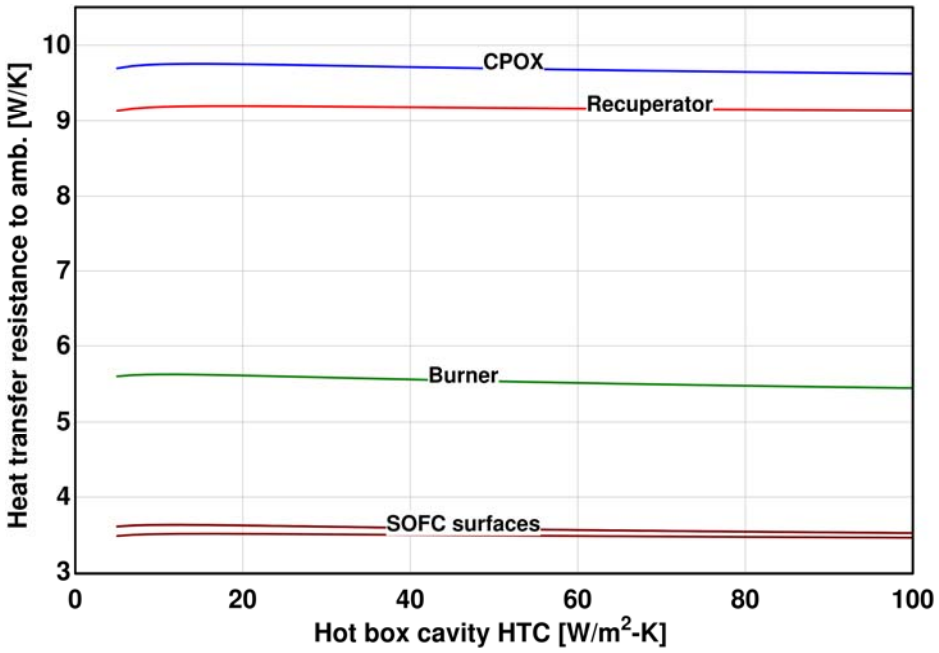

Figure 3.17 The effect of varying the heat transfer coefficient inside the enclosure on total heat transfer resistances of system components

Interestingly, total resistance increases slightly as h_{HB} increases from 2 to around 18 W/m^2-K. Further increases in h_{HB} result in only slight decreases in the thermal resistance of the BoP components. The increase in resistance is due to the competition between radiation and convection heat transfer in the hot box. Increases in h_{HB} act to decrease component surface temperatures and increase radiation heat transfer resistance. The balance between radiation and convection heat transfer mechanisms in the hot box is illustrated in Figure 3.18 using the burner. Radiation heat transfer accounts for >50% of total burner heat transfer for h_{HB} < 87 W/m^2-K.

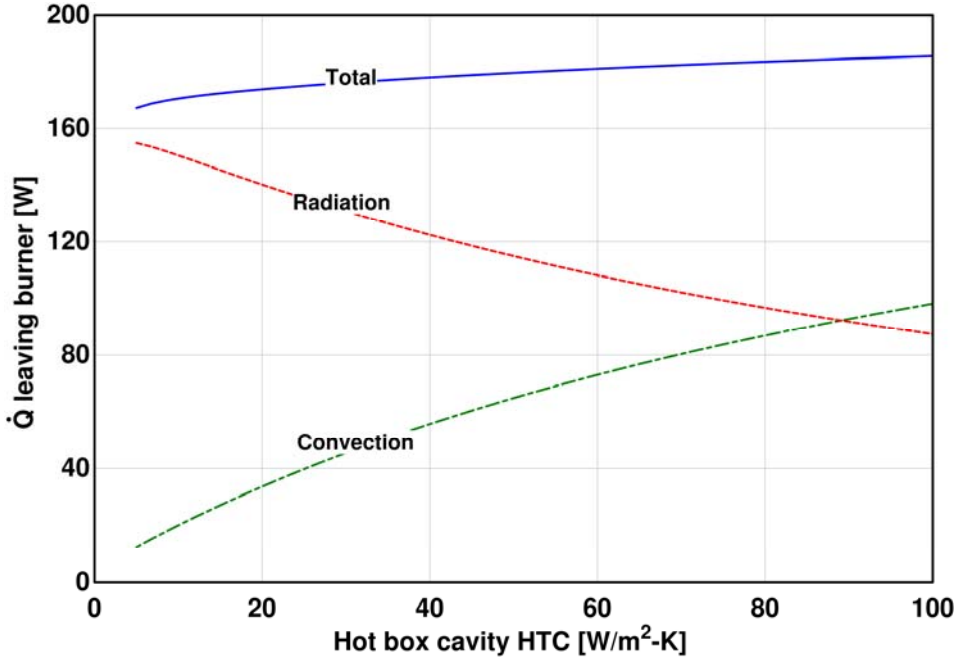

Figure 3.18 The effect of varying the heat transfer coefficient inside the system enclosure on heat transfer pathways of the burner

Total thermal resistances show little sensitivity to h_{HB}, but shown in Figure 3.19 is the effect of h_{HB} on heat transferred to the recuperator exhaust cavity gases. At the lower bound, a slight increase in h_{HB} substantially increases the component heat rejection to circulating cavity gases. The large increase in heat transfer to the gas flow in the enclosure is the main reason for lower system temperatures and therefore a higher radiation resistance. Although total resistances increase, component level heat losses increase through out the range of h_{HB}, also shown in Figure 3.19. The greatest increase in

heat loss occurs in the lower h_{HB} range where heat transfer to cavity gases increases rapidly which provides a large sink of thermal energy for system components.

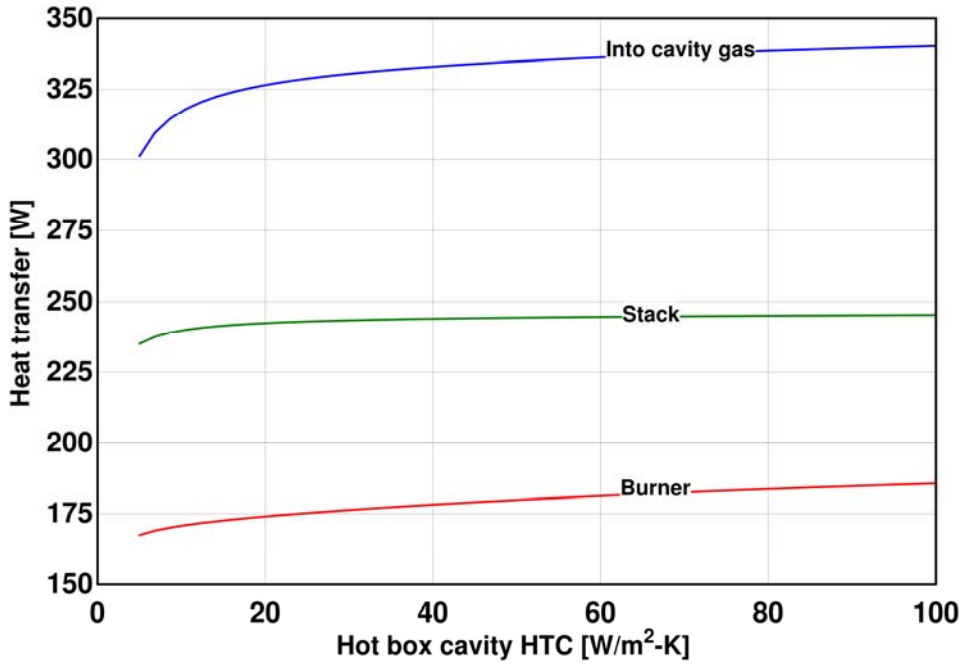

Figure 3.19 The effect of varying the heat transfer coefficient inside the system enclosure on total heat transfer within the system

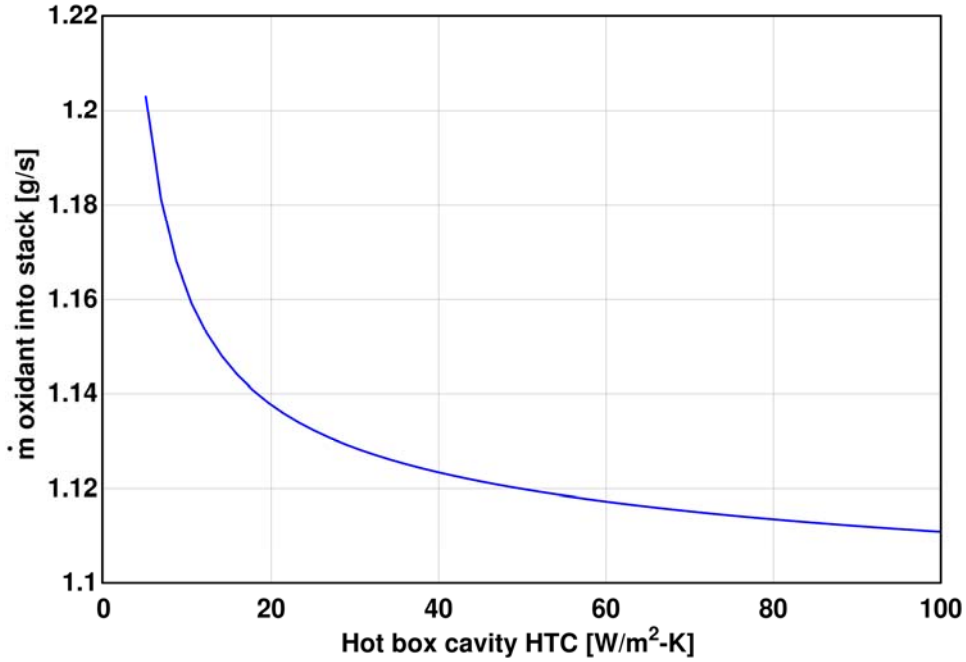

Figure 3.20 The required oxidant flowrate to the stack as a function of heat transfer coefficient inside the system enclosure

As seen earlier, oxidant flow rate is highly sensitive to the implementation of the thermal model. The sensitivity of oxidant flow rate to h_{HB} is explored in Figure 3.20. Oxidant flow rate shows a strong non-linear relationship to the enclosure heat transfer coefficient below about 40 W/m^2-K. The required oxidant flow into the stack decreases by nearly 7% as h_{HB} increases from 5 to 40 W/m^2-K. As h_{HB} increases the stack has a decreased need for convective cathode gas cooling as a greater fraction of thermal energy is being transferred from the stack surfaces to the enclosure and cavity gas.

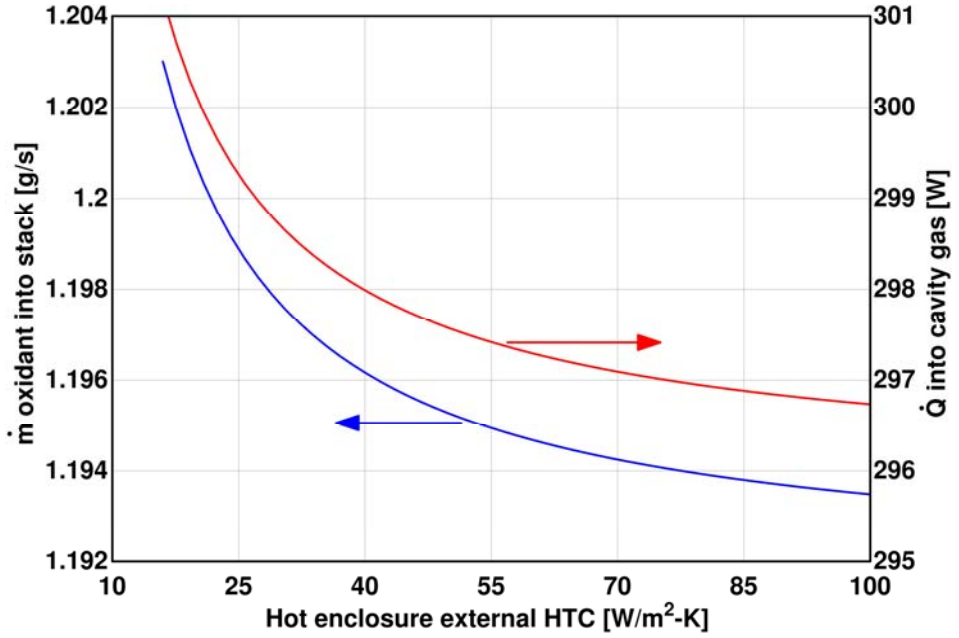

Figure 3.21 The effects of varying the heat transfer coefficient external to the enclosure on oxidant flowrate and heat transfer within the system

Variation of the heat transfer coefficient on the outer surface of the enclosure, h_{amb}, is also explored. In the UUV application h_{amb} is a function of the UUV speed. Figure 3.21 illustrates that oxidant gas flow is less sensitive to h_{amb} than h_{HB}. The large surface area of the enclosure compared to system components leads to a relatively small thermal resistance at the enclosure external boundary; therefore, a further decrease of external resistance with increasing h_{amb} has marginal effect on the total resistance from system components. Unlike the large increase in heat absorbed by cavity gases with increasing h_{HB}, heat absorbed by cavity gases decreases slightly with increasing h_{amb}. Cavity gas heating is a major thermal energy sink for stack components and without a substantial

change of energy into the cavity gas, component heat loss remains relatively constant over the range of h_{amb}. With component heat losses relatively constant, the amount of cathode gas convective cooling in the stack remains relatively constant which explains the low sensitivity of oxidant flow in the stack to h_{amb}.

3.6 Summary of Findings

A system-level thermal model has been developed to add fidelity to existing thermodynamic SOFC system models. The thermal model of the SOFC system includes a reformer, burner, recuperator, and SOFC stack, which are contained within a hot enclosure. Thermal interactions between discrete system components are captured by incorporating a system-level thermal resistance network coupling component heat transfer to both the system-enclosure inner wall and the cavity gas within the enclosure.

In this study, the thermal model was integrated with a thermodynamic system model which included a previously developed 1-D planar stack model. The 1.1 kW SOFC system under study was adapted from design concepts intended for UUV applications. Model predictions of system heat loss aid in system-level design and operating parameter selection. As shown in this study, if a conventional adiabatic thermodynamic model (Case C) is used in system design, the required stack oxidant flow rate is over-predicted by 84% requiring a 90% larger recuperator heat duty compared to the thermally integrated system model (Case B).

It was further shown that circulating recuperator exhaust gas in the hot box enclosure (Case A) decreases stack oxidant usage by 39% compared to directly purging recuperator exhaust from the system (Case B). A 41% reduction in recuperator heat transfer duty accompanies modifying the system to allow for circulating recuperator exhaust gases. Compared against Case A, adiabatic modeling results over-predict oxidant flow rate by 204% and recuperator heat duty by 221%. With circulating recuperator exhaust (Case A), stack oxidant requirements and recuperator heat transfer duty drop an additional 7% by increasing the convective heat transfer coefficient in the enclosure from

5 - 40 W/m^2-K which could be accomplished with the use of a circulating fan or other means. Model predictions point to the significance of enclosure gas circulation in sizing system components and oxidant flow rates. External thermal boundary conditions are observed to have little effect on overall system operating conditions due to the large enclosure surface area in comparison to system component areas.

Beyond UUV applications, cool ambient air could be circulated through the hot box enclosure rather than recuperator exhaust. Circulating ambient air could provide a larger thermal sink and consequently lower oxidant flows through the stack. Trade-offs between the increased blower power required to deliver sufficient circulating flow and the decrease in blower power required to deliver oxidant to the stack will need to be considered. Additionally, ambient air temperatures remain relatively constant allowing for simplified control algorithms in comparison to circulating recuperator exhaust as its temperature will vary with changes in operating conditions.

Alterations in both the profile of the cell temperature gradient and the maximum value of the gradient itself were observed with the thermal management model. Thermally integrated models predict maximum thermally induced cell stress to occur at the oxidant inlet rather than within the interior of the cell-stack as predicted with adiabatic system models. Temperature gradients from the thermally integrated model (Case A) were estimated to be about 24% higher than the adiabatic model (Case C). Stack temperature gradients are also influenced by the extent of oxidant heating occurring within stack manifolds. An accurate prediction of oxidant heating within the manifolds requires an accurate convective heat transfer coefficient which is highly dependent on the manifold geometry. In this study, a simplified manifold geometry was used utilizing a rectangular duct flow relationship to calculate a convective heat transfer coefficient.

The development of a low-dimensional thermal modeling tool can be quite effective in revealing important interactions between the components and their surroundings, as well as the impact on process gas temperatures and flow requirements within the system. While the implementation of thermal management modeling with system-level design

tools enables a better understanding of the coupled component heat transport phenomena within high temperature planar SOFC systems, it is acknowledged that this tool must be experimentally validated. Nevertheless, in lieu of such validation, the utility of the thermal model developed herein is that substantial design and performance insights are gained without the expense, complexity, and overhead of models that employ simulations based on three-dimensional computational fluid dynamics software.

CHAPTER 4

HIGHLY-INTEGRATED TUBULAR SOFC SYSTEM MODEL

Portable power is emerging as a promising market for SOFCs. SOFCs are predicted to have higher energy densities than batteries for applications that require long operational times or mission durations. System design and packaging have a large impact on the power density achieved by SOFCs. Traditionally, SOFC developers have focused on increasing the packing efficiency of discrete SOFC systems such as that discussed in Chapter 3. The physical spacing between components in discrete systems limits their overall system power density. A novel approach in system design is to create a highly-integrated SOFC system where the BoP and stack are no longer discrete components. In a highly-integrated system, components share common walls and distinct flow piping is no longer required. The thermal coupling between system components also becomes enhanced as components are in intimate contact with one another. Highly-integrated systems are posed to benefit from increased power densities, but this is only realized with system architectures that effectively thermally couple system-level sinks and sources.

4.1 Objectives

The objectives of the work related to tubular SOFC geometries are to (i) create a high-fidelity cell-stack model able to predict performance variations amongst cells, (ii) create a thermally coupled system model around the high-fidelity cell-stack to capture the thermal and fluidic coupling throughout the system, (iii) use simulation results to suggest improved system designs, (iv) and provide cell performance groupings to increase the accuracy of reduced-order models. The SOFC system model includes a tubular SOFC stack, CPOx fuel reformer, TGC, recuperator, and all process flow conduits. In this

chapter, the overall modeling approach and system geometry under study is first presented. Next details on the CFD computational domain, user-defined function, individual component models, and information exchange between models is given. The capabilities of the model are then explored by simulating a highly-integrated tubular SOFC system with an output range of 500-1000 W.

4.2 Modeling Approach

The level of model fidelity applied varies throughout the system model. Electrochemistry, anode fluid dynamics, and heat transfer within the cells is captured through a previously developed 1-D electrochemical tubular SOFC model [31]. Unlike planar stacks where relatively uniform anode and cathode gas flows exist in small length scale flow channels, tubular stacks posses a relatively large flow area external to the cells where spatial flow variations occur. The tube bundle geometry under investigation is shown in Figure 4.1, where the anode gas is internal (tube-side) to and cathode gas flow is external (shell-side) to the cells. Large cathode flow area leads to spatial variations in fluid flow, temperature, and oxidant concentration. The need to accurately capture spatial property variations within the cathode due to thermofluidic interactions is the main motivation for incorporating a CFD model of the cathode gas volume as shown in Figure 4.1.

Each tubular cell in the stack is modeled with a 1-D electrochemical tube model that is coupled to the 3-D CFD flow field. Modeling of the SOFC stack alone is not sufficient for stack design considerations because of the tight performance coupling between BoP and tube bundle. Feedback between BoP components and the stack is required. Coupling BoP models to the stack model provides the needed feedback for a realistic system modeling tool. The CFD computational domain includes the cathode (shell-side) gas flow, a tail-gas recuperator, the CPOx fuel/air preheat tube region, stack endplates, and system insulation. The CPOx and TGC components and their surrounding geometries are modeled with quasi-one dimensional thermal resistance models that are coupled to both the CFD and tube models. All models are interconnected through

passing of thermodynamic states and heat transfer rates at intersecting model boundaries (see Figure 4.2). Details on system geometry are given in Section 4.3 followed by the details of each component model and its coupling to create the system modeling tool, Sections 4.4 - 4.7.

4.3 System Model Geometry

The system design under investigation is derived from a patent application by an SOFC developer for a portable power system delivering up to 125 W [32]. The patented stack is of tubular geometry with 36-tubes arranged in a hexagonal grid. The system, depicted in the simplified diagram of Figure 4.2, can be generalized as a centrally located stack surrounded by larger cylindrical cans creating annular process flow channels. The entire system is wrapped in insulation and operates as described below.

First, oxidant for the cathode enters the system through four inlet tubes at the top of the insulation. Oxidant is then preheated in a three-fluid (oxidant, cathode gases, TGC exhaust) annular recuperative heat exchanger. Leaving the recuperator, oxidant turns radially inward entering the cathode. Oxidant leaves the cathode through concentric circle cut-outs surrounding each tube in the outlet tube-sheet. Fuel entering the system is first sent through an atomizing spray nozzle mixing with air at the outside edge of the insulation. The fuel/air mixture is preheated as it flows down a centrally located tube before entering the CPOx reformer. Leaving the reformer, reformate is distributed inside a fuel plenum located directly beneath the inlet tube-sheet. Reformate enters the anode gas channels and flows up toward the outlet tube-sheet. Anode and oxidant gases leaving the stack mix directly above the outlet tube-sheet and enter the TGC. TGC exhaust gas flows radially outward, turns 90°, and flows down an annular channel in the recuperator. Exhaust gas leaves the recuperator and is funneled radially inward and expelled from the system through conduits at the bottom of the insulation.

In order to simulate a system of more applicable power capacity, the 36-tube patent application design was scaled to a system with a nominal power output of 650 W. The

scaled 650 W system began with a 66-tube bundle geometry provided by the developer. The cells are arranged in a hexagonal grid that is symmetric about the *x*- and *y*-axes as shown in Figure 4.1. In the symmetric tube bundle, there are 19 distinct tubes as labeled in Figure 4.1. BoP components including the recuperator, CPOx, and TGC are scaled from the 36-tube system to fit around the larger 66-tube stack. Scaling the recuperator gas channels began by attempting to maintain a constant Reynolds number between the 36 and 66-tube systems. Equating Reynolds numbers simplifies to Eq. (4.1) as density and viscosity are constant between the two systems. Examining the air channel of the recuperator, the inner radius is set by the outer radius of the 66-tube bundle leading to a larger hydraulic diameter, D_h, than in the smaller 36-tube system. The 66-tube system also operates with approximately nine times more airflow (i.e. increased velocity, U) which requires a very large channel to maintain a constant *Re #.*

$$\frac{\mathrm{Re}_{66}}{\mathrm{Re}_{36}} = \frac{D_h U\big|_{66\ \mathrm{tubes}}}{D_h U\big|_{36\ \mathrm{tubes}}} = 1 \tag{4.1}$$

As an alternative scaling method, the gas channel widths within the recuperator, CPOx, and TGC of the 66-tube system are set equal to the channel widths in the 36-tube system. The result is a nominal 650 W system centered around a 66-tube stack with a system architecture equivalent to the 36-tube system, Figure 4.2.

Details of reactor sizing in the CPOx and TGC along with the tubular cell length, diameter, and thickness were extracted from information provided by the developer. The resulting system dimensions are shown in Table 4.1. Inlet flow conditions to the nominal 650 W system were also supplied by the developer.

Table 4.1 System and Tubular Cell Dimensions, units in [cm]

	CFD	CPOX	TGC	System	SOFC Cells
Height	12.8	6.3	5.8	24.9	12.5 (active)
OD	22.6	22.6	21.6	22.3	1.1
Ins. Thickness	3.0	2.4	3.2	2.9	--

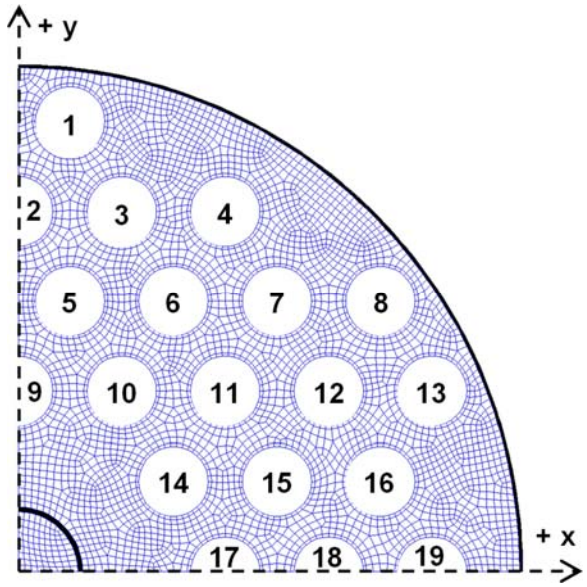

Figure 4.1 66-tube bundle shown in ¼ symmetry. The CFD grid, shown in blue, surrounds the domain of the tube model. Each cell is modeled independently with the tube model. Central tube is for fuel/air preheating.

4.4 Computational Fluid Dynamics Model

The CFD software platform employed in the model development was ANSYS® FLUENT®. It is also the FLUENT software that executes a User Defined Function (UDF) which integrates all component models. In the subsequent sections, the FLUENT domain, settings, and the UDF are discussed.

4.4.1 Domain

The domain of the CFD model is illustrated in Figure 4.2 which includes the entire cathode and stack endplates along with the majority of the recuperator, fuel/air preheat flow, and system insulation. The outer diameter (cathode surface) of every tubular cell represents the boundary between the CFD and tube model. FLUENT solves the mass, energy, momentum, and species conservation equations within the computational domain of the CFD model. Owing to the stack symmetry (see Figure 4.1), one-quarter of the system is modeled with symmetry boundary conditions applied at the *x*- and *y*-axes.

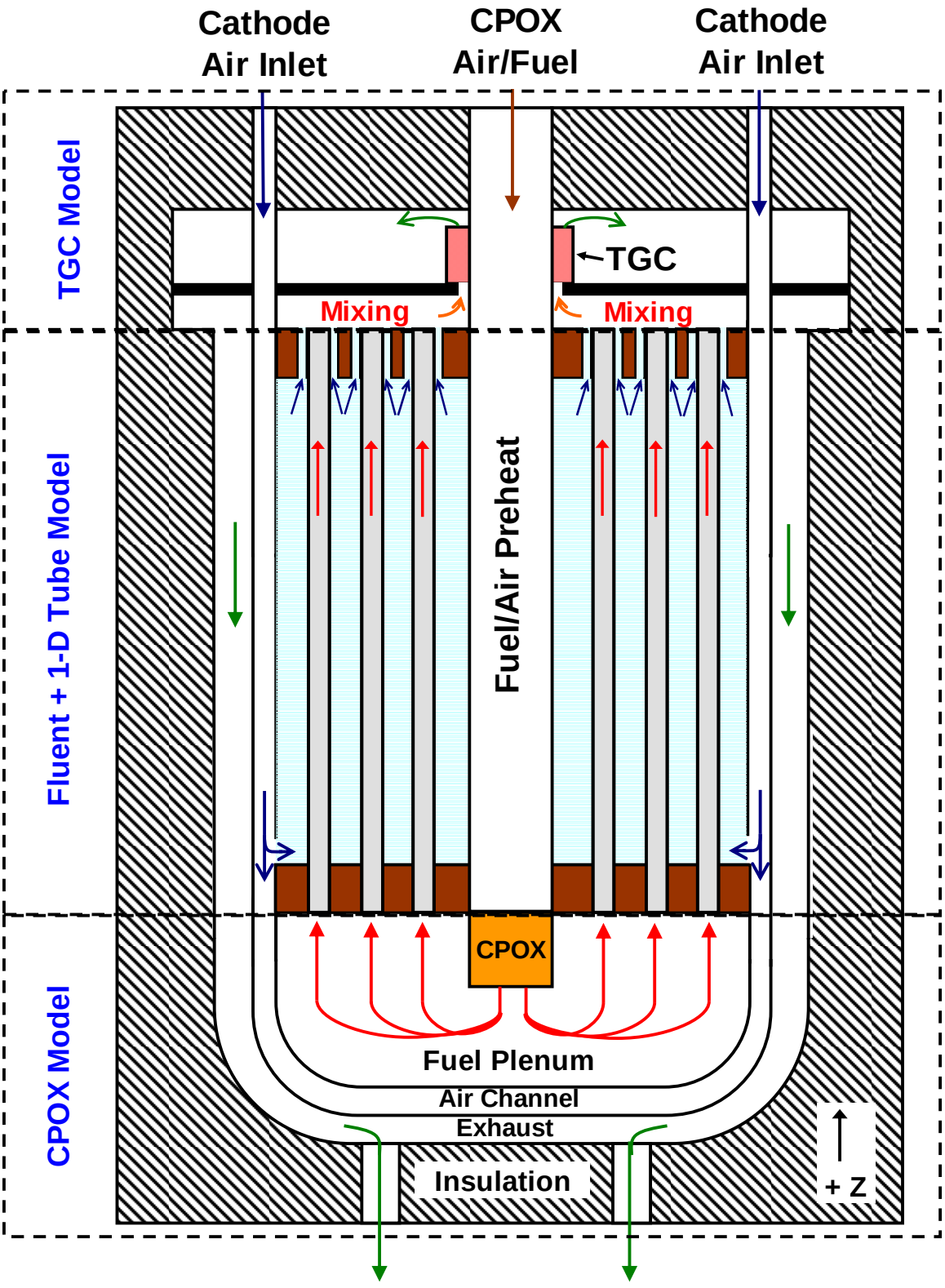

Figure 4.2 System model geometry. Dashed lines indicate domain of component models.

4.4.2 CFD Model Settings

Solid conduction, convection, and radiation heat transfer mechanisms are modeled throughout the CFD domain. It is assumed all gas species are transparent and non-participating. While surface-to-surface radiation modeling is most appropriate, surface-to-surface is unavailable in FLUENT with symmetry boundary conditions; therefore, the discrete ordinates radiation method is used. With all fluids set as transparent, discrete ordinates acts as a surface-to-surface radiation model. To check the validity of the discrete ordinates method, a complete 66-tube CFD model with surface-to-surface radiation was simulated. A comparison of numeric results between surface-to-surface and discrete ordinates methods found excellent agreement.

Diffusion occurs within the CFD domain as oxygen is reduced at the cathode electrode surface (outer diameter of cells). The flux of O_2 diffusion to the cathode surface is predicted with the 1-D tube model. Diffusion from the bulk cathode gas is modeled using Fickian diffusion utilizing temperature dependent binary diffusion coefficients, D_{ij}. Since the cathode is a two species mixture, $D_{O2,m} = D_{O2,N2}$ and $D_{O2,N2} = D_{N2,O2}$ where m is the mixture. The temperature dependent polynomial fit to the binary diffusion coefficient, $D_{O2,N2}$, was calculated with Cantera [33].

$$D_{O2,N2} = 1.095x10^{-10} \cdot T^2 + 7.993x10^{-8} \cdot T - 1.1559x10^{-5} \tag{4.2}$$

where T is in Kelvin.

A laminar flow solver is used throughout the CFD domain which is appropriate because the largest Reynolds number in the flow field is estimated at approximately 1200.

Piecewise-linear temperature dependencies of density, specific heat, thermal conductivity, and viscosity are used for each gas species. Thermal conductivity and viscosity use a mass weighted mixing law while the density is calculated using the incompressible ideal gas law.

Solid materials used within the CFD domain include a metal, insulation, and the SOFC tube material. Metal components include the inlet and outlet tube-sheets, stack can wall, fuel/air preheat tube, and the recuperator wall separating air and exhaust flows. All metals are modeled as INCONEL® 600 alloy with thermal conductivity applied as a piece-wise linear function extracted from manufacturer data [34]. Thermal conductivity values range from 17.3 to 27.5 W/m-K in the temperature range of interest. An emissivity of 0.9 is applied to all metal surfaces.

The insulation around the system is modeled as Microtherm™ fiberboard with a thermal conductivity applied as a 2nd order polynomial fit of manufacturer data, as shown below [30]. An emissivity of 0.9 is assigned to all insulation surfaces.

$$k_{fb} = 2.857x10^{-8} \cdot T^2 - 2.743x10^{-6} \cdot T + 2.002x10^{-2} \tag{4.3}$$

A common thermal conductivity, 10.5 W/m-K, is applied to the tube solid in the CFD model and 1-D tube model. A precise emissivity of SOFC cathodes is uncertain; therefore, an emissivity value consistent with the literature is used, ε_{tube} = 0.8 [8,35,36].

4.4.3 User Defined Function (UDF)

A UDF written in C employing FLUENT built-in functions is used to thermally integrate the CFD model to the remaining SOFC system. All CFD boundaries except the outer insulation surface represent interfaces with either the 1-D tube model, the CPOx model, or the TGC model. The outer diameter of every tubular cell represents the boundary between the CFD model and the 1-D tube model. The top and bottom of the CFD domain represent the boundaries between the TGC and CPOX models, respectively. It is the UDF that provides the communication pathways between FLUENT and the component models. A schematic of the required system model connections is shown in Figure 4.3.

The UDF is called within FLUENT at the start of every FLUENT iteration and thermally couples all components at their common boundaries. Passing of information from one

model to another at their intersections occurs via the writing and reading of data files. As an example, the thermodynamic state of fuel/air leaving the CFD domain is extracted with the UDF and written to a data file which the CPOx model reads as the inlet to the CPOx reformer. While the UDF relays boundary conditions to the CFD model every FLUENT iteration, executing the 1-D tube model, CPOx model, and TGC model occurs every N FLUENT iterations to update these boundary conditions. The current modeling strategy is to set $N = 5$, but this is an input parameter that could be optimized to reduce computational time.

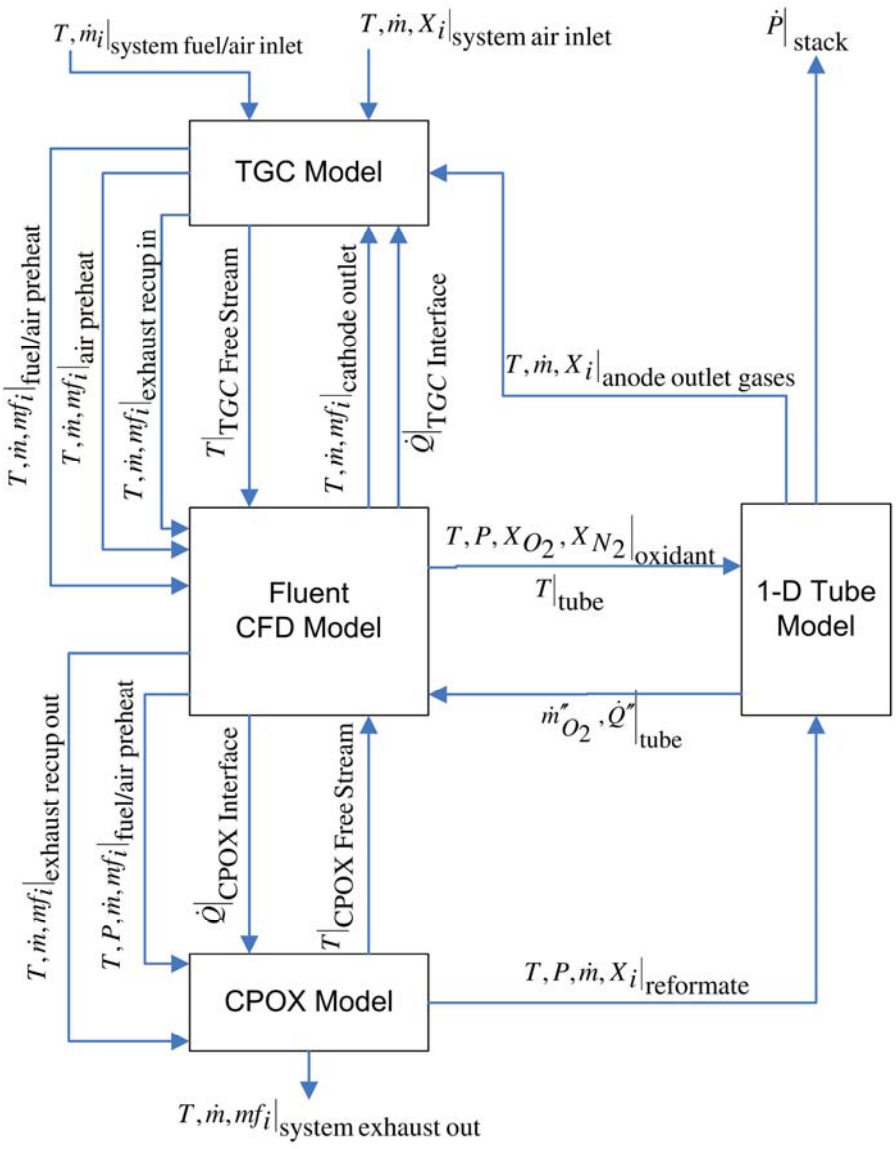

Figure 4.3 Communication pathways required between all component models. Passing of information conducted by UDF.

4.5 1-D Electrochemical Tubular Cell Model

A previously developed 1-D anode-supported tube model is employed to model the electrochemically active cell regions [31]. The model incorporates electrochemistry, anode gas flow, and heat transfer within the anode flow channel and solid MEA. Radiation heat transfer is assumed negligible within the fuel channels (interior to the cell). Gas diffusion within the porous anode is modeled using the Dusty Gas Model. Electrochemical performance is based on the Nernst equation with cathode and anode activation losses, concentration losses, and ohmic losses. Axial conduction is assumed to occur within the relatively thick anode structure only.

Each tube extends from the bottom of the inlet tube-sheet to the top of the outlet tube-sheet. Electrochemically active cell area is defined by the tube area between the tube-sheets. More specifically, the tubes are electrochemically inactive within the space where the tubes protrude into the tube-sheet because tubes are being supported by the tube-sheet. In the case of the inlet tube-sheet, no oxidant reaches the cathode surface and because ion conduction is primarily normal to the tube (not axial) the surface is assumed inactive. In contrast, tubes are assumed electrochemically inactive within the *outlet* tube-sheet even though oxidant flow reaches the cathode surface. This is a valid assumption because the 3.2 mm thickness of the tube-sheets is small in comparison to the 125 mm active tube length. Modeling of the entire bundle is accomplished by simulating every tube in the bundle with the 1-D tube model.

4.6 Coupling 3-D CFD Domain to 1-D Tube Model

The approach to couple the 3-D CFD cathode to the 1-D tube model is discussed in the following. The coupling process is carried out within the UDF.

4.6.1 Mapping 3-D Mesh to 1-D Bands

In all cases considered, the CFD computational grid of the cathode at the tube boundaries is finer than the 1-D band discretization used within the tube model as

illustrated in Figure 4.4. The first step in the mapping process is to number each 1-D tube band in order of increasing axial location. A common band grid is used on every tube within the bundle. Next, the axial locations of the 1-D band edges are calculated (red lines in Figure 4.4). Then, a loop begins over all FLUENT control volumes that border a tube wall (black lines in Figure 4.4). In this loop, the centroid of the control volume is first calculated. The control volume is then mapped to the tube band whose edges bound its centroid in the axial direction. This procedure results in a mapping between all CFD control volumes bordering the tube walls and the bands of the tube model. This mapping is used to pass information between the CFD and tube model.

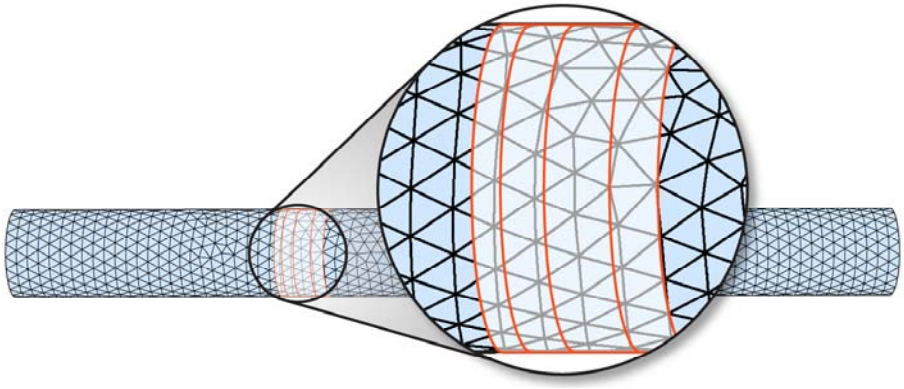

Figure 4.4 Fluent discretization, black lines, at SOFC tube interface overlaid on 1-D tube model bands, red lines

4.6.2 Variable Passing

As shown in Figure 4.3 the UDF passes the variables required for a complete coupling of mass and energy between the CFD and 1-D tube model. FLUENT provides the thermodynamic state of oxidant in the control volumes adjacent to the tube wall boundary as well as the temperature at the tube surface to the tube model. The tube model provides the resulting heat and oxygen flux occurring at the tube surface.

All flow variables extracted from FLUENT are first area averaged amongst all control volumes within their assigned axial band, thus creating area-averaged 1-D profiles that the tube model can interpret. Every FLUENT-passed variable is then sent to the tube model *except for the tube temperature profile*.

4.6.3 Tube Temperature Smoothing

Area-averaged tube temperatures are further manipulated before being applied in the tube model. Due to area averaging, the first derivative of tube temperature is not smooth, that is, step changes in axial conduction result if the area-averaged tube temperature is applied directly in the tube model. Tube axial conduction is smoothed by fitting an n^{th} order polynomial to the area-averaged tube temperature data. An axial tube temperature profile extracted from the n^{th} order polynomial fit is applied to the tube model.

4.6.4 Interpolating 1-D Tube Variables in CFD Model

All tube model variables passed to Fluent are applied using linear interpolation. For example, the heat flux applied to a particular Fluent control volume is determined with the linear interpolation scheme illustrated in Figure 4.5 given by Eqs. 4.4 and 4.5.

$$\frac{z_c - z_1}{z_2 - z_1} = \frac{Q_c'' - Q_1''}{Q_2'' - Q_1''} \tag{4.4}$$

$$Q_c'' = \frac{z_c - z_1}{z_2 - z_1} \cdot \left(Q_2'' - Q_1''\right) + Q_1'' \tag{4.5}$$

where z_1, z_2 are the axial locations of the tube model band centers. z_c is the axial location of the centroid located on the tube wall face of Fluent control volume c. Q_1'' and Q_2'' are the heat fluxes calculated via the tube model and Q_c'' is the heat flux applied to control volume *c* within the CFD model.

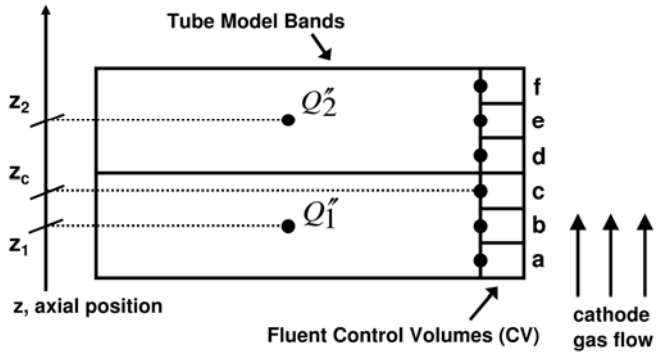

Figure 4.5 Linear interpolation of variable passing from 1-D tube model to 3-D Fluent model

4.6.5 Boundary Conditions in CFD Model

The tube surface heat flux is applied directly as a heat flux thermal boundary condition at each tube wall in the CFD model. Oxygen flux is applied as a sink of mass and energy to each control volume that borders the tube walls, where each sink is calculated as follows.

$$Mass\ Source = \frac{j''_{O_2,face} \cdot A_{face}}{V_{CV}} \left[=\right] kg/m^3 \cdot s^1 \tag{4.6}$$

$$Energy\ Source = \frac{j''_{O_2,face} \cdot A_{face} \cdot h_{O_2,face}}{V_{CV}} \left[=\right] W/m^3 \tag{4.7}$$

$$h_{O_2,face} = \int_{T_{ref}}^{T_{CV}} Cp_{O_2}\, dT \tag{4.8}$$

$$\overline{C}p_{O_2} = 25.48 + \left(1.520E^{-2}\right)T - \left(0.7155E^{-5}\right)T^2 + \left(1.312E^{-9}\right)T^3 \tag{4.9}$$

$$Cp_{O_2} = \frac{\overline{C}p_{O_2}}{MW_{O_2}} \tag{4.10}$$

where $j''_{O_2,face}$ is the interpolated oxygen flux rate applied at a control volume bordering the tube wall boundary, A_{face} is the area of the tube wall face of said control volume. V_{CV} is the volume and T_{CV} is the gas temperature of said control volume. T_{ref} is the enthalpy reference temperature in FLUENT, 298.15 K. $h_{O2,face}$ is the enthalpy of oxygen in said control volume, Cp_{O2} is the mass-based specific heat and MW_{O2} is the molar mass of oxygen.

4.6.6 Electrochemically Inactive Tube Ends

The electrochemically inactive tube ends within the tube-sheets are discretized and incorporated within the CFD domain. The conductive heat flux at the inlet and outlet of the electrochemically active tube length, calculated with the tube model, is applied as a heat flux boundary condition within FLUENT at the interface between the active and

inactive tube sections. Anode gas flow in the non-reactive ends is not discretized in FLUENT and modeled within the CPOx and TGC models.

4.7 Modeling of Fuel Gas Processing

Reforming of the liquid hydrocarbon fuel feed to the system occurs within the small CPOx unit that is integrated within the stack. Depleted anode fuel gases are completely oxidized in the tail-gas combustor which is located at the end of the tube bundle opposite of the CPOx unit. The TGC and CPOx devices (see Figure 4.2) are modeled individually. Thermal effects within each model are captured with a quasi 1-D thermal resistance model. Lumped surface temperatures are assumed within the thermal resistance model where lumped surface definitions are shown in Figure 4.6. The CPOx and TGC models share common boundaries with the CFD and tube model. At these model interfaces, the UDF extracts and exchanges the thermodynamic state, thus coupling the CPOx and TGC models to the SOFC system model (see Figure 4.3). For example, the state of preheated fuel/air entering the CPOx reformer is first extracted from the CFD model and used as an input to the CPOx model. The state of reformate within the fuel plenum is extracted and used as the anode flow inlet condition for the 1-D tube model. The CPOx and the TGC models provide a critical coupling of the fuel reforming and the combustion of unspent fuel to the CFD and tube models, thereby capturing the full performance of the overall SOFC system.

4.7.1 CPOx Model

The CPOx reformer is a porous disc with a catalyst coating that reforms the preheated fuel/air mixture leaving the CFD domain. A gaseous mixture of fuel, n-hexadecane, and air is converted to syngas via the overall reaction below.

$$C_{16}H_{34} + 8\left(O_2 + 3.76N_2\right) \Leftrightarrow 16CO + 17H_2 + 30.0N_2 \tag{4.11}$$

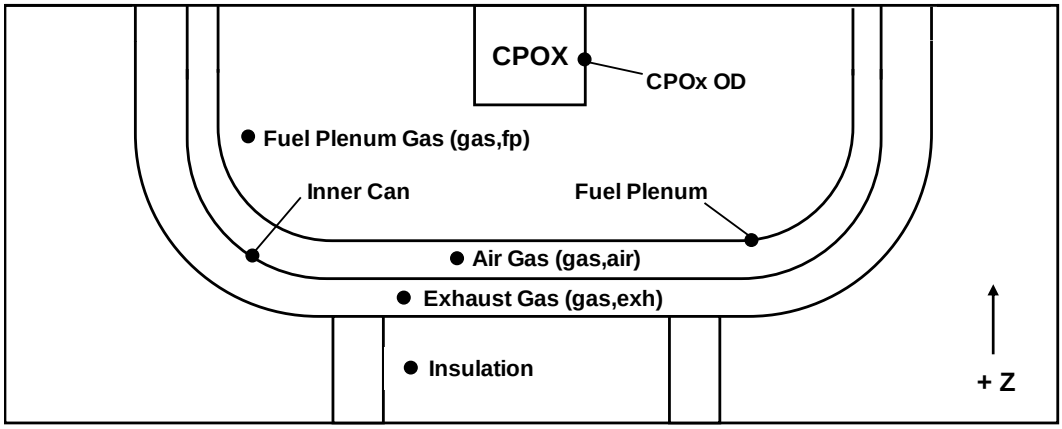

(a)

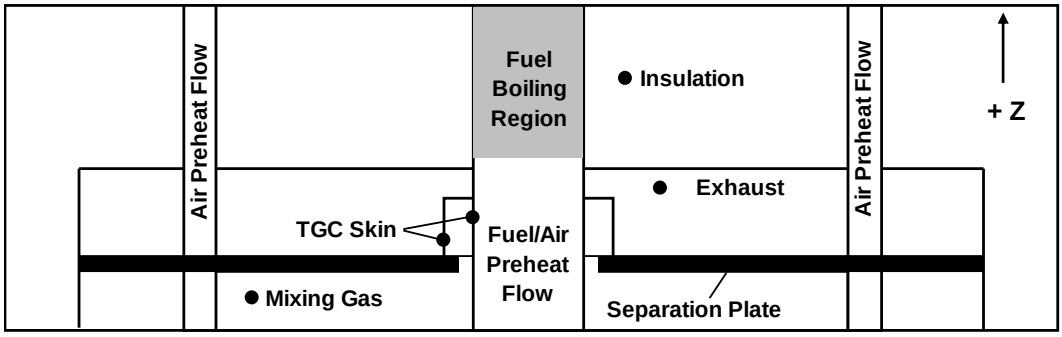

(b)

Figure 4.6 Lumped surface definitions in both the CPOx and TGC thermal resistance models. Conduction heat transfer is modeled through solids (expect CPOx and TGC reactors) yielding an inner and outer lumped surface temperature on solids. Only one surface node is shown on solid surfaces for clarity.

It is essential to couple a CPOx model to accurately predict system performance. As an example, conditions within the CFD model, such as extent of fuel/air preheat, directly effect the temperature of reformate leaving the CPOx which subsequently enters the anode of the tube model. The CPOx model domain extends from the bottom of the inlet tube-sheet to the bottom of the system insulation (see Figure 4.2) and also includes anode gas flow through the non-active tube lengths within the inlet tube-sheet, as discussed in Section 4.6.6. A quasi 1-D thermal resistance model created in Python [37] is applied to the CPOx domain, as shown in Figure 4.7, to capture thermal and fluid interactions occurring in/around the CPOx reformer. Reformate leaving the CPOx reformer is assumed to be in chemical equilibrium [38,39]. Within the thermal resistance model is a CPOx reformer, fuel plenum wall, fuel plenum gases, an inner can that separates the air

channel from the exhaust channel, air and exhaust gases located within the channels, and insulation as shown in Figure 4.6.

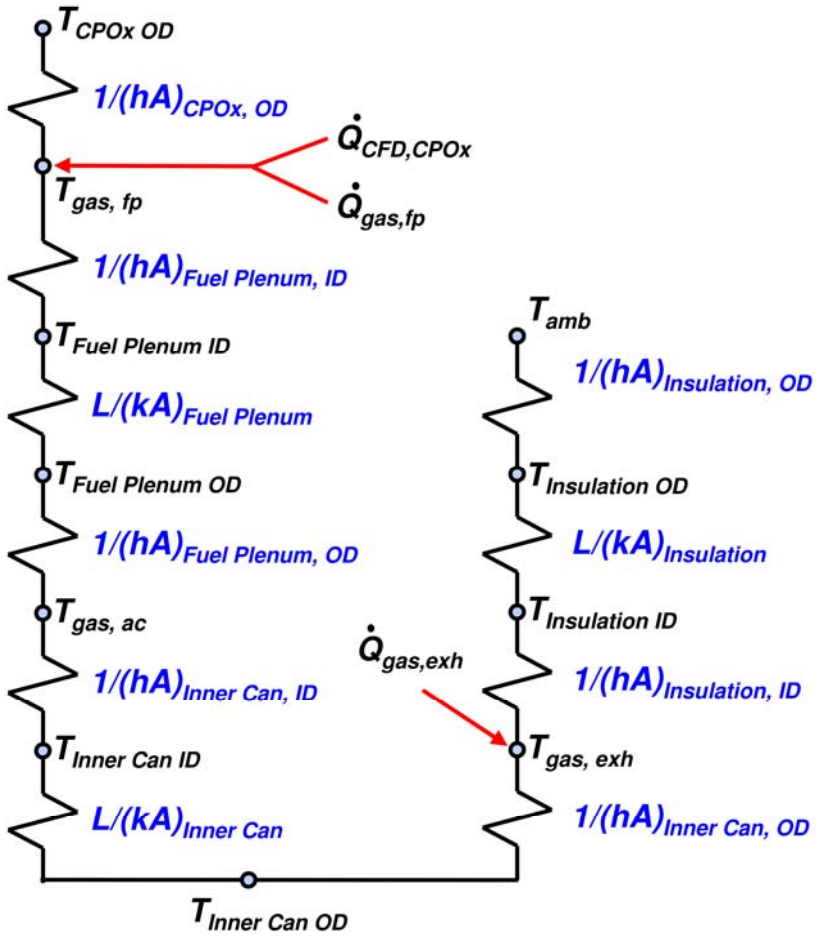

Figure 4.7 CPOx model thermal resistance network

4.7.1.1 Thermal Resistance Model

Convection and conduction heat transfer are modeled within the CPOx region assuming lumped surface temperatures on all components (see Figure 4.6 for lumped surface locations). The surface temperature of the CPOx reformer is taken as the average of the inlet and outlet gas temperatures. Thermal coupling within the CPOx domain is accomplished through a series of energy balances on all surfaces and the gases within the fuel plenum and exhaust channel. The convective heat transfer, $\dot{Q}_{conv,i}$, from any surface *i* is calculated as:

$$\dot{Q}_{conv,i} = hA_i\left(T_i - T_{gas,j}\right) \tag{4.12}$$

where T_i is the lumped temperature and A_i is the area of surface i and $T_{gas,j}$ is the free stream temperature of gas in contact with surface i. A common convective heat transfer coefficient, h, is used throughout the CPOx domain. In order to capture the presence of radiation heat transfer without the added complexity of solving non-linear equations, an effective heat transfer coefficient higher than a convectional convective heat transfer coefficient is used. A value of 100 W/m^2-K is chosen to represent heat transfer throughout the CPOx domain. While there is uncertainty surrounding this value, the heat transfer coefficient is seen as a tuning parameter which can be varied in order to match model predictions to experimental data. Future publications will also investigate the sensitivity of system parameters to the chosen CPOx heat transfer coefficient.

$$h = h_{conv} + h_{rad} = 100\,W/m^2 - K \tag{4.13}$$

Conduction, $\dot{Q}_{cond,i}$, through solid regions i is calculated as:

$$\dot{Q}_{cond,i} = (T_{i,inner} - T_{i,outer}) \cdot \left(\frac{L_i}{k_i A_{avg,i}}\right)^{-1} \tag{4.14}$$

where $T_{i,inner}$ and $T_{i,outer}$ are the surface temperatures of solid region i, $A_{avg,i}$ is the average surface area between the inner and outer surfaces of solid region i, and L_i is the thickness of the solid region.

Reformate gas flow within the fuel plenum cavity and exhaust channel gas flow is assumed to be perfectly mixed. Because gas flows entering the CPOx domain are not at the perfectly mixed gas temperature, thermal energy exchange is captured by $\dot{Q}_{gas,i}$ as follows.

$$\dot{Q}_{gas,i} = \dot{m}_i Cp_i\left(T_{i,in} - T_{gas,i}\right) \tag{4.15}$$

where $\dot{Q}_{gas,i}$ is the amount of thermal energy added at each gas volume node i, ($T_{i,in}$ – $T_{gas,i}$) is the temperature difference between the gas entering the volume and the perfectly

mixed temperature, $\dot{m}_i$ is the flow rate, and Cp_i is the specific heat calculated at the average of the inlet and perfectly mixed temperatures. Anode gas flow inside the inactive tube ends is added to the fuel plenum cavity volume. During the physical steady-state operation of this system, all air flowing down the recuperator enters the cathode and no air flow enters the air channel surrounding the fuel plenum; therefore, there is no thermal energy source, $\dot{Q}_{gas,i}$, in the air channel, Figure 4.7.

4.7.1.2 Model Integration to System Model

The thermodynamic state of all flow inlets to the CPOx model which include the fuel/air preheat and exhaust leaving the recuperator are extracted from FLUENT via the UDF. The equilibrium CPOx reformate is sent as the anode inlet condition to the stack. A perfectly mixed condition is applied within the fuel plenum; therefore, reformate is uniform in temperature, pressure, and composition entering the anode of all tubes within the bundle. Besides flow interfaces, there are also solid interfaces at the CPOx boundary between the CFD and tube models. Adiabatic boundary conditions are applied at the interfaces of the system insulation and the inner can wall. The top of the fuel plenum cavity as well as anode gas channels in inactive tube sections are bound by surfaces within the CFD model. At these CFD surfaces a convective thermal boundary condition is applied with h = 100 W/m^2-K and a free stream temperature equal to the fuel plenum gas temperature as calculated in the CPOx thermal resistance model. The total heat transfer at the interface calculated by the CFD model, $\dot{Q}_{CFD,CPOx}$, is added to the energy balance at the fuel plenum gas node within the CPOx thermal model.

4.7.2 TGC Model

The TGC is a porous annular disk in which unspent fuel from the stack is oxidized with cathode exhaust gases. TGC exhaust then enters the CFD domain at the recuperator hot flow inlet. As with the CPOx model, it is essential to couple the TGC model to the system. As an example, if the tube model predicts low stack power, an increase in unspent fuel will increase the TGC exhaust temperature which indirectly increases the

temperature of air leaving the recuperator, i.e. entering the cathode. A higher cathode inlet temperature acts to increase tube temperatures and power output; therefore, TGC coupling acts to regulate stack power. The TGC model domain extends from the top of the outlet tube-sheet to the top of the system insulation (see Figure 4.2) and also includes the anode gas flow through the inactive tube lengths within the outlet tube-sheet, as discussed in Section 4.6.6. A quasi 1-D thermal resistance model created in Python is applied to the TGC domain, as shown in Figure 4.8, to capture thermal and fluid interactions occurring associated with the TGC. Complete combustion is assumed within the TGC [18,25]. The TGC domain consists of a mixing region where stack cathode and anode exhaust gases mix, a combustor, combustor exhaust cavity, fuel/air preheat tube flow, air preheat tube flow, insulation, and a separating plate that separates the mixing region from the TGC exhaust cavity, as shown in Figure 4.6.

4.7.2.1 Thermal Resistance Model

Convection and conduction heat transfer are modeled in the same manner as in the CPOx model where all surfaces are at lumped temperatures within the TGC control volume (see Figure 4.6 for lumped surface locations). The surface temperature of the TGC is taken as the average of the inlet and outlet gas temperatures. An effective heat transfer coefficient is used in the TGC domain with the same value as used in the CPOx model (see Eq. (4.13)). A perfectly mixed gas condition is applied to the mixing region and the TGC exhaust gas cavity as given in Eq. (4.15).

4.7.2.2 System Air Flow Preheat Modeling

The TGC domain also has pipe flows used to preheat system streams of fuel/air and air. Pipe flow is not perfectly mixed, and the conductive resistance of the solid pipes is assumed negligible. There are four air preheat flow tubes within the TGC domain (only two seen in cut view of Figure 4.6).

A turbulent ($Re \approx 5000$) pipe flow Nusselt number relation is used in creating a mass flow rate functional dependence for the heat transfer coefficient within air preheat tubes.

$$h_{air,preheat} = 59664 \cdot \dot{m}_{air}^{0.887} \tag{4.16}$$

where $\dot{m}_{air}$ is the mass flow rate (kg/s) of air per air preheat tube.

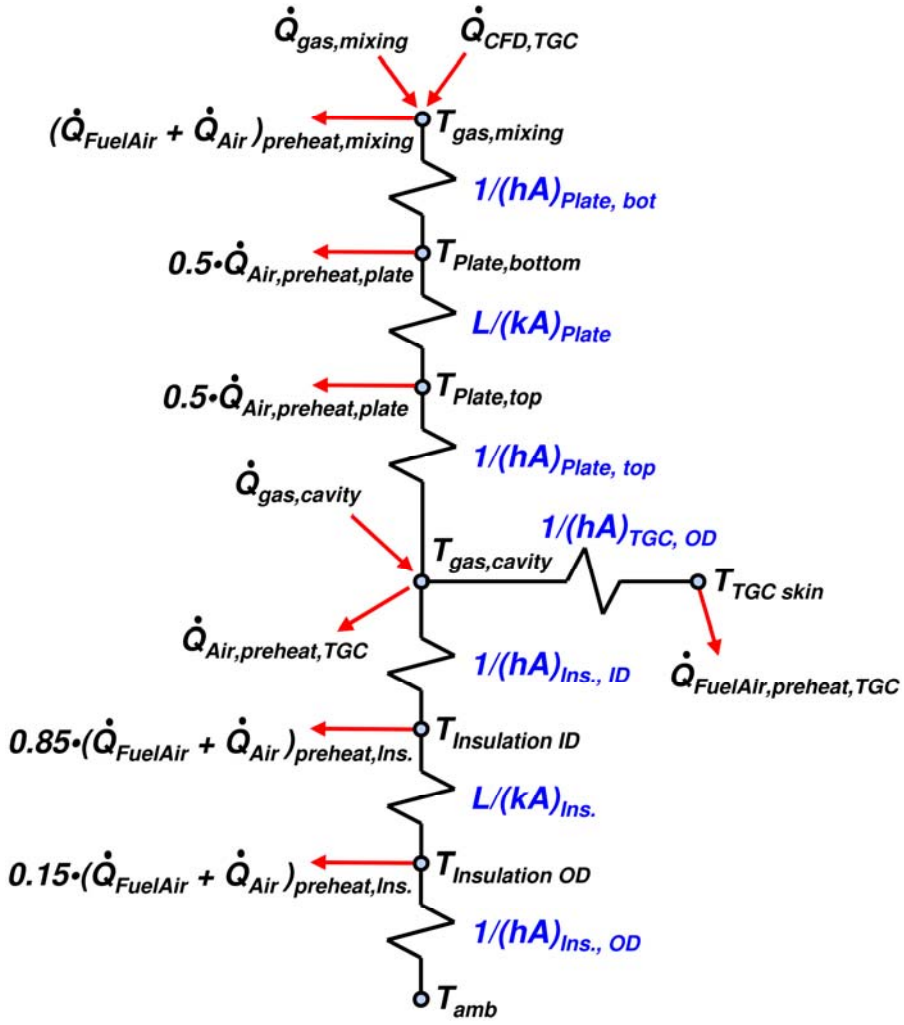

Figure 4.8 TGC model thermal resistance model

The air flow tubes pass through four regions of the TGC domain, namely the insulation, TGC exhaust cavity, separation plate, and mixing region. The magnitude of heat transfer from each region to preheat air flow is calculated by combining energy

balances and rate equations applied at each region the air flow tubes pass through. The rate of heat transfer in each region is defined as:

$$\dot{Q}_{air,i} = h_{air,preheat} A_{air,i} \left(T_{avg,i} - T_{air,avg,i} \right) \tag{4.17}$$

where $\dot{Q}_{air,i}$ is the thermal energy transferred into the air flow traveling through tube region *i* having surface area $A_{air,i}$, $T_{avg,i}$ is an average temperature representing the air flow tube region *i*. When the tube borders a solid region, $T_{avg,i}$ is the average between the inner and outer solid surface temperatures. When the tube borders a gas cavity, $T_{avg,i}$ is the perfectly mixed gas temperature. Air flow temperatures are calculated at the periphery of every region that the flow tube intersects; therefore, $T_{air,avg,i}$ is the average between the inlet, $T_{air,in,i}$, and outlet, $T_{air,out,i}$, air temperature within region *i*. Energy balances are applied to air flow in each region *i* as:

$$\dot{Q}_{air,i} = \dot{m}_{air} Cp_{air} \left(T_{air,out,i} - T_{air,in,i} \right) \tag{4.18}$$

where Cp_{air} is the specific heat representing air within the preheat tube and is evaluating at the average temperature of air into and out of the entire TGC domain.

4.7.2.3 System Fuel/Air Flow Preheat Modeling

Fuel/air preheating occurs in the centrally located fuel inlet flow tube. In the physical system, fuel is injected, mixing with air, by an atomizing spray nozzle. The spray nozzle is located at the outer periphery of the insulation. A physical spray nozzle is not modeled within the TGC, but to simulate this boundary condition, a mixture of liquid fuel and gaseous air enter the preheat tube at a common temperature. Within the tube, atomized fuel droplets are rapidly vaporized. Heating of the vaporizing fuel and gaseous air mixture is modeled by considering the air and liquid fuel components separately. An energy balance coupled to a rate equation calculates the tube area where vaporization occurs. $\dot{Q}_{f/a,vap}$ is the total energy required to first sensibly heat liquid fuel and gaseous

air to the boiling temperature of the fuel and the latent energy required to completely vaporize the fuel.

$$\dot{Q}_{f/a,vap} = \dot{m} C_p \left(T_{boil} - T_{f/a,in} \right)_{air} + \dot{m} \left[h_{fg} + C_{p,liq} \left(T_{boil} - T_{f/a,in} \right) \right]_{fuel} \qquad (4.19)$$

where T_{boil} is the boiling temperature of the fuel, $T_{f/a,in}$ is the fuel/air temperature into the TGC domain, and h_{fg} (359 kJ kg^{-1} for n-hexadecane) is the latent heat of vaporization. The mass flow rate of air and fuel entering the preheat tube are $\dot{m}_{air}$ and $\dot{m}_{fuel}$, respectively. $Cp_{liq,fuel}$ is the specific heat of liquid fuel used in calculating the sensible heating of liquid fuel. Cp_{air} is calculated at the average of the inlet and boiling temperatures.

The rate at which $\dot{Q}_{f/a,vap}$ is transferred is calculated as:

$$\dot{Q}_{f/a,vap} = h_{boil} A_{f/a,vap} \left[T_{f/a,tube} - \left(\frac{T_{f/a,in} + T_{boil}}{2} \right) \right] \qquad (4.20)$$

where $A_{f/a,vap}$ is the surface area of the fuel/air preheat tube from the inlet to the location of complete fuel vaporization. $T_{f/a,tube}$ is an area-averaged temperature of the entire fuel/air preheat tube. A high convective heat transfer coefficient, h_{boil} = 2000 W/m^2-K, is used in the preheat tube as a simplified means to simulate fuel vaporization. Rather than performing a detailed analysis involving non-dimensional groups, h_{boil} is estimated from boiling curves (Figure 10.4 in Reference [29]). This rough estimate is appropriate because system-level predictions are not sensitive to h_{boil}. For example, an h_{boil} = 1000 W/m^2-K only decreases the fuel/air temperature leaving the TGC domain by 0.7°C while increasing h_{boil} to 3000 W/m^2-K only increases the fuel/air outlet temperature by 0.3°C. The fuel/air outlet temperature is not sensitive to h_{boil} because of the low convective coefficient once fuel is vaporized dominates the rate of heat transfer as discussed in the following.

After the fuel has completely vaporized, another coupled energy balance and rate equation is applied to determine the extent of fuel/air preheating before entering the CFD domain. In this flow region, a lower convective heat transfer coefficient, $h_{f/a,pre}$ = 9.6 W/m^2-K, is used. $h_{f/a,pre}$ is based on a laminar, $Re \approx 1000$, pipe flow Nusselt number relationship with the assumption of fully developed flow. The amount of sensible heating to the fuel/air gas mixture, $\dot{Q}_{f/a,gas}$, is calculated as

$$\dot{Q}_{f/a,gas} = \dot{m}_{f/a} Cp_{f/a} \left(T_{f/a,out} - T_{boil} \right) \tag{4.21}$$

where $T_{f/a,out}$ is the temperature of fuel/air gas leaving the fuel/air preheat tube. The combined air and fuel flow rate is $\dot{m}_{f/a}$ and $Cp_{f/a}$ is the specific heat of the mixture calculated at the average outlet and boiling temperatures.

The rate of $\dot{Q}_{f/a,gas}$ is calculated with:

$$\dot{Q}_{f/a,gas} = h_{f/a.gas} A_{f/a,gas} \left[T_{f/a,tube} - \left(\frac{T_{boil} + T_{f/a,out}}{2} \right) \right] \tag{4.22}$$

where $A_{f/a,gas}$ is the surface area of the fuel/air preheat tube from complete fuel vaporization to the outlet of the fuel/air tube. It should be noted that the area-averaged temperature of the entire fuel/air preheat tube is used in calculating the driving potential in Eqs: 4.20 and 4.22. The reasoning being that the location of complete fuel vaporization is dependent on system-level operating parameters and TGC model dimensions. With the location of complete vaporization unknown, it is difficult to calculate an area averaged fuel/air preheat tube in both the vaporizing and gaseous fuel sections.

4.7.2.4 Model Integration into System Model

The thermodynamic state of all flow inlets entering the TGC model which include the cathode and anode exhaust are extracted from FLUENT and the tube model via the UDF. The state of preheated fuel/air and preheated air along with the state of TGC exhaust

leaving the TGC domain are sent as inlet conditions to the CFD model. As in the CPOx model, there are also solid interfaces at the TGC boundary between the CFD and tube models. Adiabatic boundary conditions are applied at the interfaces of the system insulation, fuel/air preheat tube, and air preheat tube. The bottom of the mixing region as well as anode gas channels in inactive tube sections are bound by surfaces within the CFD model. At these CFD surfaces a convective thermal boundary condition is applied with h = 100 W/m^2-K and a free stream temperature equal to the mixing gas temperature as calculated in the TGC thermal resistance model. The total heat transfer at the interface calculated by the CFD model, $\dot{Q}_{CFD,TGC}$, is added to the energy balance at the mixing gas node within the TGC thermal model.

4.8 System Pressure

Pressure drops are calculated within the CFD and tube models, but pressure drop calculations are not contained within the CPOx and TGC models. Because pressure is not tracked throughout the entire system, pressures need to be specified at every CFD flow outlet and at the anode flow inlet to the tube model. The outlet pressures of the fuel/air preheat, cathode exhaust, and recuperator exhaust are set to match pressures extracted from the developer of the 650 W system. In this manner, pressure outlets do not change with operating conditions, but the pressure drops calculated within the components do change with operating conditions.

Physically, the anode outlet pressure equalizes to the cathode outlet pressure. To achieve an anode outlet pressure equal to the cathode outlet pressure, the anode inlet pressure needs to be set as follows.

$$P_{anode,inlet} = P_{cathode,outlet} + \Delta P_{cell} \tag{4.23}$$

where ΔP_{cell} is the pressure drop within the anode gas channel of the cell. In most applications, ΔP_{cell} is very small, ~ 2 Pa, in comparison to the cathode pressure outlet; therefore, a simplification is made in which ΔP_{cell} is assumed negligible.

$$P_{anode,inlet} = P_{cathode,outlet} \tag{4.24}$$

A negligible pressure drop is assumed in the preheat tubes located in the TGC model. A ΔP is seen in flows that enter the TGC or CPOx domain originating from the CFD or tube model. A ΔP develops because of the independent setting of pressures in the CFD and tube models. Any ΔP within the CPOx and TGC is assumed negligible as pressure drop is not incorporated into the energy equations.

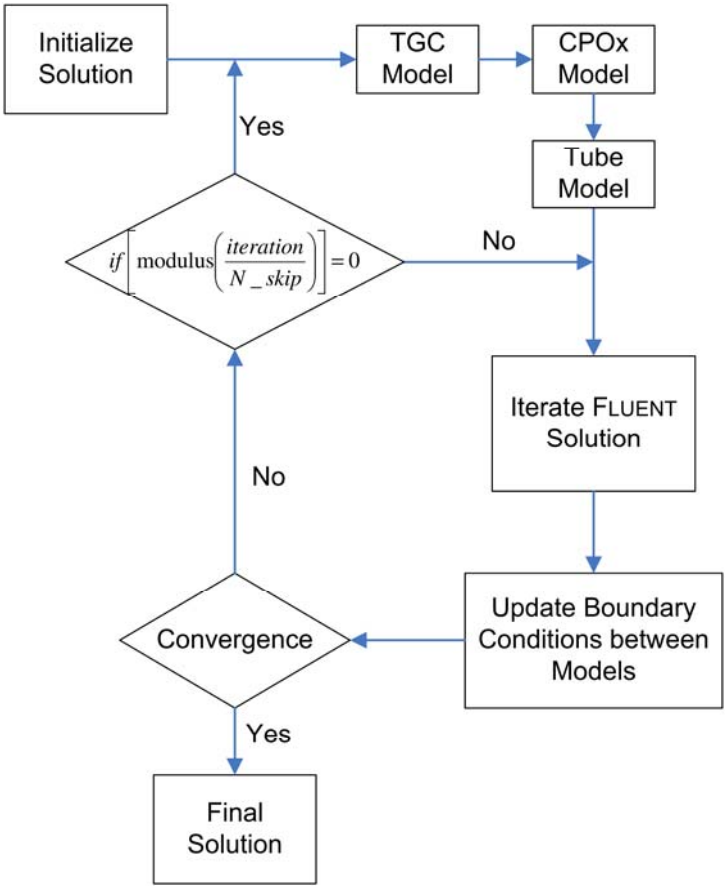

Figure 4.9 Block diagram illustrating the calling sequence of the component models to create the system model

4.9 System Solution Procedure

Figure 4.9 illustrates the calling sequence to all the component models in the system model. After the flow field is initialized, the TGC, CPOX, and tube models are called sequentially. FLUENT then iterates, solving its governing equations. The boundary

conditions for every model are updated after each FLUENT iteration. If a converged solution has not been calculated, an if statement is evaluated. If evaluated to No, FLUENT utilizes the boundary conditions from the last time the TGC, CPOx, and tube models were called. *Iteration* is the current FLUENT iteration and *N_skip* is the number of sequential FLUENT iterations without calling the TGC, CPOx, and tube models. As mentioned in Section 4.4.3, *N_skip* is set to five, but an optimal value can be found to reduce computational time.

4.10 Model Inputs / Outputs

Table 4.2 attempts to summarize the overall system-level inputs, outputs, and parameters for the system model. Not all outputs are automatically calculated such as efficiency, but they may readily be calculated with an accompanying data analysis file. Numerous results can also be extracted from the resulting CFD solution.

Table 4.2 System Model Inputs, Outputs, and Parameters

Inputs		**Outputs**	
Fuel flowrate	[kg/s]	Cell voltages	[V]
Air flowrate for CPOx	[kg/s]	Cell powers	[W]
Air flowrate for cathode	[kg/s]	Stack efficiency	[% HHV]
Cell current	[A]	Exhaust temperature	[K]
Inlet fuel/air temperature	[K]	Exhaust composition	[K]
Inlet air temperature	[K]	System efficiency	[% HHV]
Ambient temperature	[K]	Insulation heat loss	[W]
Ambient pressure	[Pa]	Insulation skin temperature	[K]
Model Parameters			
Material properties		TGC domain heat transfer coefficients	
CPOx domain heat transfer coefficient		External heat transfer coefficient	

As discussed, the system model is comprised of four component models. Each component model has a unique set of input files storing model parameters and geometry. Additionally, the UDF passes information between component models via data files. A complete listing of the input and output files for each component model is listed in Table

4.3. The output file to one model becomes the input file to another, thus interconnecting the system. A description of the contents of each file appears in the APPENDIX. Files shown in bold contain input parameters/conditions for the system model.

Table 4.3 Component Models Input/Output Files

Model	Input Files	Output Files
Tube Model	**ParameterInputs.dat**	qMEAinjO2.csv
	InputVariablesNew.dat	Tube_Power.txt
	CPOX_Outlet.dat	Tube_Fuel_Outlets.dat
	AirState.csv	
	TubeInletOutletTemp.dat	
CFD Model	**UDF_Inputs.txt**	AirState.csv
	Tube_Tip_IDs.txt	TubeInletOutletTemp.dat
	surface_ids.txt	CPOX_Inlet.dat
	emissivity.dat	TGC_Inlet.dat
	qMEAinjO2.csv	
	TGC_Outlet.dat	
CPOx Model	**System_Inputs.dat**	CPOX_Outlet.dat
	CPOX_Inputs.dat	
	CPOX_Inlet.dat	
	TGC_Outlet.dat	
TGC Model	**Stack_Parameters.dat**	TGC_Outlet.dat
	System_Inputs.dat	
	TGC_Inputs.dat	
	TGC_Inlet.dat	
	UDF_Inputs.txt	
	Tube_Fuel_Outlets.dat	

4.11 Baseline Simulation

The objective of the simulation is to demonstrate the capabilities and utility of the developed, highly-integrated SOFC modeling tool. To begin, an energy and mass balance are calculated to check the integrity of the system model. System-level results are presented illustrating the capability of the model to highlight ineffective system designs. Next, a detailed stack analysis illustrates the non-uniform performance within the stack and the usefulness of the model to stack developers.

The nominal gross electric power output of the SOFC system is 650 W. Thus, the electrical power target for the simulation was ± 10% of the nominal value . To vary bundle power without changing inlet conditions, the insulation thickness around each modeling domain (CFD, CPOx, and TGC) was varied by a common factor. Utilizing a 2X insulation factor, the system model resulted in 633 W gross electrical power with insulation 30, 24, and 31.5 mm thick surrounding the CFD, CPOx, and TGC domains, respectively.

4.12 Input Parameters

The symmetric tube bundle, shown in Figure 4.1, was simulated yielding 19 independent tube simulations. Inlet conditions and system parameters applicable to a 650 W stack were supplied by the SOFC developer and are summarized in Table 4.4. The amount of stoichiometric air, λ_{air}, for this hexadecane fueled system is calculated using the following,

$$\lambda_{air} = \left(\frac{\dot{n}_{O_2}}{24.5 \cdot \dot{n}_{C_{16}H_{34}}} \right)_{system\ inlet} \tag{4.25}$$

Ambient conditions of T_{amb} = 20°C and P_{amb} = 83 kPa surround the system insulation. The thermal boundary imposed to the outer insulation surface surrounding the system is convective with h = 10 W/m^2-K. In addition to convection, a radiation pathway is imposed at the insulation periphery in the CFD model, but the addition of radiation has little to no effect because of the low insulation skin temperatures, ~50°C.

Table 4.4 Simulation Parameters

Fuel/Air Inlet		Air Inlet		Stack		System	
Fuel Type	$C_{16}H_{34}$	T [°C]	20	j_{avg} [A/cm^2]	0.349	CPOx: O/C	1.1
T [°C]	40	P [kPa]	84.37			λ_{air}	2.55
P [kPa]	92.65						

4.13 Verification of System Model Integrity – Energy and Mass Residuals

The integrity of the system model was verified by performing mass and energy balances around the system and component models. The resulting residuals are shown in Table 4.5. The total energy residual on the system is 0.50% of total energy input into the system and the combined CFD plus tube bundle energy residual is less than 2% of SOFC stack power. Mass balances across the TGC and CPOx models with a slight imbalance seen in the CFD plus tube bundle model. This mass imbalance is very low being less than 5% of the relatively small O_2 mass consumed in the stack.

Table 4.5 Energy and mass residuals for baseline simulation

	Energy Residual			Mass Residual		
Model	Value [W]	% Total Inlet Energy	% SOFC Power	Value [g/s]	% Total Inlet Flow	% O_2 Consumed in Stack
System	14.9	0.5%	2.3%	-3.4E-4	0.01%	4.2%
CFD+Tube Bundle	12.4	0.4%	1.9%	-3.4E-4	0.01%	4.2%
TGC Region	1.9	0.1%	0.3%	0.0	0.00%	0.0%
CPOx Region	0.6	0.0%	0.1%	0.0	0.00%	0.0%

4.14 Simulation of the SOFC System

The SOFC power generator is simulated operating on a liquid hexadecane fuel. Simulation results are presented for both the overall system and for the tube bundle. Table 4.6 presents the thermodynamic states throughout the system with statepoints corresponding to Figure 4.10. The energy content at each statepoint is the summation of (i) thermal energy released when cooled to the ambient temperature, (ii) chemical energy released with the oxidation of any fuels present, and (iii) latent energy associated with condensing water if present.

System air is preheated from 20° to 668°C before entering the cathode at statepoint 3. The fuel/air gas mixture is preheated from 40° to 422°C (statepoint 7) prior to entering the CPOx reformer and subsequently enters the anode at 816°C (statepoint 9). The bundle at an average temperature of 745°C produces 637 W of gross power at 43.3 V and 14.72 A. TGC exhaust gases enter the recuperator at 868°C (statepoint 13), leaving the recuperator at 656°C (statepoint 14), and finally are heated slightly while flowing through the CPOx domain leaving the system at 682°C (statepoint 15). The co-flow recuperator leads to a high system exhaust temperature. Of the 3.01 kW of energy entering the system, 75% is convected away through exhaust gases with 21% converted to DC electrical power in the SOFC tube bundle. Conductive heat loss through system insulation only accounts for 3% of total system energy input.

The predicted CPOx reformer exhaust temperature, 1218°C, could lead to sintering within the reformer. Heat loss from the reformer is directly coupled to the estimated reformer skin temperature used within the thermal resistance network. Averaging inlet and outlet gas flow temperatures to estimate the CPOx skin temperature adds uncertainty to the thermal model. Experimental temperature profile data of the reformer would remove the uncertainty surrounding the CPOx skin temperature and predicted CPOx exhaust temperature.

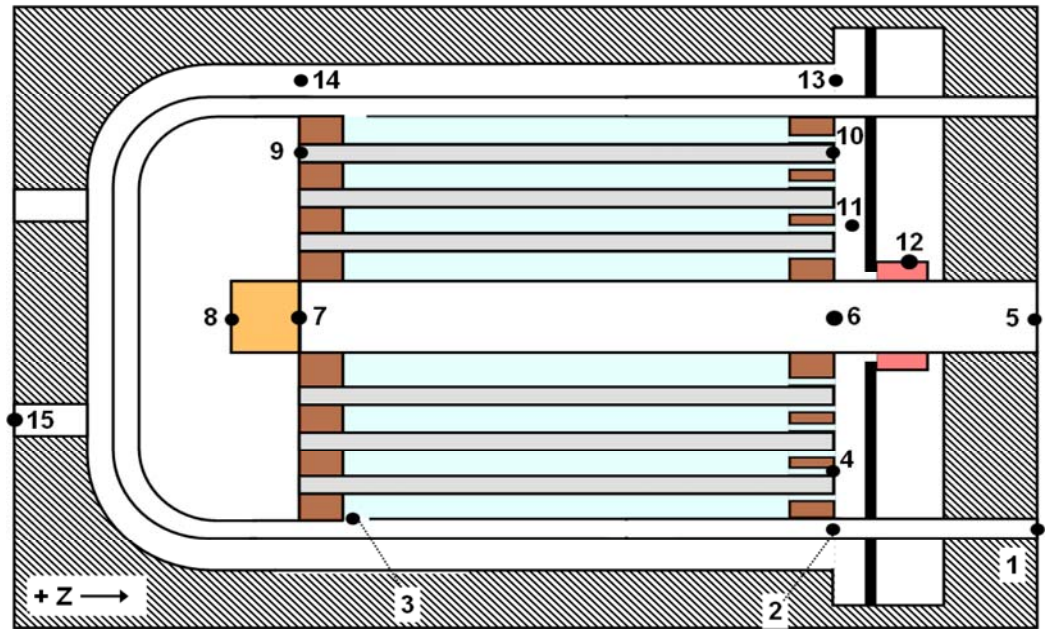

Figure 4.10 System process statepoint locations

Table 4.6 Baseline System Statepoints

State-point	T [°C]	P [kPa]	Flowrate [g/s]	Molar Composition								E [W]
				H_2	CO	CH_4	$C_{16}H_{34}$	CO_2	H_2O	O_2	N_2	
1	20	84.37	2.410	0.0	0.0	0.0	0.00	0.0	0.0	0.21	0.79	0
2	111	84.37	2.410	0.0	0.0	0.0	0.0	0.0	0.0	0.21	0.79	223
3	668	84.25	2.410	0.0	0.0	0.0	0.0	0.0	0.0	0.21	0.79	1,664
4	699	84.22	2.330	0.0	0.0	0.0	0.0	0.0	0.0	0.19	0.81	1,695
5	40	92.65	0.402	0.0	0.0	0.0	0.02	0.0	0.0	0.21	0.77	3,010
6	294	92.65	0.402	0.0	0.0	0.0	0.02	0.0	0.0	0.21	0.77	3,157
7	422	92.65	0.402	0.0	0.0	0.0	0.02	0.0	0.0	0.21	0.77	3,227
8	1218	92.65	0.402	0.24	0.24	0.0	0.0	0.01	0.02	0.0	0.50	3,226
9	816	84.22	0.402	0.24	0.24	0.0	0.0	0.01	0.02	0.0	0.50	2,974
10	718	84.22	0.483	0.10	0.10	0.0	0.00	0.14	0.16	0.0	0.50	1,633
11	716	84.22	2.813	0.02	0.02	0.0	0.0	0.03	0.03	0.15	0.76	3,371
12	999	84.22	2.813	0.0	0.0	0.0	0.0	0.05	0.05	0.13	0.77	3,345
13	868	83.27	2.813	0.0	0.0	0.0	0.0	0.05	0.05	0.13	0.77	2,889
14	656	83.22	2.813	0.0	0.0	0.0	0.0	0.05	0.05	0.13	0.77	2,177
15	682	83.00	2.813	0.0	0.0	0.0	0.0	0.05	0.05	0.13	0.77	2,264
Power												637
Heat Loss												94

Table 4.7 highlights the predicted operating conditions of the system utilizing the following definitions,

$$U_F = \frac{\left(\dot{n}_{H_2}\right)_{stack\ consumed}}{\left(4\dot{n}_{CH_4} + \dot{n}_{H_2} + \dot{n}_{CO}\right)_{anode\ inlet}} \tag{4.26}$$

$$U_{ox} = \frac{\left(\dot{n}_{O_2}\right)_{stack\ consumed}}{\left(\dot{n}_{O_2}\right)_{cathode\ inlet}} \tag{4.27}$$

$$\eta_{system} = \frac{P_{DC,stack}}{\left(\dot{n}_{fuel} \cdot HHV_{fuel}\right)_{system\ inlet}} \tag{4.28}$$

$$\eta_{SOFC} = \frac{P_{DC,stack}}{\left(\dot{n}_{fuel} \cdot HHV_{fuel}\right)_{anode\ inlet}} \tag{4.29}$$

where U_F is the fuel utilization and U_{ox} is the oxygen utilization within the stack, η_{system} and η_{SOFC} are the system and stack efficiencies, respectively. $P_{DC,stack}$ is the DC power output from the stack and found in both efficiency definitions because power conditioning is not modeled in this study. The relatively low system efficiency registered in this simulation is consistent with SOFC developer performance and substantially affected by the low fuel utilization.

Table 4.7 Baseline System Operating Conditions

$P_{cathode,\ avg}$ [kPa]	$P_{anode,\ avg}$ [kPa]	U_F	U_{Ox}	η_{SOFC}	η_{system}
84.24	84.22	0.54	0.14	25.1%	21.1%

4.15 Tube Bundle Results

Tube bundle performance is investigated with the aim of understanding tube temperature and oxygen distributions, flowfield characteristics, and identification of potential model reduction methods by strategic groupings of tubes.

4.15.1 Tube Performance Groupings

For every tube in the bundle, radiation is observed to be the dominant heat transfer mechanism for stack cooling at the outer tube surface. The annular stack can surrounding the bundle separates the cathode gases from the relatively cold air being preheated in the recuperator. The stack can has a non-linear temperature distribution with a maximum of 691°C, a minimum of 523°C, and a 621°C average temperature. With the average bundle temperature at 745°C, a large temperature driving force for radiation heat transfer to the stack can exists. Tubes with larger radiation view factors to the stack can are observed to transfer a proportionally larger amount of radiation thermal energy causing their temperatures to decrease along with tube power. Power disparities are observed within the bundle as cell power ranges from 7.6 - 10.8 W with an average of 9.7 W.

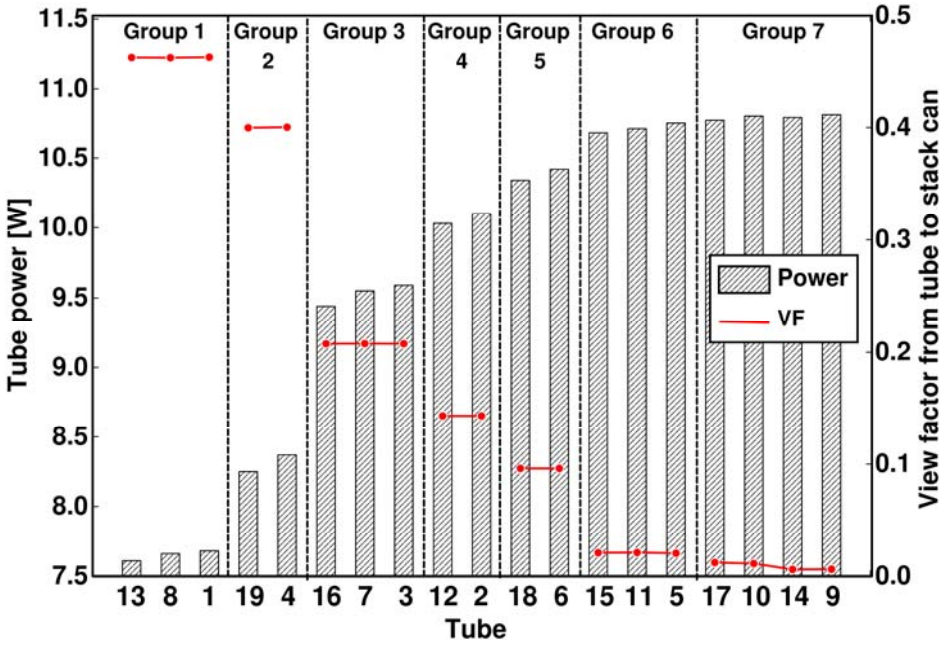

Figure 4.11 Plot of tube power and view factor from tube to stack can surface for every tube in bundle. Arranged in groupings of similar view factors. (See Figure 4.1 for cell numbering)

Power disparities are largely due to a strong functional relationship between the power output of a tube and the view factor from the tube to the stack can. This relationship is shown in Figure 4.11 where the tubes are arranged in increasing power output on the *x*- axis. Tubes with similar view factors to the stack can also have very

similar power outputs. For the bundle configuration under study, seven view factor groupings exist which lead to seven tube power groupings. Groupings 6 and 7 could be combined into a single power group, but they are left as distinct groups because of differences in axial temperature profiles which is discussed further in Section 4.15.2. Variations in tube performance point to the potential for substantial inaccuracy in stack power prediction if single-tube performance is extrapolated to emulate the performance of an entire tube bundle. Resulting power groupings suggest at least six if not seven tube simulations are required in order to predict the performance of the stack, where each tube simulation requires a unique set of thermal boundary conditions.

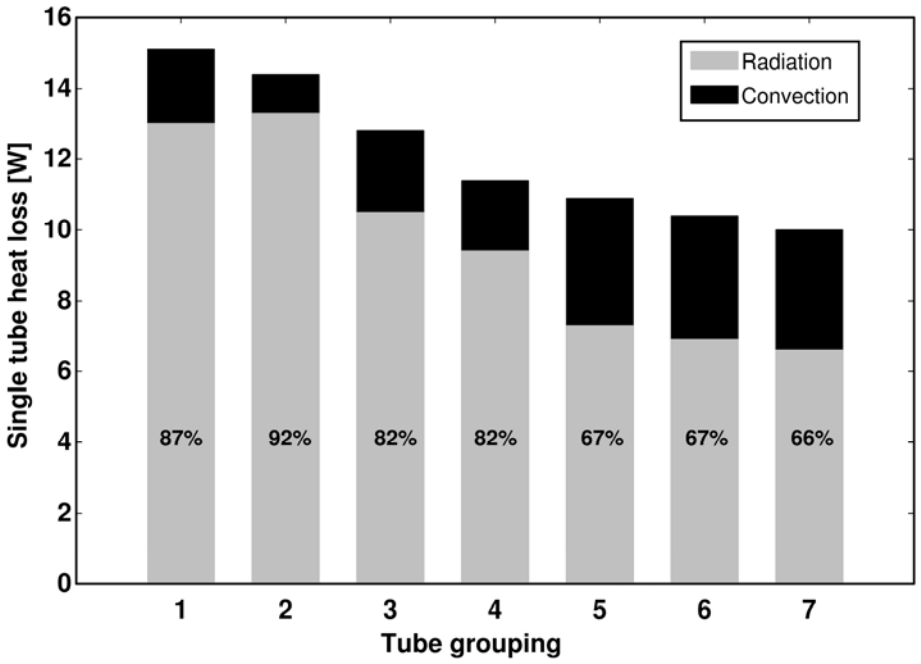

Figure 4.12 Total heat transfer from outer surface of cells. Contribution of radiation and convection shown with percentage of radiation overlaid on graph. Heat transfer is averaged within tube groupings.

The dominance of radiation in the bundle is explicitly illustrated in Figure 4.12 where individual tube values have been averaged within power groupings. For tubes located closer to the stack radial center, outer radial periphery tubes act as radiation shields effectively blocking the view to the relatively cold stack can. This is convincingly seen in Figure 4.12 where the outer radial tubes (groups 1&2) have the greatest percentage of radiation loss, 87-92%, compared to inner radial tubes (groups 6 & 7) where 66-67% of

heat transfer is due to radiation. Because of this shielding, tube power groupings are also a function of radial tube location. Referring to tube numbering in Figure 4.1, tubes at inner radii produce the greatest power and tubes at outer bundle radii producing the lowest power as shown in Figure 4.11.

Because the stack is wired in electrical series, cell voltage varies throughout the bundle as shown in Figure 4.13. Cell voltages vary from 0.52 - 0.73 V at the lowest power and highest power tubes, respectively. Voltages lower than 0.6 V occurring in tube groupings 1 and 2 are of concern as oxygen ions may begin to oxidize Ni in the anode. Further research needs to determine the voltage limit to avoid Ni oxidization. If tube groups are below the voltage limit, each cell within a grouping could be wired in series and each grouping could be wired in parallel. Thus, the current load for each grouping could be varied in order to maintain acceptably high cell voltages.

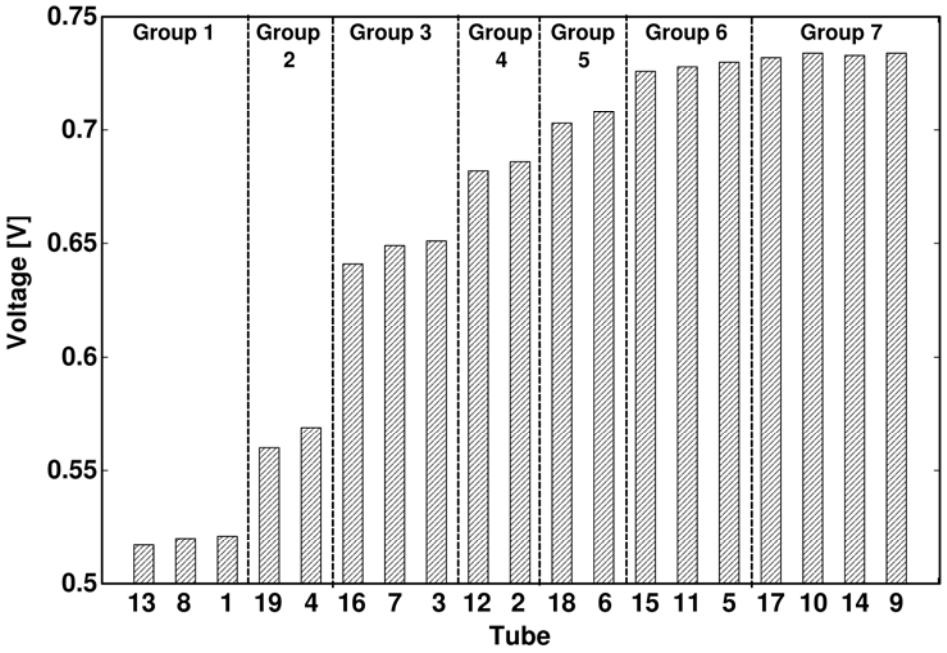

Figure 4.13 Operating voltage of every tube within bundle

4.15.2 Temperature and O_2 Axial Profiles

Area averaged axial tube temperature profiles, T(z), along with surface oxygen molar concentrations, $X_{O2}(z)$, are shown for every tube in Figure 4.14. Figure 4.14 is organized

utilizing the power groups defined in Figure 4.11. As tube power is a strong function of temperature, tube temperatures within a given power group remain within 10°C of each other. Conduction from the relatively hot CPOx region (816°C anode gas inlet) combined with high localized current density contributes to the maximum cell temperature at the anode inlet. Because air enters the cathode at a relatively cold temperature of 668°C, all tube temperatures initially decrease with increasing axial distance. Due to their close proximity to the stack can, tubes in groups 1 and 2 continue to drop in temperature with a small increase near the anode outlet due to the heat supplied by the TGC. All remaining tubes in the bundle produce enough thermal energy due to irreversibilities in the electrochemical reactions to increase their temperatures after the initial temperature decrease. The ΔT between the bundle and stack can increases in the direction of cathode and anode flow because cold oxidant enters the recuperator near the anode and cathode outlets. Radiation exchange overcomes internal tube heat generation causing temperatures to decrease at the local temperature maximum occurring approximately halfway down the length of the bundle.

Surface oxygen concentrations are dependent on bulk convective cathode mixing as well as diffusion. Oxygen diffusion from the bulk cathode to the tube surface is driven by the current produced by a tube. With the total current, 14.72 A, of each tube held constant, the sum of O_2 diffusion to the tube surface is constant for each tube. Localized current densities are directly proportional to tube temperature as seen in Figure 4.14.b. As the temperature of group 4 increases, O_2 concentration decreases at an increased rate due to a higher localized current density. O_2 concentrations are also a function of bulk convective mixing which is dependent on velocity distributions within the cathode. Because cathode gases enter at the radial periphery of the bundle combined with the quasi-radial bundle symmetry, velocity variations within the cathode are primarily a function of radial position. Tube powers were also shown to have a radial dependence which explains why O_2 concentration profiles within power groupings are very similar.

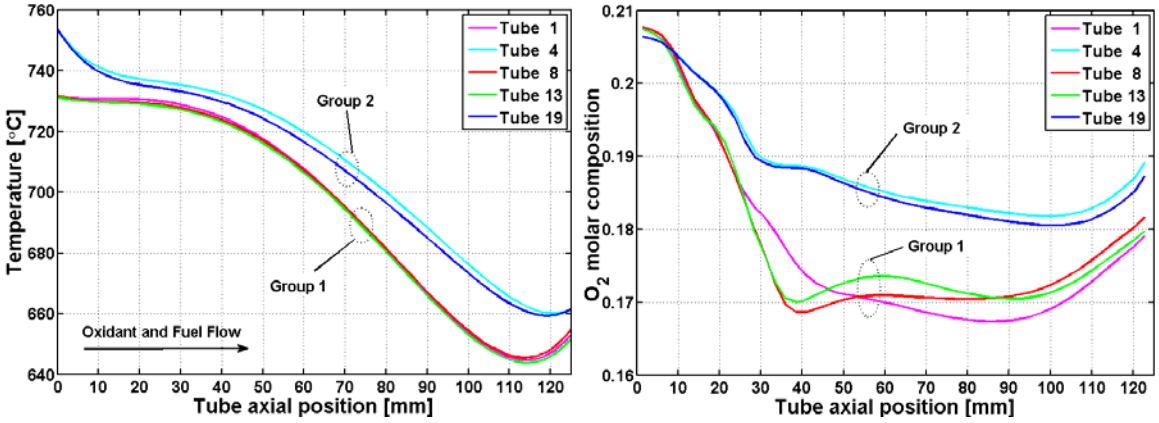

(a) Tube groupings 1 and 2

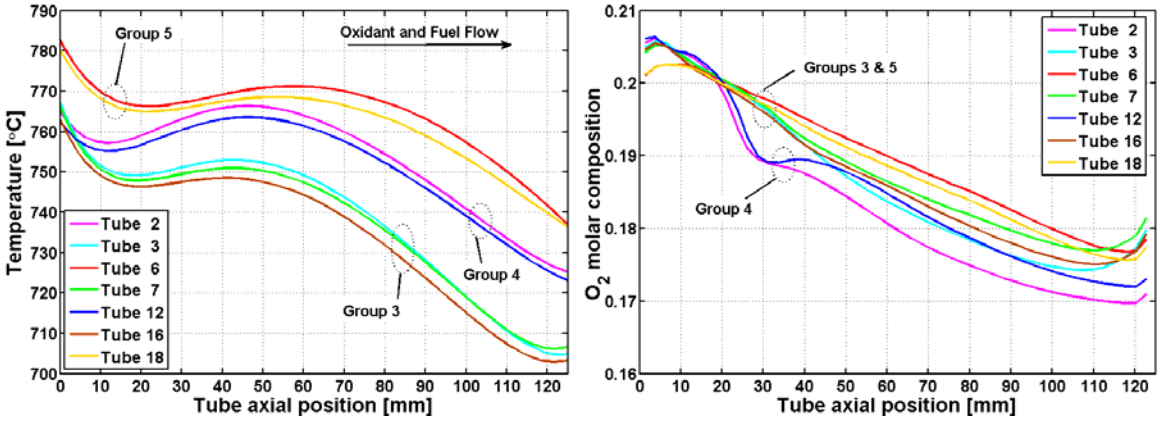

(b) Tube groupings 3, 4, and 5

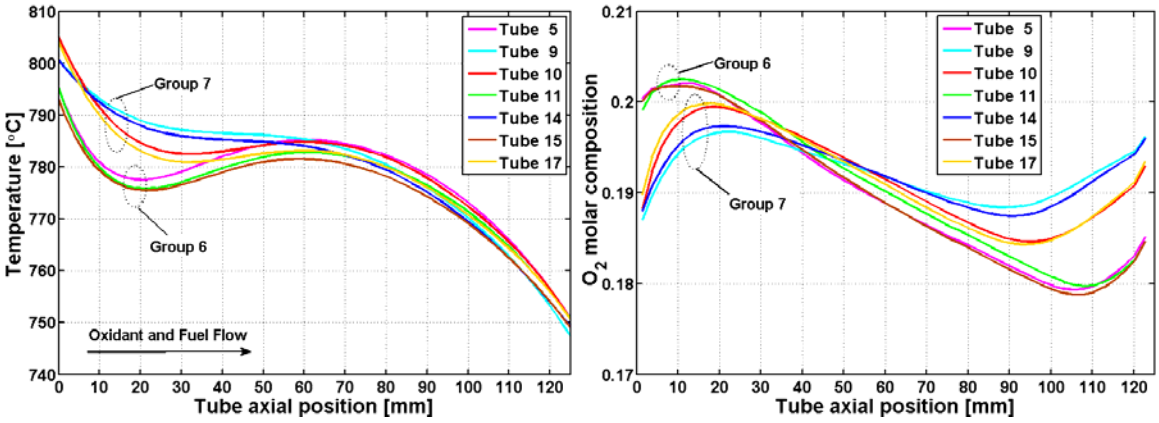

(c) Tube groupings 6 and 7

Figure 4.14 Temperature and surface oxygen molar concentration profiles of every tube in bundle. Tubes grouped based on power groupings in Figure 4.11.

4.15.3 Contours Plots and Cathode Oxidant Pathlines

Contour plots of bundle temperature and surface oxygen concentration are shown in Figure 4.15. In both figures cathode gases enter through the dark ring at the bottom of the bundle. Cathode gases flow in the positive *z*-direction and exit the bundle through concentric circle cutouts in the outlet tube-sheet. Anode fuel flow flows in the positive *z*-direction as well. Symmetric stack results are mirrored to show half of the bundle in Figure 4.15. Contours of tube temperature are shown on the left quarter with contours of surface oxygen molar concentration shown on the right quarter. Temperature contours illustrate the radiation shielding effect outer periphery tubes have on inner periphery tubes. The inner periphery ring of tubes is relatively hot with a uniform temperature distribution. Cold zones are seen at the outer periphery tubes caused by their close proximity to the stack can wall as well as by low cathode mixing. As each tube consumes the same amount of O_2 (constant cell current), low O_2 concentrations at outer periphery tubes are the result of low convective mixing not O_2 diffusion at the cathode. A further indicator of ineffective cathode mixing is demonstrated in the cathode particle pathlines colored by temperature in Figure 4.16. To reach the outer periphery tube surfaces, oxidant needs to turn 180° after entering the cathode. Pathlines indicates the majority of oxidant flows interior to the bundle with low amounts of oxidant able to overcome its initial inward radial momentum and reach the outer periphery tubes.

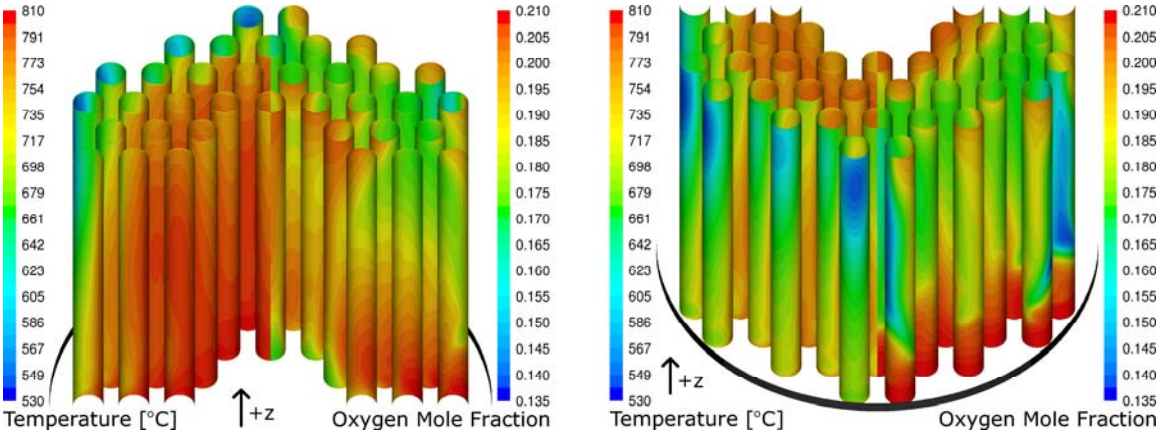

(a) Interior aspect of bundle. (b) Exterior aspect of bundle.

Figure 4.15 Contour plots of surface oxygen molar concentrations on the right quarter and tube temperatures on the left quarter.

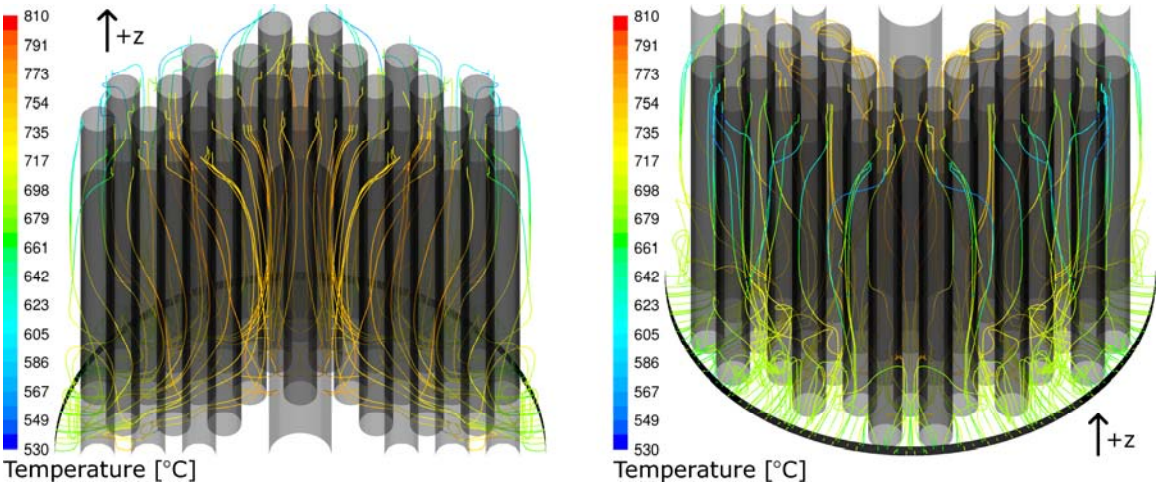

(a) Interior aspect of bundle. (b) Exterior aspect of bundle.

Figure 4.16 Pathlines with cathode colored by temperature. Tube bundle and central fuel preheat tube walls shown in black.

4.16 Summary of Findings

A powerful tubular SOFC system design and simulation tool has been developed. A detailed stack model coupling CFD to a 1-D electrochemical tubular cell model allows one to see how stack geometries affect variations in tube performance. By integrating a recuperator, tail-gas combustor, and catalytic partial oxidation reformer to the detailed stack model, thermal interactions between BoP and the SOFC stack are captured in the system level model. Model results can point fuel cell developers to more effective system architectures and optimal operating conditions with the goal of increasing system efficiencies by optimizing the thermal coupling between BoP and the SOFC stack.

The model capabilities were explored through simulation of a highly-integrated tubular SOFC system for small (~1 kW) mobile applications. The simulation predicts a fuel conversion efficiency of 21%, where 75% of the input fuel energy is convected away with the exhaust stream, and the remaining 3% lost thru heat transfer to the environment. With 75% of energy lost in the exhaust stream, model results highlight the ineffective use of a co-flow recuperator, and a counter-flow recuperator is a recommended design improvement. With ineffective preheating of oxidant, cathode gases are 148°C colder than anode gases entering the stack causing a large decrease in tube temperatures near the

cathode inlet. Unlike planar stacks, convective cooling is not the dominate mechanism for heat transfer within the stack; therefore, a large ΔT is not required of cathode gases entering the bundle.

Simulation results point to radiation heat transfer as the dominate mechanism of stack cooling within tubular stacks. Radiation accounts for 62-93% of total heat rejection from the external tube surface. The dominance of radiation leads to a strong relationship between the power output of a tube and the view factor from the tube to the relatively cold stack can wall. The bundle under study results in seven tube groupings based on similar view factors to the stack can. These seven view factor groupings correspond to seven power groupings. These groupings have impact on reduced-order modeling efforts, future research efforts will look into simulating stack performance based on tube groupings rather than the typical single tube extrapolation. This will require a unique set of thermal boundary conditions to be extracted from the detailed CFD analysis for each tube grouping.

An enormous amount of information for detailed stack design is also available from this modeling tool. Contour plots of stack temperatures reveal relatively hot and uniform tubes at the inner periphery but cold zones develop at the outer periphery of the bundle. Cathode mixing is also seen to be relatively low with low oxygen concentrations at the outer periphery, low power tubes. Non-uniformities within the stack lead to power disparities amongst cells. As cell power varies from 7.6 – 10.8 W, the current stack design leaves room for improvement. It is recommended that tubular stacks be configured such that the variation in view factors from cells to the stack surroundings is minimized. While the simulation tool was implemented for small-scale tubular SOFCs, it should be noted that the modeling approach employed is applicable to a wide range of SOFC systems.

CHAPTER 5

SENSITIVITY ANALYSIS AND PARAMETRIC STUDY

A sensitivity analysis was performed on the high-fidelity tubular system model. The goal of the sensitivity analysis is two fold. First, the analysis reveals effective tuning parameters. Tuning parameters are defined as variables within the model that can be altered in order to match model predictions to experimental data. For example, if experimentally the fuel plenum gas enters the anode channels 50°C lower than model predictions, the convective heat transfer coefficient within the fuel plenum can be 'tuned' to match experimental fuel plenum gas temperatures. By evaluating the sensitivity of system statepoints to possible tuning parameters, the most effective tuning parameters are highlighted.

Secondly, the sensitivity analysis points to the selection of effective control variables to be utilized in SOFC control strategies. SOFC system control algorithms are essential to maintain stack temperatures, suppress carbon formation, and maintain stack power during both steady-state and load-following conditions. While operating parameters such as fuel and oxidant utilization are not directly set, they can be manipulated by altering the oxidant flowrate, fuel flowrate, and operating current level which can be easily controlled with a controller unit.

The sensitivity, S_{ik}, of quantity i to variable k is given by:

$$S_{ik} = \frac{i - i_O}{i} \cdot \frac{k_O}{k - k_O} \tag{4.1}$$

where i is the new quantity as a result of using the new parameter value k. The original quantity is i_o, and k_o is the original parameter value. For each sensitivity analysis, the parameter was varied ±10% from the baseline value and the corresponding changes in quantity i were recorded. If $S_{ik} = 1$, the quantity i changed by 10% along with the 10% variation in variable k. A positive sensitivity coefficient means the quantity i is proportional to variable k. A negative sensitivity coefficient means the quantity i is inversely proportional to variable k. To quantify the resulting sensitivity coefficients, the designations shown in Eqs: (4.2-4.4) are made.

$$|S_{ik}| > 1.0 \qquad \text{Very Sensitive} \qquad (4.2)$$

$$0.1 < |S_{ik}| < 1.0 \qquad \text{Sensitive} \qquad (4.3)$$

$$|S_{ik}| < 0.1 \qquad \text{Insensitive} \qquad (4.4)$$

System operating parameters are first investigated by altering the following in order to modify the fuel and oxidant utilization within the system.

- oxidant flowrate
- fuel flowrate
- cell current

Next, system design and manufacturing specifications are investigated, including:

- cell cathode emissivity
- stack can emissivity
- insulation thickness

Finally, the sensitivity to model variables is calculated by examining:

- heat transfer coefficient in CPOx model
- heat transfer coefficient in TGC model

If it is observed that the system is sensitive to parameter k, a further exploration of the design space of parameter k is carried out with a parametric study.

5.1 Oxidant Flowrate

The first parameter studied is the magnitude of oxidant flowing into the system. In planar stacks, excess oxidant is flowed through the stack in order to maintain the stack at the desired temperature. This method is effective in planar stacks because the dominant heat transfer mechanism in the gas channels is convection. Baseline tubular system results (see Section 4.15) highlighted radiation as the dominate mechanism for cooling in tubular stacks; therefore, an excess of oxidant flow may not be required in tubular stacks.

5.1.1 Sensitivity Analysis

Sensitivity coefficients in Table 5.1 quantitatively show the effects oxidant flowrate has on a highly-integrated tubular system. Negative sensitivity coefficients explicitly state the inverse relationship between all system variables and the oxidant flowrate. For example, a 10% decrease in oxidant flowrate results in a sensitivity coefficient of -0.87 with respect to stack power which corresponds to an 8.7% increase in stack power.

Table 5.1 System Sensitivity to Oxidant Flowrate

k [kg/s]	$T_{Cathode\ Inlet}$	$T_{Anode\ Inlet}$	$T_{Recup.\ Inlet\ Hot}$	$T_{Recup.\ Outlet\ Hot}$	$T_{Exhaust}$	Stack Power	η_{sys}
-10%	-0.60	-0.38	-0.45	-0.55	-0.52	-0.87	-0.87
+10%	-0.51	-0.31	-0.36	-0.44	-0.42	-0.97	-0.98

As temperatures increase with decreased oxidant flowrate so does the system power and efficiency. One main contributor to increased stack power is hotter oxidant temperatures within the recuperator leading to a hotter stack can wall. Hotter oxidant temperatures within the recuperator are a result of an increased heat capacity ratio of exhaust to oxidant in addition to higher exhaust temperatures entering the recuperator. Both effects lead to a hotter stack can wall which lowers the driving potential of radiation exchange from the outer periphery tubes to the stack can. As expected, tubes near the outer periphery of the bundle are the most sensitive to oxidant flowrate. This is shown in Table 5.2 where the sensitivity of tube powers to oxidant flowrate is presented for every tube in the bundle. Tubes at the outer stack periphery (groups 1 and 2) are classified as

being very sensitive to oxidant flowrate. All remaining tubes are classified as sensitive to oxidant flowrate with sensitivity decreasing as tubes become closer to the bundle radial center. Tubes at the stack inner periphery (groups 6 and 7) have a limited view of the stack can which explains their lower sensitivity coefficients, but they still experience an increase in power with reduced oxidant flow because of hotter neighboring tubes and hotter cathode gases. An inverse relation to the above observations applies when oxidant flow is increased.

Table 5.2 Tube Power Sensitivity to Oxidant Flowrate

Tube Group	Tube Number	S_{ik} -10%	S_{ik} +10%
1	13	-1.90	-1.89
	8	-1.88	-1.88
	1	-1.88	-1.90
2	19	-1.57	-1.62
	4	-1.52	-1.61
3	16	-0.99	-1.09
	7	-0.94	-1.07
	3	-0.92	-1.03
4	12	-0.71	-0.81
	2	-0.68	-0.80
5	18	-0.61	-0.73
	6	-0.58	-0.72
6	15	-0.47	-0.59
	11	-0.46	-0.59
	5	-0.45	-0.58
7	17	-0.45	-0.58
	10	-0.44	-0.57
	14	-0.44	-0.58
	9	-0.44	-0.58

Oxidant flowrate is seen to be a very effective operating parameter in driving stack temperature and power output. The largest effect is seen at outer periphery tubes where a

10% reduction in oxidant flowrate results in a sensitivity of -1.90 and -1.52 corresponding to an increase in tube power of 19% and 15% at tubes 13 and 4, respectively. It is only with a thermally coupled system model that the effect between the recuperator and the stack is captured.

With the high level of sensitivity to oxidant flowrate, a parametric study is warranted in which oxidant flow is further decreased. However, while simulations were attempted at lower oxidant flowrates, the CFD model would not converge; therefore, a parametric study is not presented.

5.2 Fuel Flowrate

The baseline simulation resulted in a relatively low fuel utilization of U_F = 56%. The remaining 44% of fuel entering the stack is converted to thermal energy within the TGC. The magnitude of thermal energy leaving the TGC and entering the recuperator dictates the extent of oxidant preheating prior to entering the cathode. Thermal energy not exploited in preheating oxidant is convected out of the system in the exhaust stream. Ideally, fuel utilization is maximized such that the magnitude of thermal energy released in the TGC is sufficient to preheat the oxidant to a level where stack power decreases are offset by the decrease in fuel input into the system. Conventional system operating strategies would suggest decreasing fuel flow in order to increase fuel utilization and consequently increasing overall system efficiency. As described in Section 5.1, stack performance is highly sensitive to temperatures within the recuperator. Thus, conventional operating strategies may not prove adequate.

5.2.1 Sensitivity Analysis

By lowering the fuel flowrate while maintaining a constant current, fuel utilization is increased. This approach tests the effectiveness of the recuperator because the exhaust gas will now enter the recuperator with a lower thermal capacitance. The extent of oxidant preheating will decrease, but an effective recuperator will tend to dampen the

decline in oxidant preheating. The sensitivity of system operating conditions to fuel flowrate is shown in Table 5.3. In this analysis the flowrate of air entering the system with fuel is varied to maintain a constant O/C ratio of 1.1 used in the baseline study.

Table 5.3 System Sensitivity to Fuel Flowrate

k [kg/s]	$T_{Cathode\ Inlet}$	$T_{Anode\ Inlet}$	$T_{Recup.\ Inlet\ Hot}$	$T_{Recup.\ Outlet\ Hot}$	$T_{Exhaust}$	Stack Power	η_{sys}
-10%	0.69	0.54	0.94	0.75	0.69	1.37	0.41
+10%	0.74	0.53	0.98	0.80	0.72	1.11	0.10

Fuel utilization increases to 62.6% (up 6.6% from the baseline) accompanying the 10% decrease in fuel flowrate. The decrease in thermal energy leaving the TGC has a dramatic effect on the performance of the recuperator. The hot exhaust temperature entering the recuperator has a sensitivity coefficient of 0.94 which translates into a 9.4% decrease (82°C) in temperature associated with the 10% decrease in fuel flowrate. Combined with the lower heat capacity of the exhaust stream, oxidant is preheated to a temperature 46°C colder than the baseline simulation. A cooler oxidant within the recuperator leads to a cooler stack can wall increasing the driving potential for radiation exchange from the tube bundle to the stack can. The resulting cooler cells cause stack power to decrease. Stack power is seen to be highly sensitive to fuel flowrate. System efficiency is most with a sensitivity coefficient of 1.37 corresponding to a 13.7% decrease in efficiency as a result of the 10% decrease in fuel flowrate. An inverse relationship develops between system efficiency and fuel utilization when the later is controlled with fuel flowrate. This is a non-intuitive result which is only captured with a thermally coupled system model.

Opposite trends are seen when the fuel flowrate is increased. Interestingly, the system efficiency increases by 1% with a 10% increase in fuel flowrate. At the higher fuel flowrate condition, the increase in stack power slightly outweighs the increase in added fuel energy. Simulation results suggest a higher power density along with increased efficiency can be achieved by increasing the fuel flowrate, but temperatures

within the TGC and CPOx reformer limit the amount of excess fuel as discussed in the following parametric study.

5.2.2 Parametric Study

An increase in stack power and system efficiency was seen with increasing the fuel flowrate by 10% in the sensitivity analysis above. To further explore this effect, fuel flowrate is increased up to 140% of the baseline flowrate as shown in Figure 5.1. The maximum efficiency, 21.5%, occurs at approximately 108% of the baseline fuel flowrate. Efficiency remains relatively close to the maximum as fuel flow is varied ±10% from the 108% optimal. Efficiency begins to decrease more dramatically past this region, as efficiency drops below 19% (a 12% decrease from maximum) at 140% fuel flow.

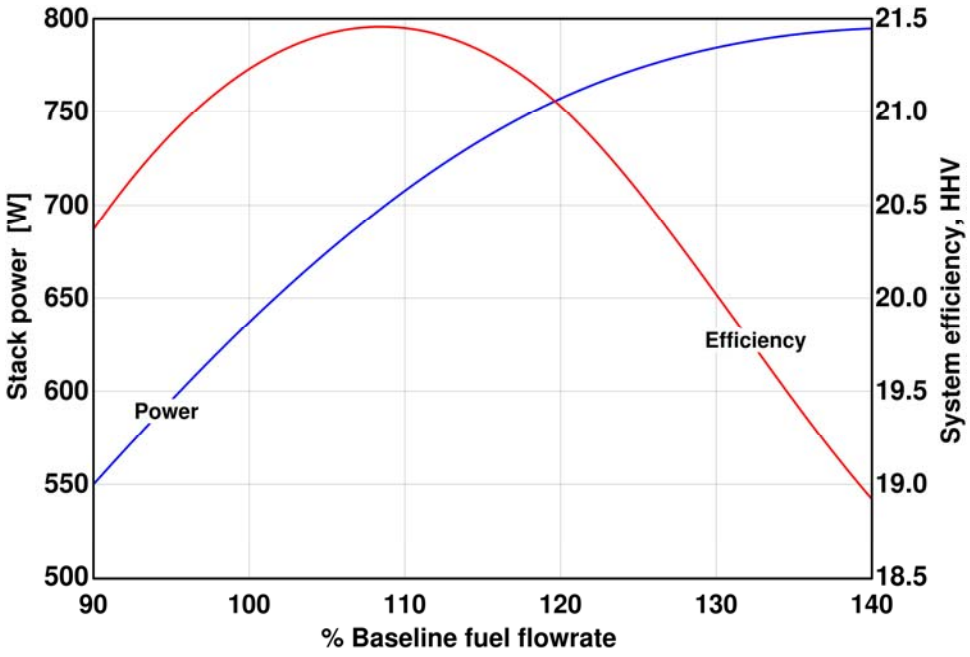

Figure 5.1 Parametric study varying fuel flowrate

Stack power on the other hand continuously increases over the range of fuel flow studied. The rate at which stack power increases does decrease as fuel flow increases with a maximum occurring slightly above 140%. With the dramatic decrease in efficiency, fuel flow was not increased passed 140% baseline. There are other system constraints that must be monitored when increasing the fuel flowrate particularly

temperatures in/around the CPOx reformer and TGC. The temperature of reformate leaving the CPOx reformer ranges from 1218°C to 1270°C at fuel flows of 100% to 140% the baseline, respectively. Both cathode and anode exhaust temperatures increase with increased fuel flowrate. Thus, TGC exhaust temperatures are highly sensitive to fuel flowrate ranging from 999°C to 1419°C at fuel flows of 100% to 140% the baseline, respectively. Because of high TGC exhaust temperatures, fuel flow should not be increased past 110% of the baseline which results in a 1101°C TGC exhaust temperature.

Choosing the optimal fuel flowrate for this system needs to take into account the intended application as both efficiency and power density are both tied to the overall size of the system. Higher system efficiencies require less fuel to be stored/supplied to operate over the desired mission duration. A higher stack power density requires fewer cells to produce the required power output. For applications where size is the key design metric, a balance between the size of the stack and the fuel storage must be made. This adds complexity to the design as fuel storage must now be included in the system model.

5.3 Cell Current

With all cells connected in electrical series, each cell within the bundle operates at a common current. The current drawn from the stack is controlled by the power electronics. As discussed in Section 1.1.1, stack efficiency continually decreases as current increases because of increasing overpotentials within the cells. However, the power density increases with increasing current until a maximum power density is reached. Generally and in the baseline simulation, SOFCs operate at the lower current density side of peak power density. While stack efficiency decreases with increased current, the overall system efficiency generally increases. System efficiency is generally proportional to fuel utilization which increases along with current, but the relationship between system efficiency and fuel utilization can be altered when the system is highly integrated. Section 5.2 altered fuel utilization by varying the fuel flowrate. Surprisingly, a higher fuel utilization resulted in decreased system efficiency due to the thermal coupling between the stack and the recuperator. The following analysis reveals whether

altering fuel flowrate or cell current is the most effective strategy to control fuel utilization.

5.3.1 Sensitivity Analysis

Table 5.4 shows the sensitivity of the highly-integrated system to a change in operating current.

Table 5.4 System Sensitivity to Cell Current

k [A]	$T_{Cathode\ Inlet}$	$T_{Anode\ Inlet}$	$T_{Recup.\ Inlet\ Hot}$	$T_{Recup.\ Outlet\ Hot}$	$T_{Exhaust}$	Stack Power	η_{sys}
-10%	-0.14	-0.05	-0.39	-0.20	-0.16	0.60	0.60
+10%	-0.13	-0.05	-0.38	-0.19	-0.15	0.56	0.56

Stack power and system efficiency are seen to be the most sensitive to operating current. A higher current demand, i.e. increased fuel utilization, results in a higher system efficiency. Conversely, a lower current demand results in a decrease in system efficiency as more unspent fuel enters the TGC. With increased fuel entering the TGC, higher temperatures are seen in the recuperator when operating at lower current demands. At the other end, a higher current leads to lower temperatures in the recuperator.

It is seen that recuperator temperatures are not as sensitive to current levels as are the power and system efficiency. This is due to the integration of the stack and the recuperator in this system design. Recall that the stack can wall separates cathode gases from oxidant flow in the recuperator. At lower currents, the magnitude of irreversibilities within the cells is lower; therefore, the cells have less thermal energy to transport resulting in lower temperature cells. With more thermal energy entering the recuperator from the TGC, there is a lower driving potential for radiation heat transfer from the cells to the stack can wall. The opposite is true at higher current demands. Irreversiblities in the cells increase resulting in increased cell temperatures. Less thermal energy enters the recuperator leading to an increase in the ΔT radiation driving potential between the cells and the stack can wall. The integrated system design acts to regulate temperatures within

the system in response to changes in current. A self-regulating system allows for simplified operating strategies as current can be varied without the need to simultaneously vary other system parameters in order to maintain system temperatures.

Stack power and system efficiency should increase until the maximum power density is reached. To identify the stack current which produces maximum power density, the following parametric study is performed.

5.3.2 Parametric Study

The stack power curve as given in Figure 5.2 has the same relationship to current density as seen at the cell level. Stack power increases with current density until a peak is reached after which stack power decreases as concentration overpotentials begin to substantially limit cell voltage.

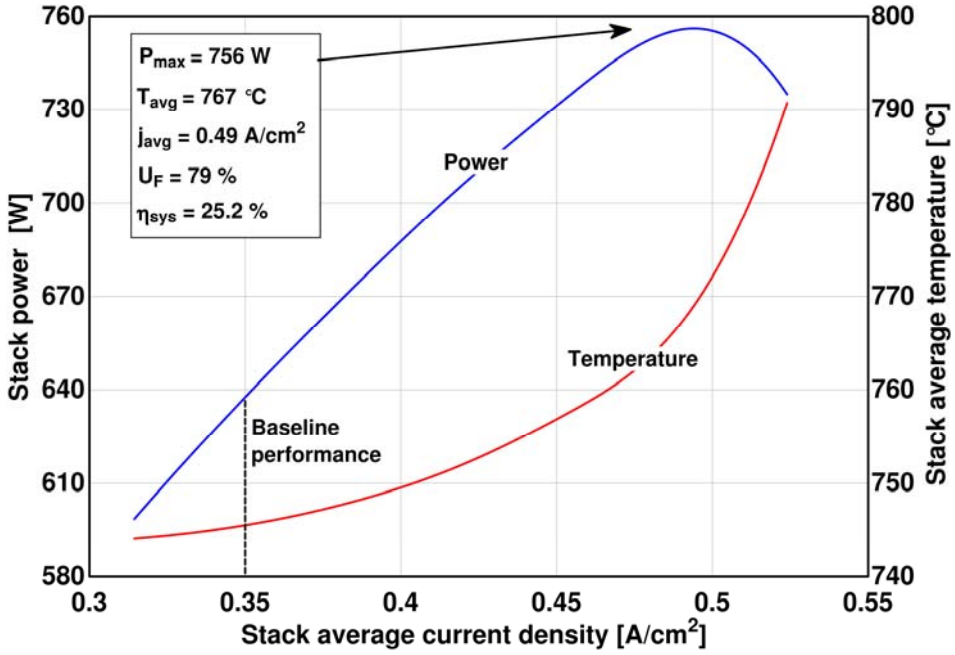

Figure 5.2 Parametric study performed on cell current

Figure 5.2 shows a maximum stack power of 756 W occurring at a current density of 0.49 A/cm^2. Stack power peaks at the same current density as a single cell operating at the stack average temperature, 767°C. Also plotted is the average stack temperature,

which increases with current density as more irreversible heat generation in the cell needs to be transferred out of the stack. Fuel utilization is linearly dependent on stack current in this parametric study ranging from 51% to 85% at the lower and upper limits of current density, respectively.

5.3.3 Fuel Utilization Control

Effective control variables can be extracted from the results of the sensitivity and parametric studies. It is often desirable to operate SOFCs at higher fuel utilizations, > 70%, in order to reduce temperature spikes in the TGC, reduce fuel storage requirements, and increase system efficiency. While fuel utilization is not directly controllable, varying the fuel flowrate and/or cell current demand allows the fuel utilization to be altered.

Simulation results highlight current demand as the most effective method to indirectly control fuel utilization. Current control is effective for two main reasons. First, the integrated system design acts to dampen any temperature spikes with variations in stack current. Secondly, fuel utilization is proportional to system efficiency when varying the stack current. Also, stack power is related to current density in the same manner as cell power. Since V-j curves for cells are well known, calculating a current demand set point near the peak power density is relatively straightforward if the stack temperature is known.

Varying fuel flowrate is not an effective method of fuel utilization control. Section 5.2 showed that system efficiency and fuel utilization are inversely proportional when varying fuel flowrate. While a lower fuel utilization resulted in a slight increase in system efficiency, increased fuel in the CPOx and TGC present challenges in temperature control. Secondly, increased fuel flows will require larger fuel storage tanks lowering the power density of the system.

5.4 Tube Cathode Emissivity

Reference values for emissivity of YSZ-LSM cathodes are very limited in fuel cell literature. The baseline simulation imposed $\varepsilon = 0.8$ on all tubes. This value is near cathode emissivities used in prior journal publications as discussed in Section 4.4.2, but emissivity values are from modeling papers not explicit measurements of cathode emissivity. The emissivity of a material is also highly dependent on the manufacturing process and how the material is treated in the manufacturing process. With proprietary fuel cell manufacturing techniques used across all developers, no single measured emissivity value will apply to all fuel cells in development.

5.4.1 Sensitivity Analysis

Because of the difficult nature in calculating a precise emissivity value, the sensitivity of the system to the cathode emissivity is carried out. The resulting sensitivity analysis is summarized in Table 5.5. System statepoints and performance are all seen to be insensitive to cathode emissivity near the baseline of 0.8. With the non-linearities in radiation heat transfer, cathode emissivity is further explored as the linear relationship shown in Table 5.5 is not likely to hold true for a large range of emissivity values. Cathode emissivity is varied from 0.2 – 0.88 in the parametric study.

Table 5.5 System Sensitivity to Tube Emissivity

k [-]	$T_{Cathode\ Inlet}$	$T_{Anode\ Inlet}$	$T_{Recup.\ Inlet\ Hot}$	$T_{Recup.\ Outlet\ Hot}$	$T_{Exhaust}$	Stack Power	η_{sys}
-10%	0.01	0.02	0.00	0.01	0.01	-0.02	-0.03
+10%	0.01	0.00	0.00	0.00	0.00	-0.02	-0.01

5.4.2 Parametric Study

The results of the parametric study are shown in Figure 5.3. As tube emissivity affects radiation heat transfer to the stack can wall, i.e. recuperator, the cathode inlet temperature is plotted along with stack power. A non-linear relationship to cathode emissivity is observed for both the stack power and cathode inlet temperature. Their

sensitivity to cathode emissivity increases as the emissivity is lowered. Overall, sensitivity remains relatively low as stack power and cathode inlet temperature only change 2.6% and 1.2%, respectively, when cathode emissivity is decreased from 0.5 to 0.2.

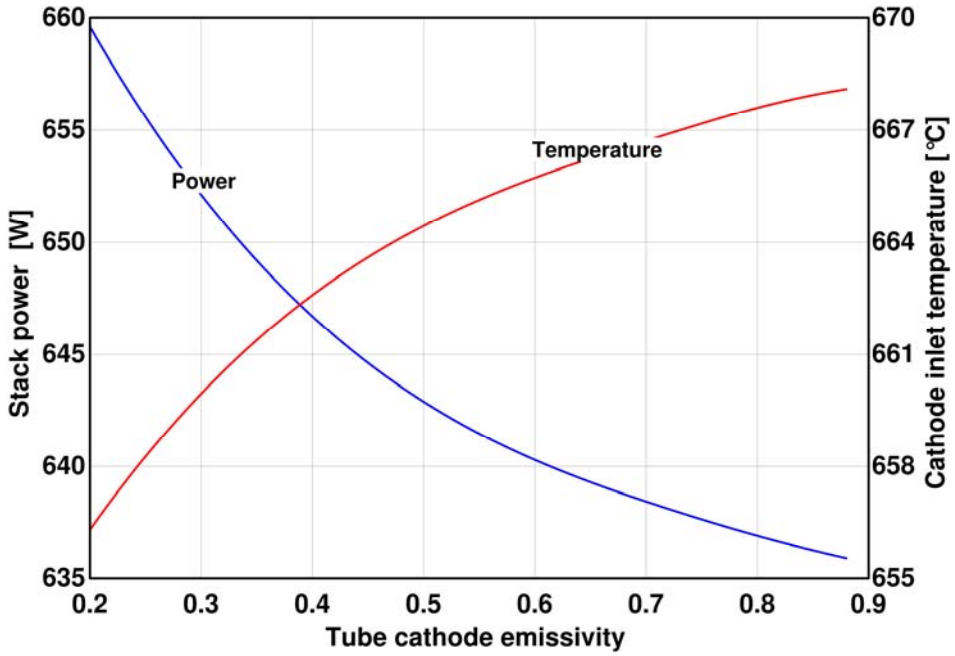

Figure 5.3 Parametric study varying emissivity at cathode external surface of the cell

5.5 Stack Can Emissivity

Because of the strong relationship between the power output of a tube and its view factor to the stack can, the sensitivity to the emissivity at the inner surface of the stack can wall is explored. The inner surface of the stack can is the side that is 'seen' by tubes with respect to radiation transport. The emissivity can be altered through the manufacturing process, i.e. a polished can would result in a decreased emissivity while a sandblasted surface would result in a higher emissivity. This sensitivity analysis points towards the type of finish that should be applied. Ultimately, economic trade-offs will need to be taken into account with any manufacturing process change.

5.5.1 Sensitivity Analysis

The resulting sensitivity analysis on the stack can emissivity is summarized in Table 5.6. System statepoints and performance are all observed to be insensitive to the stack can emissivity near the baseline of 0.9. As with the effect of cathode emissivity, the linear relationships seen in Table 5.6 will likely not hold because of the non-linearities in radiation heat transfer. In order to capture the effect of non-linearities, a larger range of stack can emissivity values is explored in a parametric study.

Table 5.6 System Sensitivity to Stack Can Emissivity

k [-]	$T_{Cathode\ Inlet}$	$T_{Anode\ Inlet}$	$T_{Recup.\ Inlet\ Hot}$	$T_{Recup.\ Outlet\ Hot}$	$T_{Exhaust}$	Stack Power	η_{sys}
-10%	0.03	0.01	-0.02	0.02	0.01	-0.03	-0.03
+10%	0.02	0.00	-0.02	0.01	0.01	-0.03	-0.01

5.5.2 Parametric Study

The emissivity of the inner surface of the stack can is varied from 0.2 – 0.99 in this parametric study with results shown in Figure 5.4. Both stack power and cathode inlet temperature are plotted against stack can emissivity. A similar trend as with cathode emissivity is seen. Both power and cathode inlet temperature are more sensitive at lower stack can emissivities, $\varepsilon < 0.5$, than at higher emissivities, $\varepsilon > 0.6$. Although, neither power or cathode inlet temperature are very sensitive to stack can emissivity. Stack power and cathode inlet temperature change by 3.3% and 2.4%, respectively, when varying stack can emissivity from 0.5 to 0.2.

If economical, the inner wall of the stack can could be polished, lowering the emissivity in order to increase stack power. This parametric study provides a metric to compare added cost of manufacturing to increased system performance. This information would not be captured in a stand-alone stack model as the stack can is highly-integrated with the recuperator; therefore, a thermally coupled system model is required to drive system design modifications.

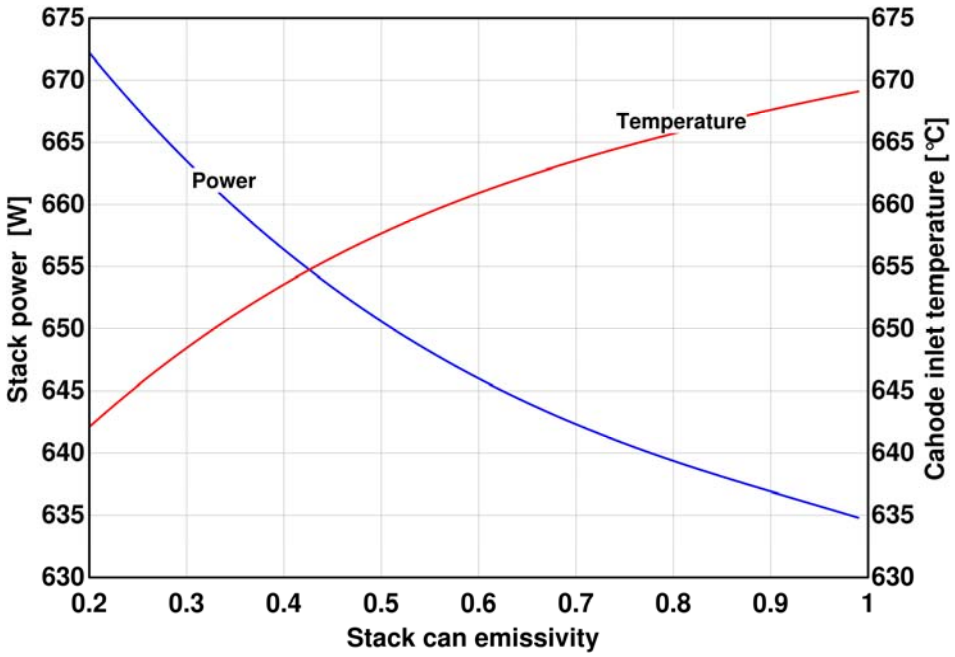

Figure 5.4 Parametric study varying emissivity at the inner surface of the stack can. This is one of the surfaces encapsulating cathode gases.

5.6 Insulation Thickness

Insulation is wrapped around the system to hinder the transfer of thermal energy out of the system. Any thermal energy transferred via conduction through the insulation is wasted and will lower the efficiency of the system. While thicker insulation will lower heat loss to the surroundings, it comes at the expense of a larger system and increased material costs. The baseline simulation resulted in 94 W of thermal energy being conducted out of the system. At only 3.1% of energy entering the system, insulation heat loss is sufficiently small utilizing the baseline insulation thickness.

5.6.1 Sensitivity Analysis

A sensitivity analysis, Table 5.7, illustrates the effect of varying the insulation thickness surrounding the system.

Table 5.7 System Sensitivity to Insulation Thickness

k [mm]	$T_{Cathode\ Inlet}$	$T_{Anode\ Inlet}$	$T_{Recup.\ Inlet\ Hot}$	$T_{Recup.\ Outlet\ Hot}$	$T_{Exhaust}$	Stack Power	η_{sys}
-10%	0.03	0.02	0.00	0.03	0.03	0.04	0.04
+10%	0.02	0.02	-0.01	0.02	0.03	0.04	0.04

All system statepoints and performance metrics are seen to be insensitive to insulation thickness around the baseline thickness. This result points to the baseline insulation thickness as being over-sized as a decrease in thickness has little effect on the system. It can be concluded that the insulation represents the dominant thermal resistance within the system for all insulation thicknesses explored. As insulation thickness is decreased further, a transition point occurs where insulation resistance no longer dominates leading to increased system sensitivity to insulation thickness. If system power density (or cost) is a key design metric, insulation needs to be sized slightly larger than the transition point. On the other hand, over-sizing insulation can aid in control as the heat rejected to the surroundings will be insensitive to operating conditions. The following parametric study locates the transition point where system operating conditions become sensitive to insulation thickness.

5.6.2 Parametric Study

Figure 5.5 depicts the relationship between stack power and insulation heat loss as a function of the insulation thickness around the system. Highlighted are the three sensitivity regions. Stack power remains relatively unchanged as insulation is decreased to 60% of the baseline thickness. A transition region occurs where stack power and insulation heat loss become sensitive to insulation thicknesses ranging from 25-60% of the baseline value. Insulation no longer represents a significant thermal resistance at thicknesses below 25% of the baseline as stack power drops significantly with additional reductions in insulation thickness. Operating at the junction of the transition and insensitive region would result in the thinnest insulation without a significant impact to stack power.

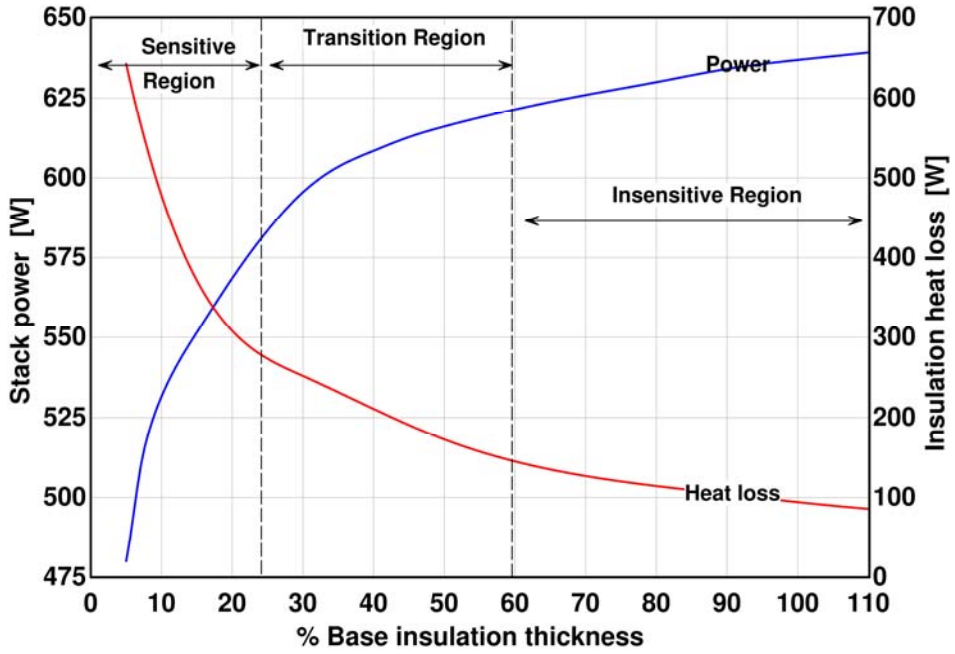

Figure 5.5 Parametric study varying insulation thickness around system

5.7 CPOx and TGC Models Heat Transfer Coefficient

As discussed in Section 4.7.1, a common heat transfer coefficient of 100 W/m^2-K is utilized throughout the CPOx and TGC thermal resistance models. An exception is the heat transfer coefficients used within the fuel/air and air tube flows within the TGC domain. The common heat transfer coefficient is higher than predicted by a convective heat transfer correlation in an attempt to capture radiation exchange without the added complexity of non-linear temperature differences. As there is some level of uncertainty in the chosen heat transfer coefficient, a sensitivity analysis quantifies the effect of the heat transfer coefficient on system performance. The common heat transfer coefficient is first varied in the CPOx model, Table 5.8, followed by varying the heat transfer coefficient in the TGC model, Table 5.9.

Table 5.8 System Sensitivity to Heat Transfer Coefficient in CPOx Model

k [W/m^2-K]	$T_{Cathode\ Inlet}$	$T_{Anode\ Inlet}$	$T_{Recup.\ Inlet\ Hot}$	$T_{Recup.\ Outlet\ Hot}$	$T_{Exhaust}$	Stack Power	η_{sys}
-10%	-0.01	-0.09	-0.01	-0.01	0.01	-0.04	-0.03
+10%	-0.01	-0.10	-0.01	-0.01	0.01	-0.04	-0.04

Table 5.9 System Sensitivity to Heat Transfer Coefficient in TGC Model

k [W/m^2-K]	$T_{Cathode\ Inlet}$	$T_{Anode\ Inlet}$	$T_{Recup.\ Inlet\ Hot}$	$T_{Recup.\ Outlet\ Hot}$	$T_{Exhaust}$	Stack Power	η_{sys}
-10%	0.00	0.01	-0.01	0.00	0.00	0.00	0.00
+10%	0.00	0.00	-0.01	0.00	0.00	0.00	0.00

System statepoints and performance metrics are seen to have little or no sensitivity to the heat transfer coefficient in the TGC model. Sensitivity coefficients for the CPOx heat transfer coefficient are all very low with no quantity changing by more than 1% with the 10% change in heat transfer coefficient. The insulation wrapped around the models presents a large thermal resistance compared to any other resistance within the models. Varying the heat transfer coefficients within the domain has little effect on the total heat transfer out of the model; therefore, the temperature distribution within the models remains fairly constant. If less insulation is wrapped around the CPOx or TGC regions, a greater impact on the choice of heat transfer coefficient would be expected.

5.8 System Design/Parameter Recommendations

Results from the sensitivity analyses and parametric studies can guide fuel cell developers towards optimizing operating parameters and system designs. Figure 5.6 acts as an SOFC system performance chart depicting the relationship of stack power to system parameters and design. In this study, a single parameter is varied with all other parameters fixed at the baseline value. Interactions between variables are not captured, but a more detailed design of experiments could be implemented in which all combinations of parameters are simulated. In the single parameter variation study, air flowrate, fuel flowrate, and stack current are the largest control variables in determining stack power output. An increase in stack power by varying air flow or current will always lead to an increase in system efficiency, but system efficiency decreases with fuel flows above 108% of the baseline (as discussed in Section 5.2.2).

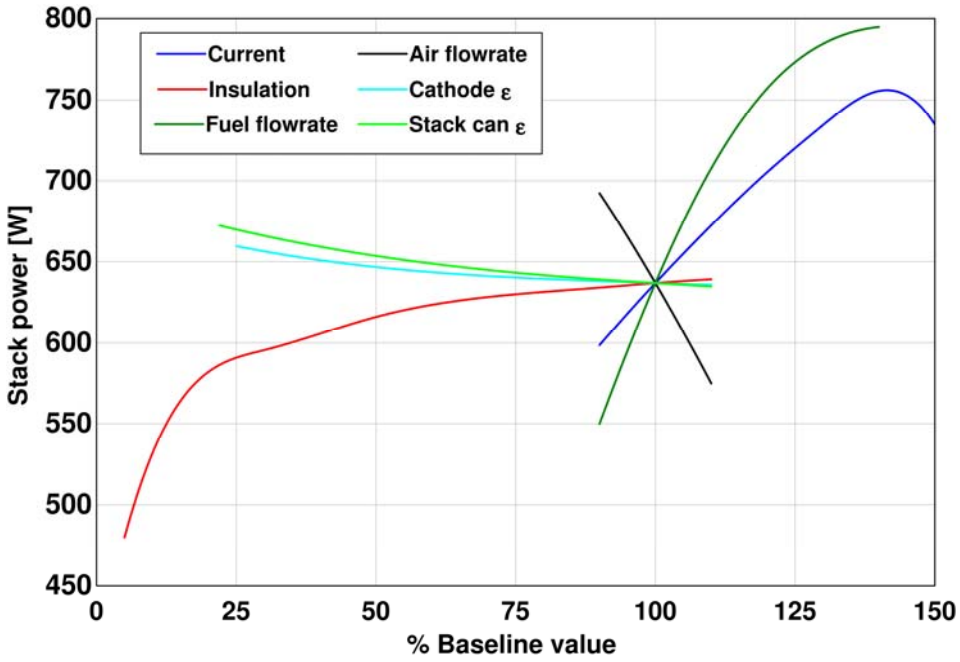

Figure 5.6 Stack power over range of operating/design variables

On the surface, increased power and efficiency are beneficial to the system, but conditions within the stack need to be investigated to ensure operating limits are not being exceeded. The baseline simulation showed variations amongst cells within the stack, but ideally all cells would be at the same operating condition. Baseline conditions resulted in a 32.2°C standard deviation with respect to the average cell temperatures. The variance in cell temperatures is altered with changes to operating conditions and emissivities as shown in Figure 5.7. Along with an increase in stack power, a beneficial decrease in cell temperature disparities results from lower emissivities in the stack. Cell temperatures become more uniform as the large radiation driving potential at outer periphery tubes is reduced. Increasing the fuel flowrate also produces more uniform cell temperatures, but excess fuel above 110% of the baseline results in large temperature spikes in the TGC. Increased stack power is also realized by increasing the current demand, but increased current is accompanied by an increase in temperature variations amongst cells. Lastly, temperature variations remain relatively unchanged when the air flowrate is altered.

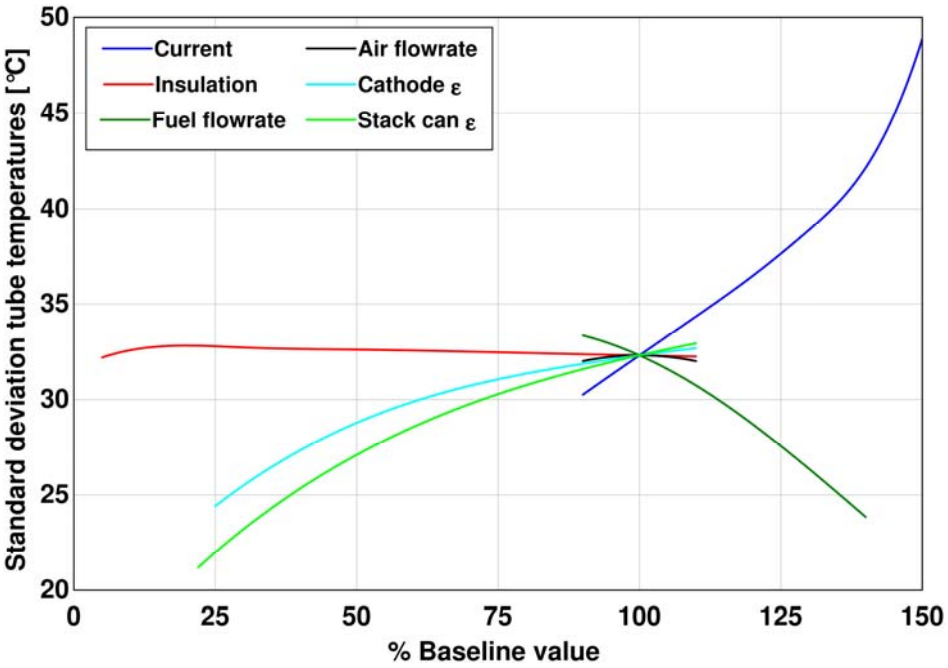

Figure 5.7 Standard deviation of tube average temperatures over range of operating/design variables

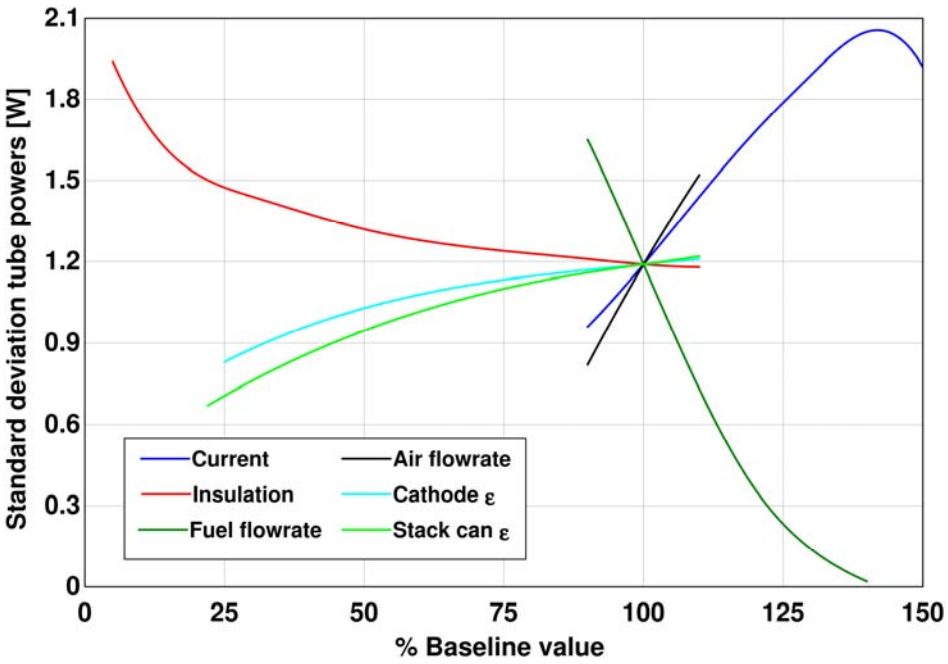

Figure 5.8 Standard deviation of tube powers over range of operating/design variables

Figure 5.8 depicts the effects of parameter variations on the standard deviation of tube powers within the stack. Stack power variations are similar to temperature variations for all parameters except for insulation thickness. While temperature variations remain

relatively uniform over the range of insulation thicknesses, each cell operates at a different location on the V-I curve as insulation thickness is varied. Non-linearities in the V-I curve are the cause for the increase in tube power variations within the stack as insulation thickness is decreased.

With radiation found to be the dominate heat transfer mechanism at baseline conditions, it is important to investigate the effect of emissivity values on the role of radiation within the stack. Figure 5.9 shows the effect of varying the stack can and cathode emissivity on the distribution of radiation and convective heat transfer from the cathode surface of the cells. With stack power slightly more sensitive to stack can emissivity, heat transfer mechanisms are also slightly more sensitive to the stack can emissivity than the cathode emissivity. Radiation remains the dominate heat transfer mechanism, >55% of total heat transfer, over the range of emissivity values. Because of the high operating temperatures and the small, enclosed stack geometry, radiation will always be a significant stack cooling method even if low emissivity value materials are utilized.

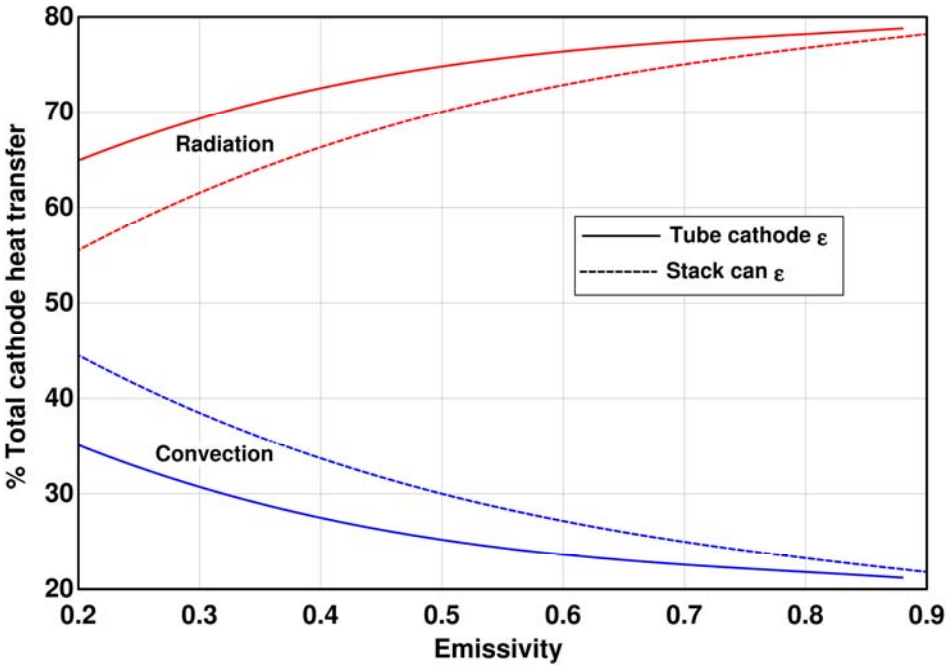

Figure 5.9 Heat transfer mechanisms from tube cathodes as a function of cathode and stack can emissivity

CHAPTER 6

CONCLUSION

Solid oxide fuel cells are a promising technology in the increasing effort to produce clean, efficient energy. High system efficiencies, 40-45% HHV, coupled with higher power densities make SOFCs attractive over conventional battery technologies for small-scale power applications including unmanned vehicles and portable power. Additionally, high efficiencies combined with the ability to operate on diesel fuel leads to the potential use as auxiliary power units where conventionally a large diesel engine is operated inefficiently at part load. While high efficiencies and power densities are possible with SOFCs, they are only realized when a complete SOFC system is effectively thermally integrated. Several thermal sinks and sources of energy exist within SOFC systems and effective coupling is required to reduce excess fuel supplied to the system solely for preheating gas streams.

A successful SOFC design begins with modeling efforts that point to effective thermally integrated designs and appropriate operating conditions. SOFC system models need to capture the thermal coupling between system components, but system models presented in the literature do not address thermal coupling. To address the inadequacy in current system models, two thermally coupled system models were created. Distinct system models were created to thermally couple two distinct system architectures, a planar SOFC system with discrete components and a highly-integrated tubular SOFC system. The highly-integrated system requires use of CFD to capture thermofluidic interactions between components whereas a lower-order thermal resistance network captures thermal interactions between spatially separated components in the discrete system.

Both thermally coupled system models are able to capture the thermal interactions occurring in and around the SOFC stack. Thermally coupled stack models reveal convective cooling is not the sole method to transport the irreversible heat produced within the stack. In the planar system, heat loss through stack insulation lowers the magnitude of excess oxidant required to flow through the stack. Radiation and convection within the gas manifolds of planar stacks also provide an effective means to preheat oxidant prior to entering the cathode channels. These planar system results lead to a lower heat duty within the recuperator and smaller oxidant storage requirements. In the tubular system, radiation is observed to be the dominate heat transfer mechanism within the stack. Thus, tubular stacks are not dependent on convective stack cooling and ancillary blower power is reduced. Significant variations in cell performance occur because radiation view factors to the walls surrounding the stack are not uniform. Consequently, cells with similar radiation view factors also have similar cell performance. This is significant as it gives tubular stack developers insight into stack performance variations simply based on stack geometry. Planar stacks hold an advantage as they are less susceptible to performance disparities.

Beyond revealing heat transfer mechanisms within the SOFC stack, the thermally coupled system models point to effective operating parameters and system designs. In the planar system, recuperator exhaust gas can be circulated within the system enclosure to provide an additional thermal sink to the stack and further reduce stack oxidant requirements. In the highly-integrated tubular system, stack performance is highly coupled to the temperature distribution within the recuperator as the two components share a common wall. Simulation results point to the co-flow recuperator as a poor configuration, and SOFC developers would be able to evaluate the performance increase of a counter-flow recuperator with the system modeling tool. Finally, the highly-integrated system model reveals effective control variables. For example, fuel utilization is effectively increased by increasing the current demand whereas decreasing the fuel flowrate is ineffective because it is accompanied by a decrease in system efficiency.

It is evident from the foregoing analyses that thermal coupling exists between components in small-scale SOFC systems. Thermally coupled system models are a critical step in ultimately creating efficient SOFC systems able to meet the increasing demand for cleaner, high efficiency energy sources.

6.0 Recommendations for Future Work

While much has been accomplished with respect to developing high-fidelity modeling tools and approaches for SOFC systems, some work remains. For planar SOFC systems, the next step is to model the gas cavity between system components and the enclosure wall with a CFD model. A CFD model would capture the details of cavity gas circulation and calculate convective heat transfer coefficients along with radiation view factors between components. Detailed CFD results would allow validation of the lower dimensional thermal resistance model approach.

While performance trends can be extracted, the high-fidelity tubular system model needs to be validated against experimental data before optimal operating parameters can be extracted. Experimental data that is both useful and feasible to measure includes the temperatures of (i) oxidant entering the cathode, (ii) fuel/air entering the reformer, (iii) TGC exhaust entering and leaving the recuperator, (iv) exhaust leaving the system, and (v) the insulation skin temperature. Finally, cell operating voltages could be measured where the predicted tube groupings would guide developers as to which cells to probe.

The impact of simplifying assumptions within the tubular system model should also be investigated. First, fuel is assumed to perfectly uniform at the anode entrance to all cells, but uneven distributions within the fuel plenum and pressure variations in the mixing region of the TGC will lead to uneven fuel flows within the cells. The effectiveness of the fuel plenum geometry can be captured by extending the CFD domain to include the fuel plenum region. In addition to the fuel plenum, the CFD domain needs to be extended to the mixing region in order to capture pressure variations between the anode outlets. Lastly, while the current stack model captures the effect of stack design on

thermal interactions, the effect of stack design on cell interconnects and associated ohmic losses are not captured. By integrating cell interconnects into the tubular model, a more complete stack development tool would be created. This also allows a thorough investigation of wiring each tube within a grouping in series and wiring the groups together in parallel. Thus, current demand is varied amongst tube groupings as a method to achieving uniform cell voltages.

Finally, computationally efficient reduced-order tubular stack models can be created with insight from the high-fidelity model. It is envisioned that the reduced-order stack model will include the anode flow, solid cells, cathode flow, and the walls surrounding the tube bundle. The 1-D tube model is computationally efficient and can be utilized within the reduced-order stack model. A 1-D plug-flow model of the cathode region could be used in replace of the current CFD representation. As radiation is dominate within the stack, surface to surface radiation must be modeled with accurate view factors between the 1-D bands of the tubes and the surrounding walls. Also, tube groupings suggest the performance of a single cell should be aggregating only to cells within its tube grouping. This method requires simulation of N tube groupings where radiation view factors between tube groupings could be extracted from the high-fidelity model.

REFERENCES CITED

[1] Used with permission of Dr. R.J. Kee, Colorado School of Mines, 2010.

[2] Braun, R.J., Klein, S.A., Reindl, D.T., 2006. Evaluation of system configurations for solid oxide fuel cell-based micro-combined heat and power generators in residential applications, J. Power Sources, 158:1290-1305.

[3] Sorrentino, M., Pianese, C., Guezennec, Y. G. 2008. A hierarchical modeling approach to the simulation and control of planar solid oxide fuel cells. J. Power Sources 180:380-392.

[4] Aguiar, P., Adjiman, C.S., Brandon, N.P., 2004. Anode-supported intermediate temperature direct internal reforming solid oxide fuel cell. I: model-based steady-state performance. J. Power Sources 138:120-136.

[5] Lin, Y., Beale, S.B., 2006. Performance predictions in solid oxide fuel cells. Applied Mathematical Modeling 30:1485-1496.

[6] Chyou, Y.P., Chen J.S., Chung, T.D., 2008. A methodology for optimizing the start-up scenario of solid oxide fuel cell utilizing transient analyses. J. of ECS 155:B650-B659.

[7] Wang, L., Zhang, H., Weng, S., 2008. Modeling and simulation of solid oxide fuel cell based on the volume-resistance characteristic modeling technique, J. Power Sources 177:579-589.

[8] Calise, F., Dentice d'Accadia, M., Restuccia, G., 2007. Simulation of a tubular solid oxide fuel cell through finite volume analysis: Effects of the radiative heat transfer and exergy analysis, Int. J. Hydrogen Energy 32:4575-4590.

[9] Sanchez, D., Chacartegui, R., Munoz, A., Sanchez, T., 2006 Thermal and electrochemical model of internal reforming solid oxide fuel cells with tubular geometry, J. Power Sources 160:1074-1087.

[10] Aguiar, P., Adjiman, C.S., Brandon, N.P., 2005. Anode-supported intermediate temperature direct internal reforming solid oxide fuel cell. II: Model-based dynamic performance and control. J. Power Sources 147:136-147.

[11] Salogni, A., Colonna, P., 2010. Modeling of solid oxide fuel cells for dynamic simulations of integrated systems. Applied Thermal Engineering 30:464-477.

[12] Chyou, Y.P., Chung, T.D., Chen, J.S., Shie, R.F., 2005. Integrated thermal engineering analyses with heat transfer at periphery of planar solid oxide fuel cell. J. Power Sources 139:126-140.

[13] Beale, S.B., Zhubrin, S.V., 2005. A distributed resistance analogy for solid oxide fuel cells, Num. Heat Transfer, Part B, 47:573-591.

[14] Petruzzi, L., Cocchi, S., Fineschi, F., 2003. A global thermo-electrochemical model for SOFC systems design and engineering, J. Power Sources, 118:96-107.

[15] Kee, R.J., Kee, B.L., Martin, J.L., 2010: Radiative and convective heat transport within tubular solid-oxide fuel-cell stacks, J. Power Sources, 195:6688-6698.

[16] Cordiner, S., Mariani, A., Mulone, V., 2010. CFD-Based design of microtubular solid oxide fuel cells, J. of Heat Transfer, 132.

[17] Lockett, M., Simmons, M.J.H., Kendall, K., 2004. CFD to predict temperature profile for scale up of micro-tubular SOFC stacks, J. Power Sources, 131:243-246.

[18] Sorrentino, M., Pianese, C., 2009. Control oriented modeling of solid oxide fuel cell auxiliary power unit for transportation applications, J. Fuel Cell Science and Tech., 6.

[19] Murshed, AKM., Huang, B., Nandakumar, K., 2007. Control relevant modeling of planer solid oxide fuel cell system, J. Power Sources, 163:830-845.

[20] Akkaya, A., Sahin, B., Erdem, H., 2009. Thermodynamic model for exergetic performance of a tubular SOFC module, Renewable Energy, 34:1863-1870.

[21] Jiang, W., Fang, R., Khan, J.A., Dougal, R.A., 2006. Parameter setting and analysis of a dynamic tubular SOFC model, J. Power Sources, 162:316-326.

[22] Lee, K.H., Strand, R.K., 2009. SOFC cogeneration system for building applications, part 1: Development of SOFC system-level model and the parametric study, Renewable Energy, 34:2831-2838.

[23] Lisbona, P., Corradetti, A., Bove, R., Lunghi, P., 2007. Analysis of a solid oxide fuel cell system for combined heat and power applications under non-nominal conditions, Electrochimica Acta 53:1920-1930.

[24] Chan, S.H., Ding, O.L., 2005. Simulation of a solid oxide fuel cell power system fed by methane, Int. J. Hydrogen Energy 30:167-179.

[25] Lu, N., Li, Q., Sun, X., Khaleel, M.A., 2006. The modeling of a standalone solid-oxide fuel cell auxiliary power unit, J. Power Sources 161:938-948.

[26] Burke, A.A., Carreiro, L.G., 2006. System modeling of an air-independent solid oxide fuel cell system for unmanned undersea vehicles, J. Power Sources, 158:428-435.

[27] Braun, R.J., 2002. Optimal Design and Operation of Solid Oxide Fuel Cells for Small-scale Stationary Applications, Ph.D. Thesis, University of Wisconsin, Madison, WI.

[28] Ackermann, T., de Haart, L.G.J., Lehnert, W., Thom, F., 2000. Modeling of mass and heat transport in thick-substrate thin-electrolyte layer SOFCs, Proc. Of the 4th European SOFC Forum, July, Luzerne, Switzerland.

[29] Incropera, F., DeWitt, D., Bergman, T., Lavine, F., 2007. Fundamentals of Heat and Mass Transfer, 6th Ed. Wiley, New York.

[30] Microtherm International Ltd., 2001. Microtherm Insulation Product and Performance Data, product brochure, Table 3, p.5, June.

[31] Colclasure, A.M., Sanandaji, B.M., Vincent, T.L., Kee, R.J., 2011. Modeling and control of tubular solid-oxide fuel cell systems. I: Physical models and linear model reduction, J. Power Sources 196: 196-207.

[32] Poshusta, J., et al., Jul. 9 2009. Solid Oxide Fuel Cell Systems with Hot Zones and Two-Stage Tail Gas Combustors, Protonex Technology Corporation, US Patent Application 12/006,668.

[33] D.G., Goodwin, Cantera (Version 1.8) [Computer software], Pasadena, CA: Caltech. Available from: http://code.google.com/p/cantera

[34] Special Metals, Sept. 2008. INCONEL 600 Data Sheet, product data sheet, Table 3, p. 2.

[35] Jia, J., Abudula, A., Wei, L., Jiang, R., Shen, S., 2007. A mathematical model of a tubular solid oxide fuel cell with specified combustion zone, J. Power Sources 171:696-705.

[36] Karcz, M., 2009. From 0D to 1D modeling of tubular solid oxide fuel cell, Energy Conv. and Management., 50:2307-2315.

[37] G. van, Rossum, Python (Version 2.6) [Computer Software]. Available from: http://www.python.org

[38] Krummenacher, J., West, K., Schmidt, L., 2003. Catalytic partial oxidation of higher hydrocarbons at millisecond contact times: decane, hexadecane, and diesel fuel, J. Catalysis 215:332-343.

[39] Hohn, K., DuBois, T., 2008. Simulation of a fuel reforming system based on catalytic partial oxidation, J. Power Sources, 183:295-302.

APPENDIX

High-Fidelity Tubular System:

Input and Output File Descriptions

AirState.csv ---------- Written by UDF, stores profiles of oxidant composition adjacent to tube surfaces along with the tube temperature profile. Read in by tube model.

CPOX_Inlet.dat ---------- Written by UDF. Contains the state of fuel/air, recuperator exhaust, and heat flux at the interface between CFD model and CPOx model.

CPOX_Inputs.dat ---------- Input file for CPOx model. Contains input variables describing CPOx geometry and heat transfer coefficients. Geometry indirectly prescribed via two thermal resistances. Explicit geometry input and resistances calculated in: CPOX_HT_Problem_No_Radiation.EES.

CPOX_Outlet.dat ---------- Written by CPOx model. Contains the state of CPOx reformate leaving the fuel plenum.

emissivity.dat ---------- Input file used to store the emissivity of the tubes, Inconel, and insulation.

InputVariablesNew.dat ------ Input file setting tube model parameters. Both current/voltage demand and NewSetUp controlled by UDF.

qMEAinjO2.csv ---------- Written by tube model. Contains the flux of oxygen and heat at the tube surface.

ParameterInputs.dat---------- Input file for tube model. Contains tube geometry and physical properties.

Stack_Parameters.dat --------- Input file used to store information relating to the number of tubes in the bundle and the number of tubes per grouping.

surface_ids.txt ---------- Input file used to store the FLUENT surface IDs for each tube or tube group.

System_Inputs.dat ---------- Input file used for multiple models. Contains information on temperatures and flowrates entering the system as well as ambient conditions.

TGC_Inlet.dat ---------- Written by UDF. Contains the state of oxidant leaving the cathode and heat flux at the interface between CFD model and TGC model.

TGC_Inputs.dat ---------- Input file for TGC model. Contains input variables describing TGC geometry and heat transfer coefficients.

TGC_Outlet.dat ---------- Written by TGC model. Contains the state of preheated fuel/air and air streams as well as TGC exhaust entering the CFD domain.

Tube_Fuel_Outlets.dat ------- Written by UDF, contains the state of anode gases leaving each tube or tube grouping.

TubeInletOutletTemp.dat ---- Input file for tube model, written by UDF. Contains the inlet and outlet tip temperatures for a given tube or tube group.

Tube_Power.txt ---------- Written by UDF, contains the power of each tube or tube group in the system.

Tube_Tip_IDs.txt ---------- Input file used to store the Fluent surface IDs. Stores the faces where the solid non-electrochemical active tube is adjacent to the active tube length.

UDF_Inputs.txt ---------- Input file used to store UDF parameters. Contains information on the number of tube groups, relaxation factors, fitting coefficients, and the number of FLUENT iterations for every CPOx, TGC, and tube model call.